Cell Reports
Medicine

Article

Lymph node and tumor-associated PD-L1^{+} macrophages antagonize dendritic cell vaccines by suppressing CD8^{+} T cells

Graphical abstract

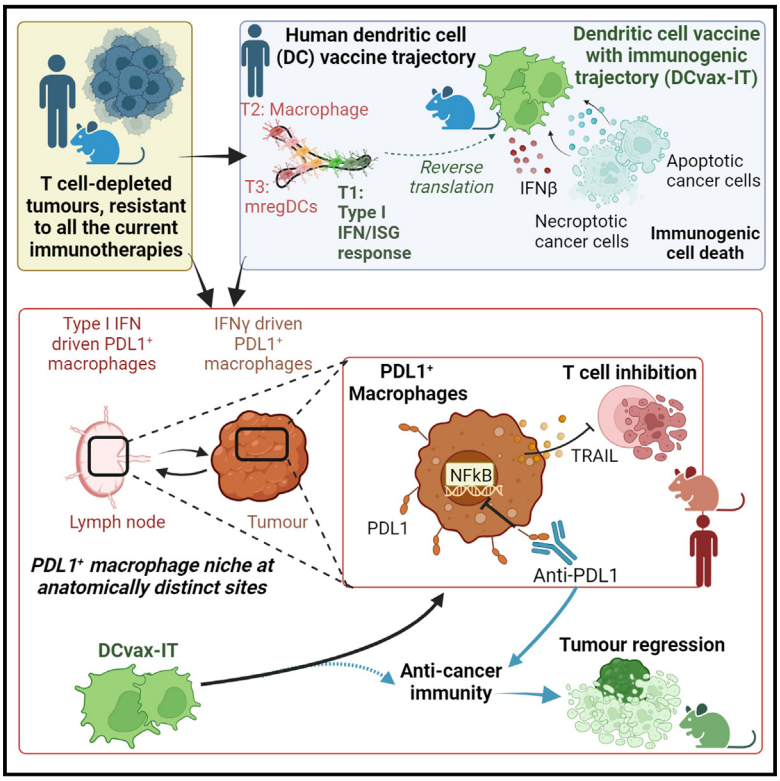

Highlights

- Multi-omics analyses predict a highly immunogenic type I IFN^{HIGH} DC vaccine state
- DC vaccines fail because they facilitate PD-L1^{+} TAMs in lymph nodes and tumors
- PD-L1^{+} TAMs suppress CD8^{+} T cell responses to disrupt DC vaccine efficacy
- Targeting PD-L1^{+} TAMs via PD-L1 blockade improves DC vaccine-driven tumor control

Authors

Jenny Sprooten, Isaure Vanmeerbeek, Angeliki Datsi, ..., Steven De Vleeschouwer, Rüdiger V. Sorg, Abhishek D. Garg

Correspondence

abhishek.garg@kuleuven.be

In brief

Sprooten et al. use human-to-mouse reverse translation to create DC vaccines. Counterintuitively, these induce an accumulation of CD8^{+} T cell-suppressive PD-L1^{+} macrophages in lymph nodes and tumors, such that vaccination and co-blockade of PD-L1 (but not PD-1) is mandatory for tumor suppression. This pathway is also operational in DC vaccinated cancer patients.

Sprooten et al., 2024, Cell Reports Medicine 5, 101377
January 16, 2024
https://doi.org/10.1016/j.xcrm.2023.101377

CellPress

Cell Reports Medicine

CellPress
OPEN ACCESS

Article

Lymph node and tumor-associated PD-L1$^+$ macrophages antagonize dendritic cell vaccines by suppressing CD8$^+$ T cells

Jenny Sprooten,[1] Isaure Vanmeerbeek,[1] Angeliki Datsi,[2] Jannes Govaerts,[1] Stefan Naulaerts,[1] Raquel S. Laureano,[1] Daniel M. Borràs,[1] Anna Calvet,[1] Vanshika Malviya,[3] Marc Kuballa,[2] Jörg Felsberg,[4] Michael C. Sabel,[4] Marion Rapp,[4] Christiane Knobbe-Thomsen,[4] Peng Liu,[5,6] Liwei Zhao,[5,6] Oliver Kepp,[5,6] Louis Boon,[7] Sabine Tejpar,[8] Jannie Borst,[9] Guido Kroemer,[5,6,10] Susan Schlenner,[3] Steven De Vleeschouwer,[11,12,13] Rüdiger V. Sorg,[2] and Abhishek D. Garg[1,14,*]

[1]Laboratory of Cell Stress & Immunity, Department of Cellular & Molecular Medicine, KU Leuven, Leuven, Belgium
[2]Institute for Transplantation Diagnostics and Cell Therapeutics, Medical Faculty, Heinrich Heine University Hospital, Düsseldorf, Germany
[3]Department of Microbiology, Immunology and Transplantation, KU Leuven-University of Leuven, Leuven, Belgium
[4]Department of Neurosurgery, Medical Faculty, Heinrich Heine University Hospital, Düsseldorf, Germany
[5]Metabolomics and Cell Biology Platforms, Gustave Roussy Cancer Center, Université Paris Saclay, Villejuif, France
[6]Centre de Recherche des Cordeliers, Equipe labellisée par la Ligue contre le cancer, Université de Paris, Sorbonne Université, Inserm U1138, Institut Universitaire de France, Paris, France
[7]JJP Biologics, Warsaw, Poland
[8]Laboratory for Molecular Digestive Oncology, Department of Oncology, KU Leuven, Leuven, Belgium
[9]Department of Immunology and Oncode Institute, Leiden University Medical Center, Leiden, the Netherlands
[10]Institut du Cancer Paris CARPEM, Department of Biology, Hôpital Européen Georges Pompidou, AP-HP, Paris, France
[11]Department of Neurosurgery, University Hospitals Leuven, Leuven, Belgium
[12]Laboratory of Experimental Neurosurgery and Neuroanatomy, Department of Neurosciences, KU Leuven, Leuven, Belgium
[13]Leuven Brain Institute (LBI), Leuven, Belgium
[14]Lead contact
*Correspondence: abhishek.garg@kuleuven.be
https://doi.org/10.1016/j.xcrm.2023.101377

SUMMARY

Current immunotherapies provide limited benefits against T cell-depleted tumors, calling for therapeutic innovation. Using multi-omics integration of cancer patient data, we predict a type I interferon (IFN) response^{HIGH} state of dendritic cell (DC) vaccines, with efficacious clinical impact. However, preclinical DC vaccines recapitulating this state by combining immunogenic cancer cell death with induction of type I IFN responses fail to regress mouse tumors lacking T cell infiltrates. Here, in lymph nodes (LNs), instead of activating CD4$^+$/CD8$^+$ T cells, DCs stimulate immunosuppressive programmed death-ligand 1-positive (PD-L1$^+$) LN-associated macrophages (LAMs). Moreover, DC vaccines also stimulate PD-L1$^+$ tumor-associated macrophages (TAMs). This creates two anatomically distinct niches of PD-L1$^+$ macrophages that suppress CD8$^+$ T cells. Accordingly, a combination of PD-L1 blockade with DC vaccines achieves significant tumor regression by depleting PD-L1$^+$ macrophages, suppressing myeloid inflammation, and de-inhibiting effector/stem-like memory T cells. Importantly, clinical DC vaccines also potentiate T cell-suppressive PD-L1$^+$ TAMs in glioblastoma patients. We propose that a multimodal immunotherapy and vaccination regimen is mandatory to overcome T cell-depleted tumors.

INTRODUCTION

Cancer immunotherapy with immune-checkpoint blockade (ICB) has improved the outlook for many patients.[1] However, not all cancers respond to current immunotherapies.[1] This is especially applicable to T cell-depleted tumors because they are non-immunogenic[2–5] and hence contain less CD8$^+$ T cells but abundant tumor-associated macrophages (TAMs) with anti-inflammatory (M2-like) activity.[6–9]

The immune control of poorly immunogenic tumors[4] can be potentiated by dendritic cell (DC) vaccines designed to elicit antigen-specific immunogenic responses.[4,8,10] Such vaccines typically utilize patient-derived autologous DCs that are pulsed with cancer antigens and stimulated with maturation stimuli *ex vivo* before they are reinjected into the patient.[11,12] DCs are endowed with the unique capacity to cross-present antigens to CD4$^+$/CD8$^+$ T cells in lymph nodes (LNs).[13,14]

Unfortunately, these pro-immunogenic capacities of DC vaccines have not consistently translated into the clinic.[11,15] Recently, the lack of efficacy of ICBs against T cell-depleted tumors has spurred the interest in multimodal immunotherapy regimens integrating next-generation DC vaccines.[4,12,15,16] Hence,

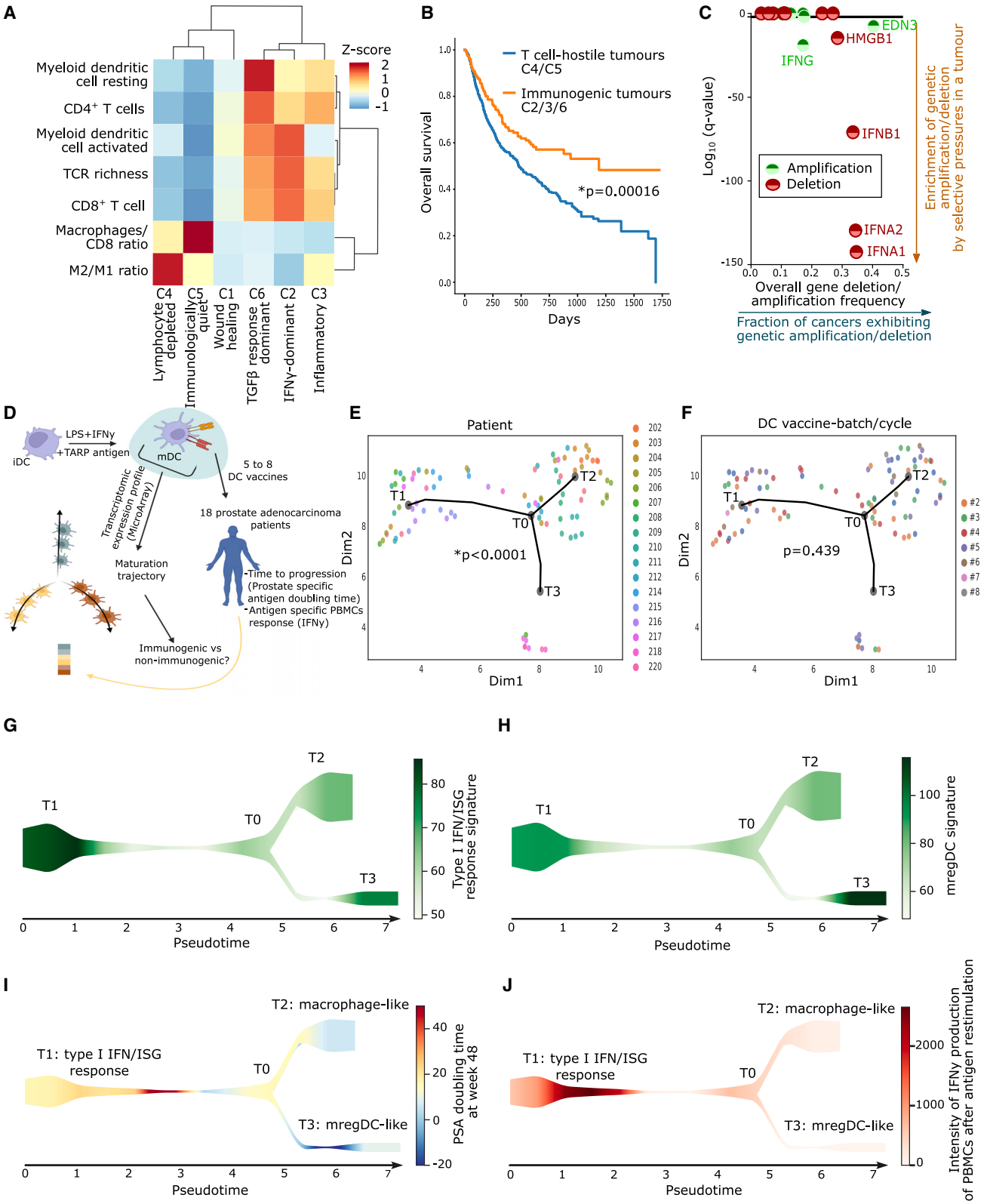

(legend on next page)

the overarching aim of this study was to use a human multi-omics cancer data-driven framework to inform the design of a next-generation DC vaccine with a highly immunogenic maturation trajectory (DCvax-IT) through a reverse translational approach. We wanted to tailor this DC vaccine against ICB non-responsive, T cell-depleted tumors and then decipher the exact immunological mechanisms regulating the anti-tumor effects of DCvax-IT. Finally, we aimed at confirming our preclinical observations in clinical settings as proof of concept for the future design of trials integrating DC vaccines.

RESULTS

Dysregulated danger signaling, defective type I interferon production, and DC depletion distinguishes the human T cell-depleted tumors

For a reverse translational approach, we first needed to extract the most dysregulated immune-pathways from human T cell-depleted tumors. Hence, we analyzed tumor immune landscapes in The Cancer Genome Atlas (TCGA).[17] Previously, an immunogenomics analysis had identified six pan-cancer immune-landscape classes (C1–C6; Figure 1A).[16] We reanalyzed these classes across 3,546 patients spanning 13 cancer types, for major immune cell fractions or ratios, and T cell receptor (TCR) richness (Figure 1A).[4,17] C4/C5 tumors showed the most striking depletion of $CD4^+$/$CD8^+$ T cells, TCR richness, and DCs (Figure 1A). Simultaneously, C4/C5 tumors exhibited high ratios of macrophages to $CD8^+$ T cells and M2 (anti-inflammatory) to M1 (pro-inflammatory) macrophages (Figure 1A).

Importantly, in an integrated multi-cancer dataset of 704 patients (spanning five cancer types) treated with ICBs,[18] overall survival of patients with C4/C5 tumors was significantly shorter compared to those bearing immunogenic C2/C3/C6 tumors (Figure 1B). This highlighted the suitability of TCGA C4/C5 tumors as transcriptomic representatives of ICB-resistant non-immunogenic tumors, which we will refer to as T cell-depleted tumors.

Next, we investigated transcriptomic anticorrelations between pairs of ligand-receptor, cell-receptor, or cell-ligand in TCGA C4/C5 tumors.[18,19] Such inverse correlations, representing immune dysregulation, were visually illustrated by node-to-node connecting arrows in a network (Figure S1A).[18,19] TCGA C4/C5 tumors exhibited an inverse correlation between various pairs relevant for danger signaling[20] (e.g., the TLR4 and type I interferon [IFN] pathways) (Figure S1A). Next, we pursued copy number variation (CNV) analyses for loci-centric amplification or deletion events of genes short-listed in the aforementioned network in pan-cancer TCGA data.[21] This revealed that type I IFN-related genes (*IFNA1/2*, *IFNB1*) were under the highest pan-cancer deletion pressures (Figure 1C). Altogether, these data indicated that human T cell-depleted tumors harbor various immune disparities and dysregulated danger signaling.

Type I IFN response distinguishes the most immunogenic and clinically efficacious maturation state of human DC vaccines

Previous clinical trials usually applied DC vaccines stimulated with IFNs (IFN$\alpha/\beta/\gamma$, inducing IFN-stimulated genetic [ISG] response) and/or TLR4-agonists (such as bacterial liposaccharide [LPS]), although with limited success.[22] We analyzed the DC vaccine transcriptomes from a clinical trial in which TLR4/IFN-stimulated DC vaccines were used against ICB-resistant (T cell-depleted) tumors. In this trial, 18 prostate cancer patients were treated with six to eight cycles of autologous monocyte-derived DC (moDC) vaccines pulsed with TCRγ alternate reading frame protein (TARP) antigen and stimulated with LPS + IFNγ (Figure 1D).[23] The bulk transcriptome of each DC vaccine could be correlated with patient responses (i.e., prostate-specific antigen [PSA] doubling time, as time-to-tumor progression [TTP]) and IFNγ production by TARP antigen-pulsed peripheral blood mononuclear cells (PBMCs). We performed a pseudo-time trajectory analysis[24] on transcriptomes of 93 DC vaccines (Figure 1D), revealing that these DC vaccines followed three rather distinct trajectories (T1, T2, or T3) (Figures 1E and 1F). These trajectories distinguished different patients (Figure 1E) but were independent from DC batches/cycles (Figure 1F). Next, we performed a REACTOME pathway enrichment per trajectory and found T1 enriched for type I IFN response and immunogenic/pro-inflammatory signaling (*IRF3*, *IFI44L*, *MAVS*, *CCR7*, *GBP4/5*, *MX2*, *RELB*, *OASL*, *HLA-DRA*, *CD40*, *TNFSF4*) (Figures S1B and S1C), T2 enriched for macrophage-like pathways (phagocytosis, scavenger receptor pathway, M2 macrophages; *CD68*, *CXCL1*, *CXCL12*, *CCL26*, *CEACAM3*, *CCL2*, *CCR1*) (Figures S1B and S1D), and T3 enriched for hyper-maturation and

Figure 1. T cell-depleted tumors and maturation trajectories of human DC vaccines

(A) CIBERSORT deconvolution across TCGA cancer types. Population abundances were row normalized (C1, n = 1,313; C2, n = 1,210, C3, n = 688; C4, n = 222, C5, n = 2; C6, n = 111).

(B) Overall survival of cancer patients' transcriptome profiled before ICBs treatment (anti-PD-1/CTLA4/PD-L1 ICBs, or combinations thereof) sub-grouped in T cell-depleted C4/C5 tumors (n = 667) and immunogenic C2/C3/C6 tumors (n = 474). Statistics: log rank test.

(C) GISTIC 2.0 analysis with indicated 12 genes. Statistical significance: false discovery rate (FDR) < 0.05 (random permutations to background score distribution, BH adjusted). Bladder cancer, n = 136; breast cancer, n = 880; colorectal adenocarcinomas, n = 585; glioblastoma multiforme, n = 580; head and neck cancer, n = 310; kidney cancer, n = 497; acute myeloid leukemia, n = 200; lung adenocarcinoma, n = 357; lung squamous cell carcinoma, n = 344; ovarian cancer, n = 563; endometrial cancer, n = 496.

(D–J) Single-cell trajectory reconstruction exploration and mapping (STREAM) DC vaccine trajectory of 93 DC vaccines from 18 prostate adenocarcinoma patients vaccinated with five to eight vaccines. (D) Overview of STREAM DC vaccine trajectory. (E and F) Pseudo-time inferred from DC vaccines' transcriptome based on variable genes. Principal graph initiated with epg_alpha = 0.01, epg_mu = 0.2, epg_lambda = 0.03, and epg_n_nodes = 5. Dots depict individual DC vaccines and dot color represents (E) patient number or (F) DC vaccine batch/cycle (chi-squared test of independence of variables). (G and H) Signature scores overlaid on the graph as streamplots. Type I IFN/ISG-response signature (G) or mature regulatory DC signature (H) were used as color intensity. (I and J) Patient outcomes were overlaid on the graph as streamplots. PSA doubling time at week 48 (I) and intensity of IFNγ production of peripheral blood mononuclear cell after antigen restimulation (J) were used as color intensity. Here, "n" represents different patients (biological replicates). See also Figure S1.

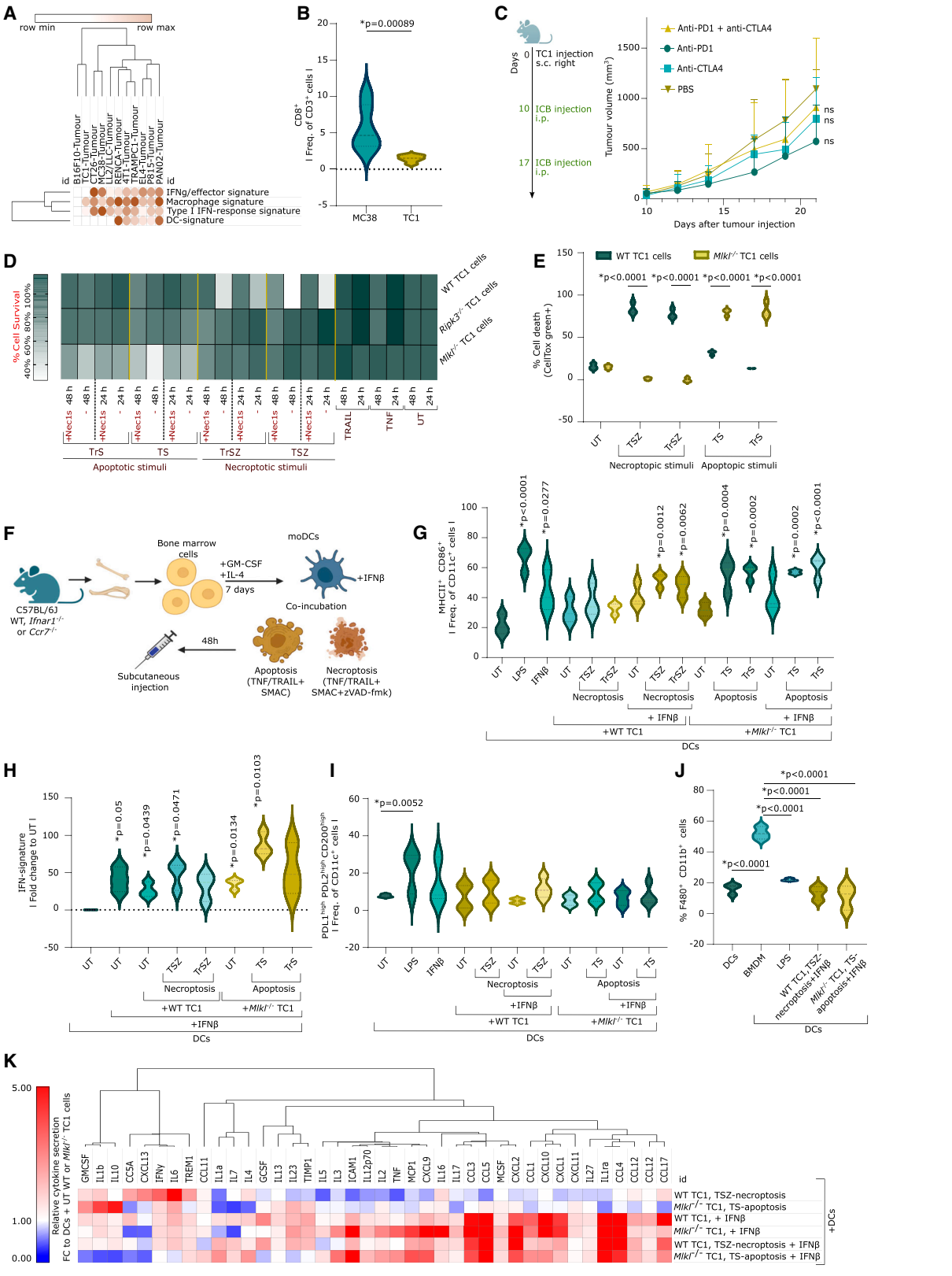

(legend on next page)

immune-checkpoint signaling (*CLEC10A*, *TLR5*, *TGFA*, *SIGLEC6/9/12*, *CD36*, *IL12R*, *IL13RA1*, *ENTPD1*, *IL1R1*, *CMTM6*, *TNFRSF10B*, *REL*, *S1PR1*) (Figures S1B and S1E).

T1 might correspond to a specific ISG-response$^+$ DC vaccine subset, T2 a macrophage-like phenotype,[14] and T3 a maturation-associated regulatory (mreg)-DC program.[14,25] To validate this interpretation, we applied published ISG-response signature (Table S1) and an mregDC-signature (Table S1) to these trajectories.[25,26] Indeed, the ISG-response signature was preponderant in T1 (Figure 1G), while the mregDC-signature was most abundant in T3 (Figure 1H).

Next, we aligned these trajectories with tumoral (TTP or PSA doubling time) (Figure 1I) and antigen-specific (PBMC) patient responses (Figure 1J). We found that the T1 trajectory correlated with strong antigen-specific responses and longer TTP, contrasting with T2 and T3 trajectories, which associated to weak antigen-specific responses and a shorter TTP (Figures 1I and 1J). These data suggested that a potential DCvax-IT approach should favor a type I IFN/ISG-response^{HIGH} state over macrophage-like or mregDC-like states.

Murine TC1 tumors phenocopy immune disparities of human T cell-depleted tumors

To formulate a preclinical DCvax-IT, it appeared necessary to delineate a syngeneic murine tumor model mimicking the major immune-disparities of human T cell-depleted tumors. Therefore, we conducted an analysis of tumor transcriptomes from 11 commonly used (subcutaneous) murine tumor models in immuno-oncology[27] (Figure 2A). This involved genetic signatures (Table S1) for pro-lymphocytic IFNγ/effector signaling, macrophages, type I IFN/ISG response, or DCs.[27,28] This revealed that the triple-oncogene-driven c-H-Ras$^+$HPV16-E6$^+$HPV16-E7$^+$TC1 tumors[29] recapitulated most features of human T cell-depleted tumors (negligible IFNγ/effector signaling, type I IFN/ISG response, and DCs vs. enrichment of the macrophage signature) (Figure 2A).

Next, we pursued tumor immunophenotyping to validate the choice of TC1 tumors and selected the immunogenic MC38 tumors[30] for comparison (Figure 2A). Compared to MC38 tumors, TC1 tumors had significantly lower CD8$^+$CD3$^+$ T cell infiltrates (Figure 2B), lower CD8$^+$ T cell-to-TAMs (CD11b$^+$F4/80$^+$) ratio (Figure S2A), and a higher CD8$^+$ T cell death (Figure S2B). This was further supported by TC1 tumors being non-responsive to PD-1/cytotoxic T lymphocyte-associated protein (CTLA)-4 blockade, or a combination thereof (Figure 2C). Finally, in line with defective type I IFN/TLR danger signaling in human C4/C5 tumors, TC1 cancer cells failed to secrete IFNα/β upon stimulation with agonists of TLR4 (LPS), TLR7 (imiquimod), RIG-I (5′pppdsRNA), STING/cGAS (2′3′cGAMP), and immunogenic (doxorubicin) or non-immunogenic (cisplatin) chemotherapy (Figures S2C and S2D). This underscored the suitability of TC1 tumors as preclinical representatives of human T cell-depleted C4/C5 tumors.

TC1-cells undergo apoptotic or necroptotic immunogenic cell death with antigen release

We explored the possibility of providing damage-associated molecular pattern (DAMP)-based danger signaling and antigen-release-based DC pulsing via immunogenic cell death (ICD).[10,15] ICD is well established to potentiate anticancer DC vaccines.[31] However, it is currently debatable which underlying cell death pathway (i.e., apoptotic vs. necroptotic) has the strongest potentiating effect.[32]

To distinguish apoptosis vs. necroptosis, we utilized death receptor-driven necroptotic (combination of tumor necrosis factor [TNF]/TRAIL, BV6, and zVAD-fmk) vs. apoptotic stimuli (combination of TNF/TRAIL and BV6).[33,34] TNF or TRAIL were comparatively used to account for their distinct pro-inflammatory activity.[35] The death of wild-type (WT) TC1 cells in response to necroptotic stimuli was avoided by RIPK1 inhibitor, Nec1s.[36] WT TC1 cells did not respond to apoptotic stimuli (Figure 2D). To overcome this, we used CRISPR-Cas9-driven knockout of two necroptosis regulators (i.e., *Ripk3* or *Mlkl*) (Figures S2E and S2F).[34] *Ripk3*$^{-/-}$TC1 cells were resistant to both necroptotic and apoptotic stimuli (Figure 2D). Instead, *Mlkl*$^{-/-}$ TC1 cells showed resistance to necroptotic but susceptibility to apoptotic stimuli (Figure 2D). WT TC1 cells underwent necroptotic cell death (Figure 2E) based on the following findings: the absence of caspase-3/7 activity (Figure S2G), non-sustained annexin V staining (Figures S2H and S2I), and phosphorylation of MLKL

Figure 2. Optimization of DCvax-IT for T cell-depleted tumors

(A) Metagene expression for indicated signatures in different subcutaneous tumors (from GEO: GSE85509).

(B) Flow cytometry analysis of CD45$^+$ fraction from subcutaneous MC38/TC1 tumors on day 23 after injection (percentage of CD8$^+$ of CD3$^+$ cells, n = 6; two-tailed Student's t test).

(C) Tumor volume of TC1-tumor-bearing mice treated with anti-PD-1/CTLA4 on day 9/16 after injection (n = 6; area under curve; one-way ANOVA, Kruskal-Wallis test).

(D) Survival of WT, *Ripk3*$^{-/-}$, and *Mlkl*$^{-/-}$ TC1 cells 24/48 h after treatment (three or four repeats).

(E) Cell death of WT and *Mlkl*$^{-/-}$ TC1 cells 48 h after treatment. p values depict comparison WT vs. *Mlkl*$^{-/-}$ TC1 cells (n = 3; two-way ANOVA, Sidak's multiple comparisons test).

(F) Schematic overview of the vaccine formulation process.

(G and H) Functional analysis of DCs untreated or stimulated with LPS, IFNβ, or with untreated or dying TC1s (with/without IFNβ). (G) Flow cytometry of DC maturation (MHCII$^+$ CD86$^+$ frequency of CD11c$^+$). p values depict comparison vs. UT DCs (n = 3; one-way ANOVA, Dunnett's multiple comparisons test). (H) IFN-signature expression (qPCR). p values depict comparison vs. UT DCs (n = 3; one sample t test).

(I) Flow cytometry of frequency of PD-L1$^+$PD-L2$^+$CD200$^+$ of CD11c$^+$ cells (moDCs alone/cocultured with untreated/dying WT/*Mlkl*$^{-/-}$ TC1 cells). p values depict comparison vs. UT moDCs (n = 4, LPS/IFNβ n = 3; one-way ANOVA, Fischer least significant difference [LSD]).

(J) Flow cytometry of frequency of CD11b$^+$F4/80$^+$ in moDCs (alone/cocultured with untreated/dying WT/*Mlkl*$^{-/-}$ TC1 cells) or bone-marrow-derived macrophages (BMDMs). p values depict comparison vs. BMDMs (n = 3; one-way ANOVA, Dunnett's multiple comparisons test).

(K) Cytokine secretion via cytokine array. From all values, the background was subtracted. Normalization was done using moDCs + untreated cancer cells (n = 3).

Here, "n" represents biological replicates and error bars represent SEM. See also Figures S2 and S3.

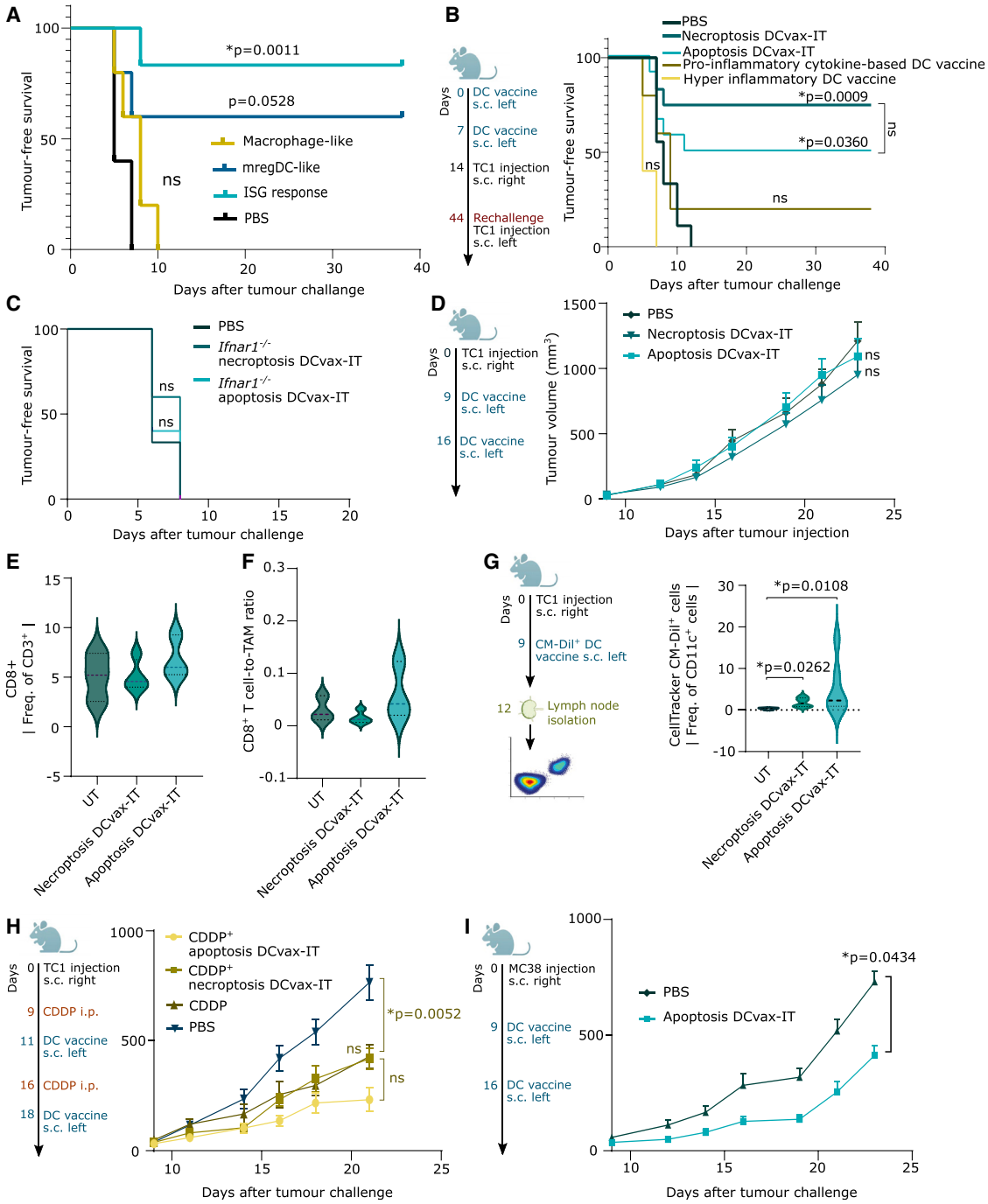

Figure 3. DCvax-IT fails against T cell-depleted tumors in a curative setup

(A–C) Tumor-free survival of mice vaccinated with two prophylactic DC vaccines (day 0/7), followed by subcutaneous TC1 challenge. p values depict comparison vs. PBS-treated mice. (A) Comparison of indicated DC vaccines to PBS-treated mice (PBS, n = 5; all vaccines; n = 5, log rank, Mantel-Cox test). (B) Comparison of indicated DC vaccines to PBS-treated mice (PBS, n = 9; necroptotic/apoptotic DCvax-IT, n = 6; pro-inflammatory cytokine/hyper-inflammatory DC vaccines, n = 5, log rank [Mantel-Cox] test). (C) Comparison of indicated DC vaccines to PBS-treated mice (PBS, n = 6; apoptosis/necroptosis DCvax-IT, n = 5, log rank [Mantel-Cox] test).

(D) TC1-tumor-bearing mice treated with DCvax-IT (day 9/16 after injection). Comparison to PBS-treated mice (n = 12, area under curve; Kruskal-Wallis test). (E and F) Flow cytometry analysis of $CD45^+$ fraction from untreated/DCvax-IT-treated TC1 tumors (day 23 after tumor injection). Frequency of (E) $CD8^+$ T cells or (F) $CD8^+$ T cells to TAM ratio. Comparison to PBS-treated mice (UT, n = 3; necroptosis DCvax-IT, n = 4; apoptosis DCvax-IT, n = 3, one-way ANOVA, Dunnett's multiple comparisons test).

(legend continued on next page)

(Figures S2L and S2M) (hereafter referred to as necroptotic^{TC1}). Conversely, *Mlkl*$^{-/-}$ TC1 cells underwent apoptotic cell death (Figure 2E) as indicated by significant caspase-3/7 activity (Figure S2G), sustained annexin V staining (Figures S2J and S2K), and the absence of MLKL phosphorylation (Figures S2L and S2M) (hereafter referred to as apoptotic^{TC1}). We did not explicitly use *Casp8*$^{-/-}$ TC1 cells as necroptotic system because *Casp8*$^{-/-}$ or *Casp8*$^{-/-}$*Casp9*$^{-/-}$ (but not *Casp9*$^{-/-}$) TC1 cells (Figure S2N) underwent Nec1s-inhibitable cell death upon apoptotic stimuli (Figure S2O), thereby making the latter redundant.

Finally, we analyzed the ICD-like DAMP-profiles.[32] Both apoptotic^{TC1} and necroptotic^{TC1} showed surface-calreticulin^{HIGH} CD47^{LOW} cells (Figure S2P), as well as the release of ATP (Figures S2Q and S2R), HMGB1 (Figure S2S), and the TC1-specific E7 antigen (Figure S2S). Thus, TC1 cells showed proficient DAMP-based apoptotic/necroptotic ICD coupled with antigen release.

DCvax-IT co-integrating ICD and IFNβ stimulation favor type I IFN responses over macrophage-like or mregDC-like phenotypes

We based our DC vaccines on bone-marrow-derived moDCs (Figure 2F). We compared different types of IFN (IFNα/β/γ)[37] for their potential to induce DC maturation (MHC-II$^+$CD86$^+$CD11c$^+$) (for flow cytometry gating strategy, see Dataset S1) and secretion of the ISG-factor CXCL10. LPS served as a positive control. IFNβ induced the most pronounced DC maturation (Figure S2T) and CXCL10 secretion (Figure S2U). We selected 2.5 ng/mL IFNβ for the rest of the study since it achieved sufficient maturation, CXCL10 release and upregulated several ISGs in DCs: *Irf7*, *Rsad*, *Mx1*, *Cxcl9*, or *Cxcl10* (Figure S2V).

We pulsed moDCs with apoptotic/necroptotic^{TC1}, with or without IFNβ-stimulation (Figure 2F), and checked for successful pulsing (efferocytosis of apoptotic/necroptotic^{TC1} by DCs), DC maturation, bulk IFN/ISG-response genetic signature, macrophage-like/mregDC-like phenotype, and increase in CCR7$^+$DCs (necessary for LN homing). After pulsing with apoptotic^{TC1}, we already saw promising DC stimulation (i.e., efferocytosis of TC1 cells) (Figure S3A) and DC maturation (Figure 2G), which was further enhanced by IFNβ (Figures 2G and S3B). Costimulation with IFNβ was useful for necroptotic^{TC1} since it outperformed DC maturation by necroptotic^{TC1} alone (Figures 2G, S3C, and S3D). Also, the combination of ICD and IFNβ increased CCR7$^+$ DCs (Figures S3E and S3F).

Next, to confirm type I IFN/ISG response, we investigated the induction of the ISG-signature (metagene for *Irf7*, *Rsad*, *Mx1*, *Cxcl9*, and *Cxcl10*) in cocultures of DC + TC1 + IFNβ. The IFNβ-induced ISG response was either maintained or potentiated in the cocultures (Figure 2H). Moreover, TNF-elicited apoptosis/necroptosis was better at preserving or potentiating ISG response than TRAIL-induced cell death (Figure 2H). Altogether, these data drove us to prioritize cocultures of DCs, TNF-driven apoptosis/necroptosis, and IFNβ for the DCvax-IT formulation. We checked for the presence of macrophages-like (CD11b$^+$F4/80$^+$) and mregDCs-like (programmed death-ligand 1 [PD-L1]$^+$PD-L2$^+$CD200$^+$CD11c^{+25}) phenotypes (for flow cytometry gating strategy, see Dataset S1) in DCvax-IT. LPS stimulation alone favored the acquisition of mregDC-like phenotype (Figure 2I). However, the presence of dead cancer cells avoided the mregDC-like phenotype (Figure 2I). Moreover, compared to bone-marrow-derived macrophages, apoptotic^{TC1}/necroptotic^{TC1} DCvax-IT contained few CD11b$^+$F4/80$^+$ macrophages (Figure 2J).

Finally, we explored the DCvax-IT secretome using an antibody array combined with gene-set enrichment analysis (GSEA)-based Gene Ontology biological pathway analyses. The secretome of necroptotic^{TC1} + DCs was more inflammatory than that of apoptotic^{TC1} + DCs (Figures 2K, S3G, and S3H). Costimulation with IFNβ strongly induced an array of pro-inflammatory cytokines (Figures 2K, S3I, and S3K) with the notable exception of IFNγ (Figure 2K). Thus, our preclinical DCvax-IT resembled the human DC vaccines with an immunogenic trajectory.

Type I IFN response distinguishes the most immunogenic DC vaccine *in vivo*

Next, we wondered whether the trajectories of DC vaccines can be validated *in vivo*. Three distinct mouse DC preparations were conceived to recapitulate human DC vaccine trajectories, i.e., the ISG-response$^+$ DC vaccine (DCs stimulated with IFNβ), mregDC-like vaccine (DCs stimulated with LPS), and a macrophage-like vaccine (monocytes differentiated with M-CSF + IL4). These preparations were pulsed with antigenic peptides from TC1 cells (E6/E7 peptides) and prophylactically injected into mice to elicit an immune response that protects against later rechallenge with TC1 cells. PBS injection was used as a negative control. The ISG-response$^+$ DC vaccine significantly protected from tumor challenge (compared to PBS treatment) (Figure 3A). By comparison, mregDC-like vaccine protected fewer mice from tumor challenge and macrophage-like vaccine completely failed to confer immune protection (Figure 3A). Thus, DC vaccines favoring a type I IFN/ISG-response^{HIGH} state have the highest immunogenic potential.

DCvax-IT induces type I IFN sensing-dependent anticancer immunity *in vivo*

Next, we assessed the immunogenicity of DCvax-IT in the prophylactic setting (Figure 3B). Two injections with both apoptotic^{TC1}/necroptotic^{TC1} DCvax-IT efficiently protected mice from tumor challenge within 1 week (Figure 3B) and tumor-free mice also resisted a second rechallenge with TC1 cancer cells (Figure S3L). This *in vivo* immunogenicity of DCvax-IT was superior

(G) Frequency of Celltracker CM-DiI$^+$CD11c$^+$ cells in LNs of vaccinated mice. p values depict comparison vs. PBS-treated mice (UT, n = 4, necroptosis/apoptosis DCvax-IT, n = 6, one-way ANOVA, Kruskal-Wallis test).
(H) TC1-tumor-bearing mice treated with cisplatin (day 9/16) alone or in combination with DCvax-IT (day 11/18) and after TC1-injection. p values depict comparison vs. cisplatin-treated mice (n = 8; area under curve, one-way ANOVA, Dunnett's multiple comparisons test).
(I) MC38-tumor-bearing mice treated with DCvax-IT (day 9/16) after MC38-injection. p values vs. PBS-treated mice (PBS, n = 8; apoptosis DCvax-IT, n = 10, area under curve, Mann-Whitney test). Here, "n" represents biological replicates and error bars represent SEM. See also Figure S3.

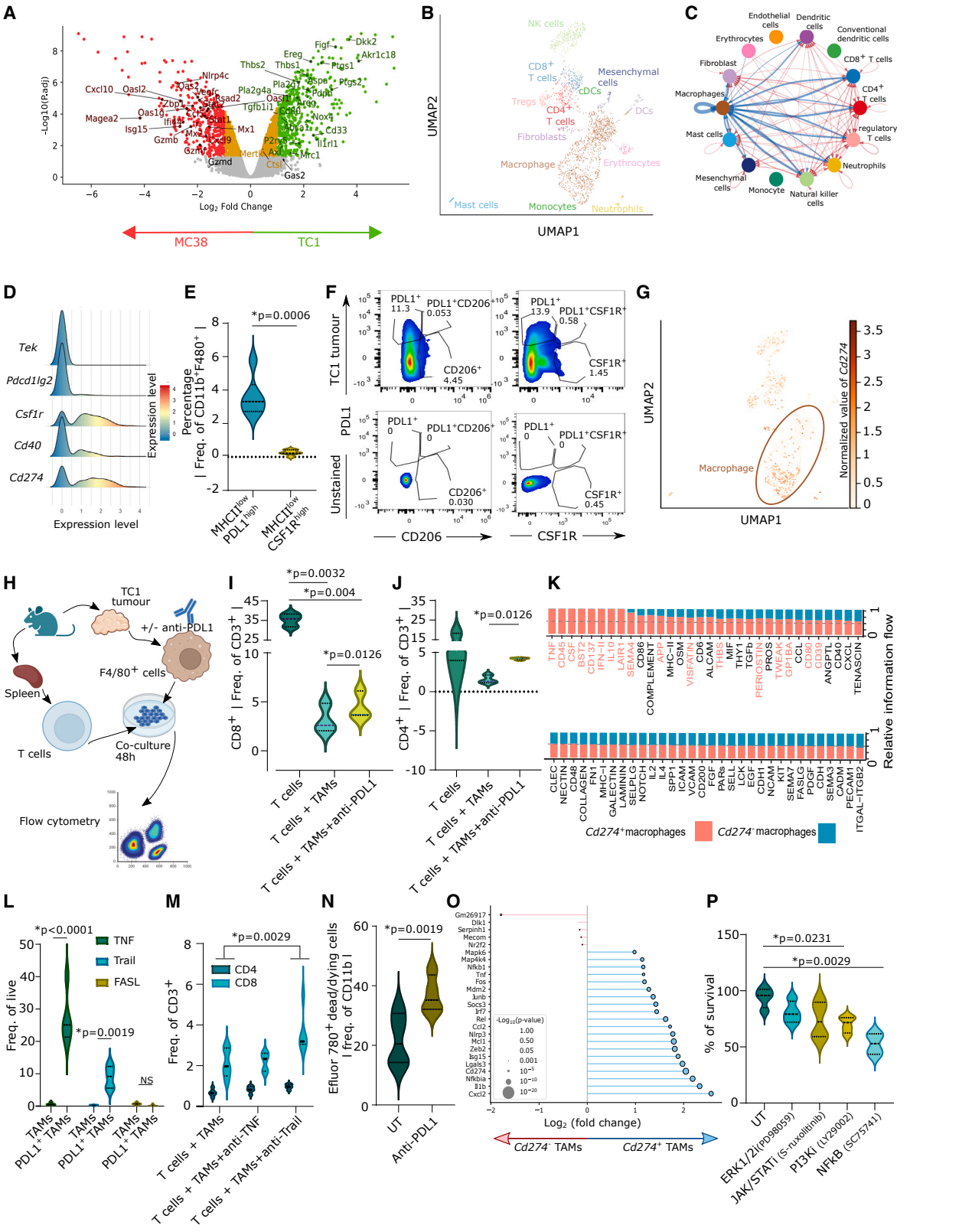

(legend on next page)

to some other frequently used maturation formulations of DC vaccines (Figure 3B), namely, pro-inflammatory cytokine-based DC vaccines (DCs co-stimulated with IL1β, IL6, PGE2, and TNF)[38–41] or hyperinflammatory DC vaccines (DCs co-stimulated with LPS and IFNγ).[42–46]

Next, we wondered if type I IFN sensing via receptor complex of IFNAR1::IFNAR2 on DCs was necessary for the induction of anticancer immunity. Hence, we re-tested apoptotic^{TC1}/necroptotic^{TC1} DCvax-IT with *Ifnar1*$^{-/-}$ DCs. Efferocytosis of apoptotic^{TC1}/necroptotic^{TC1} by *Ifnar1*$^{-/-}$ DCs was efficient (Figures S3M and S3N) but *Ifnar1*$^{-/-}$ DC maturation was not proficient (Figure S3O). Accordingly, mice vaccinated with *Ifnar1*$^{-/-}$ DCs-based DCvax-IT failed to resist tumor challenge (Figure 3C). In conclusion, DCvax-IT efficiently induced anticancer immunity in a fashion that relied on the ability of the DC to sense IFNβ.

Curative DCvax-IT fails against T cell-depleted tumors but acts against T cell-infiltrated tumors

We evaluated DCvax-IT in a therapeutic setting, in mice bearing TC1 tumors (Figure 3D). However DCvax-IT failed to slow down the growth of TC1 tumors (Figure 3D), to increase CD8$^+$ T cell infiltration (Figure 3E), or to shift the CD8$^+$ T cell-to-TAM ratio (Figure 3F).

We wondered whether DCvax-IT failed to reach the tumor-draining LN, because moDCs exhibit limited LN-homing,[10] particularly with preexisting tumors.[47,48] Hence, we fluorescently labeled the DCvax-IT with CellTracker CM-DiI and injected them into mice to evaluate their accumulation in inguinal/axillary LNs draining the subcutaneous injection site (Figure 3G). There was significant LN-enrichment of CM-DiI$^+$ DCvax-IT (Figure 3G), which was similar in tumor-free and TC1-tumor-bearing mice (Figure S3P). Moreover, the LN-enriched CM-DiI$^+$ DCvax-IT retained their IFN response *in vivo*, as suggested by high phosphorylated-signal transducer and activator of transcription 1 (STAT1),[49] which exceeded that found in CM-DiI^{NEGATIVE} DCs (Figure S3Q).

Next, we investigated if TC1 tumors can be overcome by combinatorial chemotherapy. However combining DCvax-IT with cisplatin, a chemotherapy with immunotherapy-synergizing properties in TC1 tumors,[7,50] did not add therapeutic efficacy (Figure 3H).

We investigated the possibility that the non-immunogenicity of TC1 tumors could explain their resistance to DCvax-IT. Hence, we therapeutically applied DCvax-IT against the T cell-enriched MC38 tumors, which are responsive to ICBs (Figure S3R). We focused on apoptotic^{MC38} DCvax-IT because MC38 cells were only susceptible to apoptosis (Figures S3S and S3T).[51] Here, we observed that DCs efficiently executed efferocytosis (Figures S3U and S3V) and phenotypically matured (Figure S3W) when exposed to apoptotic^{MC38} plus IFNβ. Interestingly, apoptotic^{MC38} DCvax-IT significantly reduced MC38-tumor growth (Figure 3I). Thus, despite the high immunogenicity and proficient LN-homing abilities of DCvax-IT, T cell-depleted (but not T cell-infiltrated) tumors were resistant to DCvax-IT.

TC1 tumors preferentially accumulate anti-inflammatory PD-L1$^+$ TAMs

To improve the efficacy of DCvax-IT, it appeared critical to identify the dominant immunoresistance pathway operating in TC1 tumors. Differential gene expression (DGE) analyses comparing the bulk transcriptomes of TC1 and MC38 tumors (Figure 2A) indicated that TC1 tumors preferentially expressed genes embedded in anti-inflammatory pathways relevant to myeloid cells and TAMs (Figure 4A; Table S2).[52] To confirm this at single-cell resolution, we accessed published single-cell RNA sequencing (scRNA-seq) data of TC1 tumors[53] (Figure 4B). Here, we pursued a cell-to-cell interaction with CellChat.[54] TAMs established the densest interactions with all other tumoral immune/stromal cells, as indicated by the broadest width of connecting nodes (Figure 4C). Immunophenotyping confirmed that, as compared to MC38 tumors, TC1 tumors contained a higher M2-to-M1 TAM ratio (Figure S4A) and low M1-like MHC-II^{HIGH}CD206^{LOW} TAMs (Figure S4B). Also, TC1 tumors contained more TAMs than DCs (Figure S4C).

Figure 4. TC1 tumors enrich CD8$^+$ T cell-suppressive PD-L1$^+$ macrophages

(A) Volcano plot of gene expression between MC38 and TC1 tumors (GEO: GSE85509).

(B) Uniform manifold approximation and projection (UMAP) of untreated TC-1 tumor scRNA-seq data (GSM7103827).

(C) Inferred cell-cell communication by CellChat from dataset in (B) (bandwidth indicates intensity of cell-to-cell communication).

(D) Macrophages as density over expression of indicate gene levels from dataset in (B).

(E) CD45$^+$ cell fraction from TC1 tumors (day 23 after injection). Frequency of TAMs (n = 6; two-tailed paired t test).

(F) Flow cytometry analysis of PD-L1$^+$, CSF1R$^+$, CD206$^+$ (gating on unstained samples) on TAM from TC1 tumors isolated on day 23 post injection.

(G) UMAP of TC1-tumor scRNA-seq data indicating normalized *Cd274* expression (log1p-transformed reads per 10,000).

(H–J) Flow cytometry of T cell recovery after cocultures with TAMs from TC1 tumors (day 23 post injection), pre-incubated with/without anti-PD-L1 for 48 h, together with paired spleen-derived T cells. (H) TAM/T cell coculture experimental setup. (I and J) Frequency of (I) CD8$^+$ T cells and (J) CD4$^+$ T cells (n = 3; two-tailed paired t test).

(K) Relative information flow (CellChat) of Cd274$^+$ and Cd274$^-$ macrophages (1,006 cells) from dataset in (B).

(L) TNF, TRAIL, FASLG expression of indicated TAMs from TC1 tumors (isolated on day 23 post injection) (n = 5; two-way ANOVA; Sidak's multiple comparisons test).

(M) Flow cytometry analysis of live T cell recovery, as per experimental setup in (H) and (J) but pre-incubated with/without anti-TNF/anti-TRAIL for 48 h, together with paired spleen-derived T cells (n = 5; two-way ANOVA).

(N) Flow cytometry analysis of Efluor 780$^+$ dead/dying cell in untreated/anti-PD-L1-treated TC1-derived TAMs (isolated on day 23 post injection) (n = 4; two-tailed paired t test).

(O) DGE of *Cd274*$^+$ macrophages (blue) vs. *Cd274*$^-$ macrophages (red) from dataset in (B). The x axis: log2 fold change of PD-L1$^+$ to PD-L1$^-$. Size of circles: −log10-transformed p values.

(P) Percentage TAM survival from TC1 tumors (day 23 post injection) treated with different inhibitors (n = 4; one-way ANOVA; Dunnett's multiple comparisons test). Here, "n" represents biological replicates. See also Figure S4.

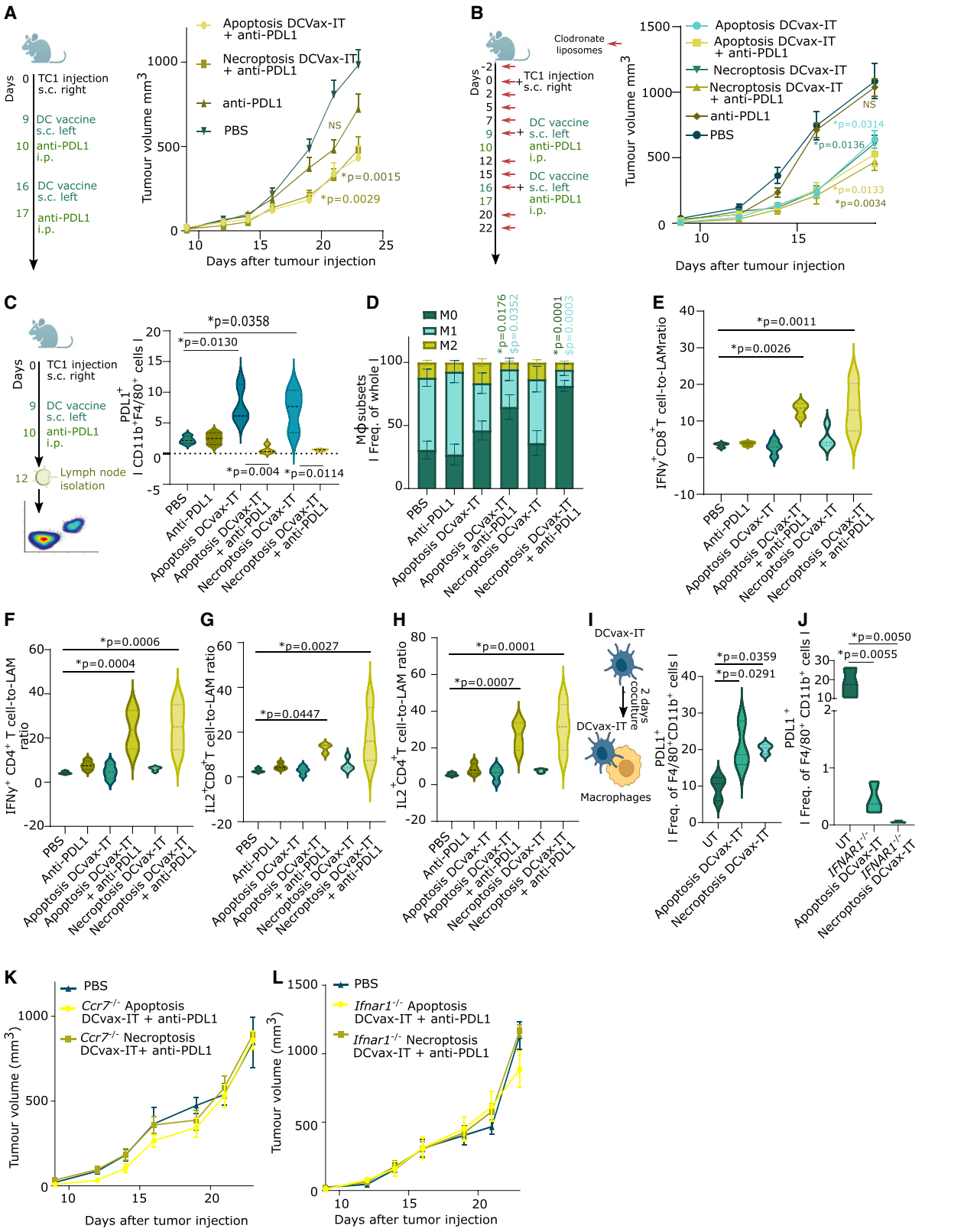

(legend on next page)

Several TAM-associated targets are currently explored as potential therapeutic targets; e.g., CSF1R, CCR2, CX3CR1, SIRPA, TIE2 (*Tek*), PD-L1 (*Cd274*), PD-L2 (*Pdcd1lg2*), CD40, IDO1, and PD-1 (*Pdcd1*).[6,8,52] To prioritize among these, we used the differential TC1-specific myeloid genes (Figure 4A) as input for a correlation GSEA against a reference murine macrophage transcriptome.[55] This predicted *Csf1r*, *Cd274*, *Cd40*, *Tek*, and *Pdcd1lg2* as the top five targets (Figure S4D). On the scRNA-seq level, TC1-tumor-infiltrating TAMs most highly expressed *Csf1r*, followed by *Cd274* (Figure 4D). Tumor immunophenotyping emphasized that TC1 tumors were dominated by immunoregulatory (MHC-II^{LOW}) TAMs expressing significant PD-L1 (PD-LI^{+}MHC-II^{LOW}) rather than CSF1R (CSF1R^{+}MHC-II^{LOW}) (Figure 4E). In TC1 tumors, PD-LI^{+}MHC-II^{LOW} TAMs were strongly enriched and were distinct from CSF1R^{+}MHC-II^{LOW} TAMs or the standard M2-like CD206^{+}MHC-II^{LOW} TAMs (Figure 4F). Such distinct PD-L1^{+} TAMs were also observed in LLC tumors (another T cell-depleted tumor) (Figure S4E). Of note, most of the *Cd274* originate from TAMs (Figure 4G) and accordingly there were more PD-L1^{+} TAMs than PD-L1^{+} DCs/cDC1/cDC2 (Figure S4F). Moreover, *Cd274*$^{+}$ TAMs exhibited stronger interactions than *Cd274*$^{-}$ TAMs, reflecting higher activity (Figure S4G). Thus, TC1 tumors enrich M2-like PD-L1^{+} TAMs.

PD-L1^{+} TAMs limit CD8^{+} T cell responses via TRAIL signaling

PD-L1^{+} TAMs can limit T cell responses through a thus-far elusive mechanism.[56] We isolated TAMs from TC1 tumors and splenic lymphocytes from the same mice and cocultured them with or without PD-L1 blockade (Figure 4H). The presence of TAMs reduced the recovery of live CD8^{+}/CD4^{+} T cells, and PD-L1 blockade partially but significantly improved the recovery of live T lymphocytes (Figues 4I and 4J). This phenotype was PD-L1 specific, rather than dependent on PD-L1 and PD-1 interactions,[57] because PD-1 blockade failed to increase T cell recovery (Figures S4H and S4I).

To understand the mechanism behind this, we interrogated the TC1-tumor scRNA-seq data for death receptor ligands within cell-to-cell interaction networks (*Cd274*$^{+}$ TAMs vs. *Cd274*$^{-}$ TAMs). This analysis indeed indicated the presence of such ligands (*Tnf*, *Tweak*, and fatty acid synthase ligand [*Faslg*]) in *Cd274*$^{+}$ TAMs (Figure 4K). Such extrinsic ligands are well established to limit CD8^{+} T cells.[58,59] Flow cytometric analysis revealed that PD-L1^{+} TAMs contained higher levels of TNF/TRAIL (but not FASLG) than PD-L1^{-} TAMs, (Figure 4L). Importantly in TAM:T cell cocultures, the blockade of TRAIL, but not TNF, rescued the recovery of CD8^{+}T cells (Figure 4M). This suggested that PD-L1^{+} TAMs limit CD8^{+} T cell responses via TRAIL signaling.

PD-L1 blockade reduces accumulation of PD-L1^{+} TAMs

We wondered how PD-L1 blockade antagonized TAMs to allow recovery of T cells.[60,61] PD-L1 blockade did not significantly affect the M2-like (MHC-II^{LOW}CD206^{HIGH}) vs. M1-like (MHC-II^{HIGH}CD206^{LOW}) ratio in bone-marrow-derived macrophages (Figure S4J) or TAMs (Figure S4K). PD-L1 reportedly facilitates various pro-survival pathways.[60–64] Accordingly, a substantial fraction of TAMs died upon PD-L1 blockade (Figure 4N). Our scRNA-seq analysis of TC1 tumors found that *Cd274*$^{+}$ TAMs expressed various pro-survival genes (*Nfkbia*, *Rel*, *Socs3*, *Junb*, *Fos*, *Nfkb1*, *Map4k4*, *Mapk6*) (Figure 4O).[60–64] Remarkably, an *ex vivo* screening of TC1-tumoral TAMs with pharmacological inhibitors of nuclear factor κB (NF-κB), Janus kinase (JAK)/STAT, extracellular signal-regulated kinase (ERK), or phosphatidylinositol 3-kinase (PI3K) highlighted that NF-κB inhibition most proficiently reduced TAM survival (Figure 4P). Hence, we wondered if PD-L1 blockade was modulating the NF-κB pathway in macrophages. Hence, we used a J774 macrophage reporter system for NF-κB signaling. Indeed, PD-L1 blockade suppressed LPS-driven NF-κB activation (Figure S4L). Thus, PD-L1 blockade reduces PD-L1^{+} TAM survival.

DCvax-IT and PD-L1 blockade together suppress TC1 tumors by overcoming TAMs

We evaluated whether treating TC1 tumors with PD-L1 blockade can suppress tumor growth irrespective of DCvax-IT (Figure 5A).

Figure 5. DCvax-IT-mobilized PD-L1^{+} macrophages in LNs are blunted by DCvax-IT and anti-PD-L1 ICB

(A) TC1-tumor-bearing mice treated with DCvax-IT (day 9/6) and/or anti-PD-L1 (day 10/17). p values depict comparison vs. PBS-treated mice (PBS, n = 12; apoptosis/necroptosis DCvax-IT + anti-PD-L1, n = 12; area under curve, one-way ANOVA Kruskal-Wallis test).

(B) TC1-tumor-bearing mice treated with DCvax-IT (day 9/16) and/or anti-PD-L1 (day 10/17) in combination with clodronate liposomes (CLs). p values depict comparison vs. CL-treated mice (CL/apoptosis DCvax-IT/necroptosis DCvax-IT, n = 5; anti-PD-L1/apoptosis DCvax-IT + anti-PD-L1/necroptosis DCvax-IT + anti-PD-L1, n = 6; area under curve, one-way ANOVA, Dunnett's multiple comparisons test).

(C–H) Lymph node analysis of TC1-tumor-bearing mice, 3 days post treatment with DCvax-IT (with/without anti-PD-L1). (C) Frequency of PD-L1^{+} of CD11b^{+}F4/80^{+} cells. p values depict comparison vs. PBS-treated mice unless otherwise specified (n = 3–4; unpaired t test). (D) Frequency of M1 (MHC-II^{HIGH}CD206^{LOW}), M2 (MHC-II^{LOW}CD206^{HIGH}), or M0 (MHC-II^{LOW}CD206^{LOW}) macrophages. *p values depict comparison vs. M0 from PBS-treated mice. $^{\$}$p values depict comparison vs. M1 from PBS-treated mice (n = 6; two-tailed Student's t test). (E) IFNγ^{+}CD8^{+} T cells-to-TAMs ratio. p values depict comparison vs. PBS-treated mice (PBS/apoptosis DCvax-IT + anti-PD-L1, n = 3; anti-PD-L1/apoptosis DCvax-IT/necroptosis DCvax-IT + anti-PD-L1, n = 4, one-way ANOVA, Fischer's LSD test). (F) IFNγ^{+}CD4^{+} T cells-to-TAMs ratio. p values depict comparison vs. PBS-treated mice (PBS, n = 3; anti-PD-L1/apoptosis DCvax-IT/apoptosis DCvax-IT + anti-PD-L1/necroptosis DCvax-IT + anti-PD-L1, n = 4, one-way ANOVA, Fischer's LSD test). (G) IL2^{+}CD8^{+} T cells-to-TAMs ratio. p values depict comparison vs. PBS-treated mice (biological replicates; PBS/apoptosis DCvax-IT + anti-PD-L1, n = 3; anti-PD-L1/apoptosis DCvax-IT/necroptosis DCvax-IT + anti-PD-L1, n = 4, one-way ANOVA, Fischer's LSD test). (H) IL2^{+}CD4^{+} T cells-to-TAMs ratio. p values depict comparison to PBS-treated mice (PBS, n = 3; anti-PD-L1/apoptosis DCvax-IT/apoptosis DCvax-IT + anti-PD-L1/necroptosis DCvax-IT + anti-PD-L1, n = 4, one-way ANOVA, Fischer's LSD test).

(I and J) Frequency of PD-L1^{+} cells of CD11b^{+} F4/80^{+} cells after coculturing BMDMs with (I) WT or (J) *Ifnar1*$^{-/-}$ DCvax-IT for 48 h. p values depict comparison vs. untreated DCs (n = 3; one-way ANOVA, Dunnett's multiple comparisons test).

(K and L) TC1-tumor-bearing mice treated with (K) *Ccr7*$^{-/-}$ (L) or *Ifnar1*$^{-/-}$ DCvax-IT (day 9/16) and with anti-PD-L1 (day 10/17). p values depict comparison vs. PBS-treated mice (n = 6; area under curve; one-way ANOVA, Kruskal-Wallis test). Here, "n" represents biological replicates and error bars represent SEM. See Figures S4 and S5.

PD-L1 blockade indeed slightly (but not significantly) suppressed TC1-tumor growth (Figure 5A). In contrast, the combination of PD-L1 blockade with apoptotic^{TC1}/necroptotic^{TC1} DCvax-IT significantly reduced TC1-tumor growth (Figure 5A). This synergistic anti-tumor effect was also found in LLC tumors (Figure S4M).

Since the TAM modulation via PD-L1 was independent of PD-1, and more dominant than CSF1R, we combined PD-1 or CSF1R blockade with DCvax-IT. Unlike PD-L1 blockade (Figure 5A), neither PD-1 (Figure S4N) nor CSF1R (Figure S4O) blockade could synergize with DCvax-IT. Of note, CSF1R blockade did not suppress TC1-tumor growth despite achieving significant depletion of CSF1R$^+$ TAMs (Figure S4P), although without disturbing the general TAM compartment (Figure S4Q).

The results positioned PD-L1$^+$ macrophages as the key immuno-resistance barrier to DCvax-IT. To explore this conjecture, we depleted the macrophages with clodronate liposomes (CLs) (Figure 5B)[65] CL was used at a carefully titrated dose that depleted macrophages (Figure S4R) but not DCs (Figure S4S). CL based macrophage depletion non-significantly reduced the therapeutic response to PD-L1 blockade (Figure S4T). However, macrophage depletion was sufficient to significantly enhance the anti-tumor effect of DCvax-IT (Figure 5B). This combinatorial synergism between CL and DCvax-IT could not be further improved by PD-L1 blockade (Figure 5B).

Accordingly, under macrophage depletion, DCvax-IT boosted the intra-tumoral infiltration of CD8$^+$ T cells (Figure S4U). This stimulus to CD8$^+$ T cell infiltration was not further potentiated by PD-L1 blockade (Figure S4U). Of note, these data were not confounded by anti-PD-L1 antibody-driven Fc receptor crosslinking and NK cell-mediated antibody dependent cellular cytotoxicity[66] because depletion of NK cells via anti-NK1.1 antibody[67] (Figure S4V) or usage of anti-PD-L1 antibody engineered to possess a D265A mutation that minimizes its binding to Fc receptors[68] (Figure S4W) did not disrupt the synergism between PD-L1 blockade and DCvax-IT. In conclusion, DCvax-IT plus PD-L1 blockade suppressed TC1 tumors by antagonizing TAMs.

DCvax-IT induces PD-L1$^+$ macrophages in LNs and simultaneous PD-L1 blockade blunts them

Modus operandi of DC vaccines involves anti-tumor priming of LN T cells.[10,15,69] However, little is known about their impact on LN-associated macrophages (LAMs). Since DCvax-IT showed good LN homing, we investigated whether they might induce PD-L1$^+$ LAMs. We immunophenotyped the inguinal/axillary LNs of tumor-bearing mice (Figure 5C). While DCvax-IT did not directly cause a mobilization of macrophages (Figure S5A) or cDC1/cDC2 (Figures S5B and S5C) in LNs, it did induce an enrichment of PD-L1$^+$ LAMs (Figure 5C). Here, for immunophenotyping, we used a PD-L1 antibody recognizing another non-overlapping epitope than the therapeutic anti-PD-L1 antibody. A similar expansion was not observed for CSF1R$^+$ LAMs (Figure S5D), PD-L1$^+$cDC1/cDC2 (Figures S5E and S5F). However, DCvax-IT plus PD-L1 blockade strongly reduced the accumulation of not only PD-L1$^+$ LAMs (Figure 5C) but also macrophages (Figure S5A), cDC1/cDC2 (Figures S5B and S5C), CSF1R$^+$ LAMs (Figure S5D), and PD-L1$^+$cDC1/cDC2 (Figures S5E and S5F). The reduction of PD-L1$^+$ LAMs was observed at both percentages and absolute counts (Figure S5G). PD-L1 blockade plus DCvax-IT caused significant reduction in both M1-like/M2-like LAMs thereby "re-wiring" the compartment toward M0-like phenotype (MHC-II^{LOW}CD206^{LOW}) (Figure 5D). There was no clear increase in phenotypic-maturation of cDC1/cDC2 (Figures S5H and S5I). PD-L1$^+$ LAM enrichment also happened after vaccination with other DC preparations (especially the pro-inflammatory cytokine-based preparations) but not after PD-1 blockade (Figure S5J). DCvax-IT-induced increase in PD-L1$^+$ LAMs was also confirmed for LLC tumors (Figure S5K) but not for MC38 tumors (Figure S5L). Furthermore, combination with PD-L1 blockade prevented the accumulation of these LAMs in LLC tumors (Figure S5K).

Next, we analyzed the LN-associated T cells. None of the treatments caused an increase in CD4$^+$/CD8$^+$ T cells (Figures S5M and S5N). DCvax-IT or PD-L1 blockade alone did not increase IFNγ^+CD4$^+$/CD8$^+$ T cells (Figures 5E and 5F) or IL2$^+$CD4$^+$/CD8$^+$ T cells (Figures 5G and 5H). However, DCvax-IT plus PD-L1 blockade strongly mobilized IFNγ^+CD4$^+$/CD8$^+$ T cells (Figures 5E and 5F) and IL2$^+$CD4$^+$/CD8$^+$ T cells in LN (Figures 5G and 5H).

Subsequently, we wondered whether DCvax-IT was directly inducing PD-L1 on macrophages. Coculturing macrophages with DCvax-IT resulted in more PD-L1$^+$ macrophages (Figure 5I) but not CSF1R$^+$ macrophages (Figure S5O). Since DCvax-IT secreted several type I IFN/ISG-response-driven cytokines (Figure 2K) that can induce PD-L1,[61,70] we ablated this pathway via *Ifnar1*$^{-/-}$ DCvax-IT. *Ifnar1*$^{-/-}$ DCvax-IT failed to induce PD-L1 on macrophages (Figure 5J). In contrast to WT DCvax-IT, *Ccr7*$^{-/-}$ DCvax-IT (Figure 5K) or *Ifnar1*$^{-/-}$ DCvax-IT (Figure 5L) failed to synergize with PD-L1 blockade to mediate TC1-tumor reduction. This confirmed that DCvax-IT induces PD-L1$^+$ LAMs, which limits effector CD4$^+$/CD8$^+$ T cells, thus creating an immuno-resistant macrophage niche.

DCvax-IT mobilizes PD-L1$^+$ TAMs and combination with anti-PD-L1 ICB blunts them to promote anti-tumor T cell immunity

We wondered whether DCvax-IT also enhanced PD-L1$^+$ TAMs to weaken anti-tumor T cells. Indeed, DCvax-IT caused a significant enrichment of TAMs (Figure 6A) and PD-L1$^+$ TAMs (Figure 6B). Accordingly, DCvax-IT plus PD-L1 blockade prevented the accumulation of TAMs (Figure 6A) and PD-L1$^+$ TAMs (Figure 6B). This reduction was detected for both relative and absolute counts (Figure S6A). An increase in the CD8$^+$ T cell-to-TAM ratio was also observed (Figure 6C). Moreover, ELISA-based analysis of TAM lysates confirmed that combinatorial PD-L1 blockade caused a reduction of PD-L1 protein (Figure S6B). We did not see any differences in the abundance of DCs, cDC1/cDC2, PD-L1$^+$cDC1/cDC2 (Figures S6C–S6G), or their phenotypic maturation (Figures S6H–S6J). Similarly, there was no increase in PD-L1$^+$ fibroblasts (Figure S6K), PD-L1$^+$ endothelial cells (Figure S6L), or other tumoral cells (Figure S6M). Also, TC1 cancer cells did not express PD-L1/PD-L2 (Figure S6N). The DCvax-IT-induced increase in PD-L1$^+$ TAMs was cross-confirmed in LLC tumors (Figure S6O) but not MC38 tumors (Figure S6P). Expectedly, in DCvax-IT-treated LLC tumors, PD-L1

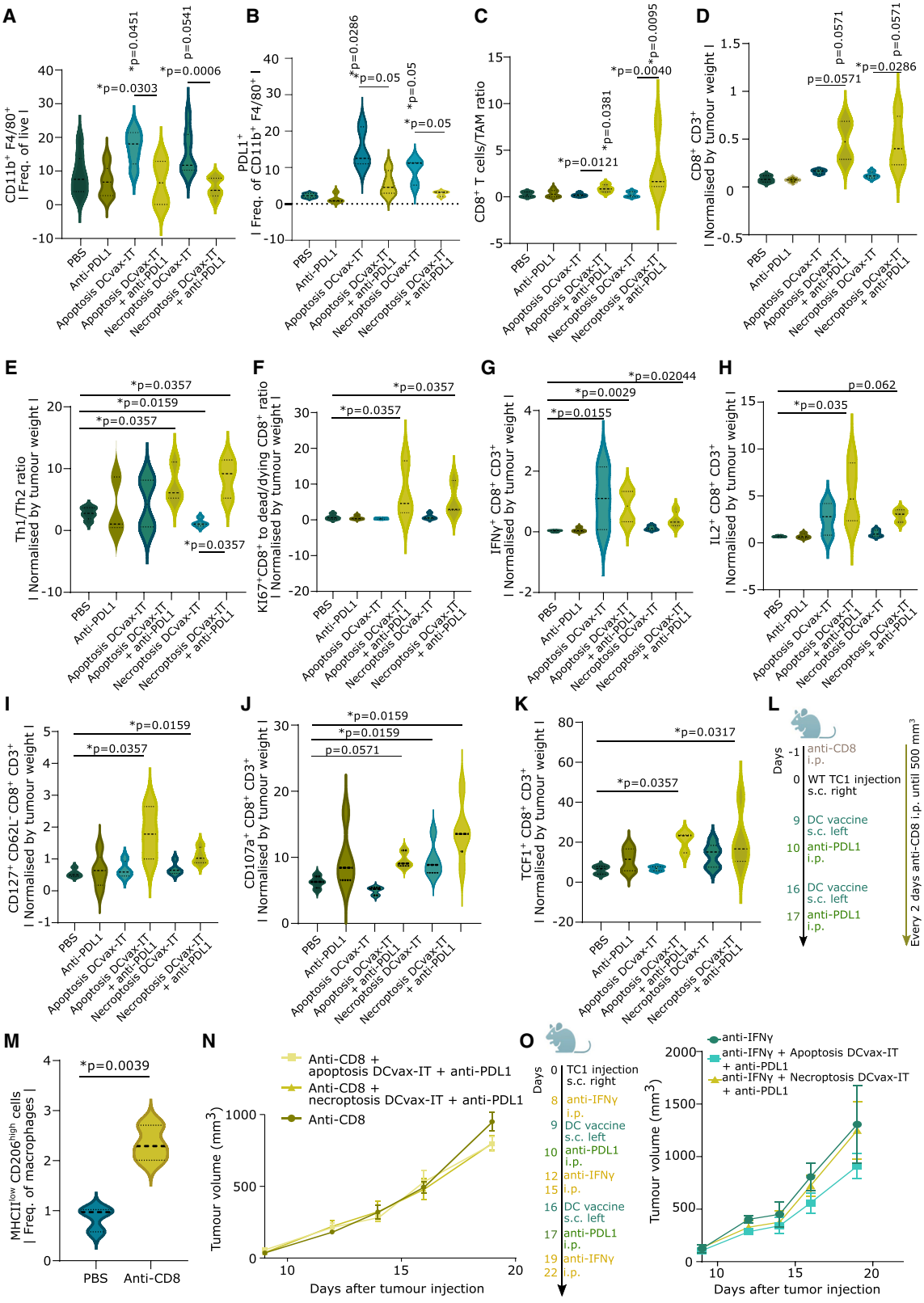

(legend on next page)

blockade blunted PD-L1$^+$ TAMs (Figure S6O). This emphasized the immunosuppressive relevance of PD-L1$^+$ TAMs.

Consequently, only DCvax-IT plus PD-L1 blockade caused a significant augmentation of CD8$^+$ T cells (Figure 6D). In contrast, all conditions caused a non-significant increase in CD4$^+$ T cell infiltrates (Figure S7A). Similarly, only the combinatorial regimen skewed the tumoral milieu toward higher Th1-to-Th1 ratio (Figure 6E), increased the ratio of proliferating Ki67$^+$CD8$^+$ T cells over dead/dying CD8$^+$ T cells (Figure 6F), and enhanced effector CD8$^+$ T cells,[2,4,71] i.e., effector IFNγ^+ (Figure 6G) or IL2$^+$ (Figure 6H) CD8$^+$ T cells, effector-memory CD127$^+$CD62L$^-$CD8$^+$ T cells (Figure 6I), and cytotoxic CD107a$^+$CD8$^+$ T cells (Figure 6J). The combination treatment also increased exhausted PD-1$^+$TIM3$^+$CD8$^+$ T cells (Figure S7B) and stem-like memory T cell factor (TCF1)$^+$CD8$^+$ T cells (Figure 6K) without increasing terminally differentiated eomesodermin (EOMES)$^+$TCF1$^-$CD8$^+$ T cells (Figure S7C).

To confirm the antagonistic relationship between M2-like TAMs vs. CD8$^+$ T lymphocytes, we depleted CD8$^+$ T cells via antibodies (Figure 6L). Interestingly, TC1 tumors depleted of CD8$^+$ T cells (Figure S7D) contained more M2-like TAMs (Figure 6M) and less M1-like TAMs (Figure S7E). This was accompanied by accelerated tumor growth (Figure S7F). Expectedly, the anti-tumor effect of DCvax-IT plus PD-L1 blockade disappeared in the absence of CD8$^+$ T cells (Figure 6N). Tumor T cell-derived IFNγ is a dominant inducer of PD-L1-signaling.[61] Accordingly, antibody-based neutralization of IFNγ also disrupted the synergism of DCvax-IT and PD-L1 blockade (Figure 6O).

Finally, we confirmed the pro-CD8$^+$ T cell role for DCvax-IT's type I IFN response and LN homing by immunophenotyping the tumors after the administration of *Ifnar1*$^{-/-}$ DCvax-IT or *Ccr7*$^{-/-}$ DCvax-IT plus PD-L1 blockade. Despite combination with PD-L1 blockade, *Ccr7*$^{-/-}$ DCvax-IT, or *Ifnar1*$^{-/-}$ DCvax-IT (Figure S7G) did not increase the number of tumor-infiltrating CD8$^+$ T cells. This confirmed that DCvax-IT mobilizes PD-L1$^+$ macrophage niche spanning both tumors and LNs thereby suppressing T cell immunity such that combination with PD-L1 blockade prevents the accumulation of these TAMs and revives anti-tumor T cells.

PD-L1 and TAM co-association is a negative prognostic niche in human cancers that specifically predicts clinical response to PD-L1 blockade

Bioinformatics analysis with 21 scRNA-seq datasets spanning 13 cancer types, 287 patients, and two species showed that TAMs where the most dominant source of *CD274* (Figure 7A) among various tumoral cells. We also explored the correlation of *CD274* with M1 vs. M2-like macrophages across the pan-cancer immune-landscape classes in TCGA. Interestingly, the more immunogenic C1/C2/C6 tumors showed a higher correlation between *CD274* and M1 macrophages (Figure 7B). Conversely, T cell-depleted C4/C5 tumors displayed a better correlation between *CD274* and M2-like macrophages (Figure 7B). Finally, in terms of survival impact, a TCGA-based pan-cancer multivariate prognostic analysis (19 cancer types, 8,493 patients) emphasized that, in most cancers, co-enrichment of *CD274* and macrophages associated with an increased hazard ratio (i.e., shorter overall survival) (Figure 7C).

Next, we determined if an M2-like PD-L1$^+$ TAM metagene in pre-treatment tumor transcriptomes can distinguish clinical responders from non-responders in an immunotherapy cohort integrating treatments with either PD-L1 blockade (454 patients, five cancer types) or PD-1 blockade (761 patients, 11 cancer types). Importantly, PD-L1$^+$ TAM metagene was significantly more expressed in patients responding to PD-L1 blockade (Figure 7D) than PD-1 blockade (Figure 7E). This correlation emphasized the interaction of TAMs with PD-L1 across a variety of different cancers.

DC vaccines mobilize lymphocyte-suppressive PD-L1$^+$ TAMs in glioblastoma

The preclinical observation of DC vaccine-induced T cell-suppressive PD-L1$^+$ TAMs called for functional validation in DC vaccinated patients. A cancer type distribution analysis of C4/C5 tumors confirmed that T cell-depleted tumors often are glioblastoma (GBM)/low-grade gliomas (LGGs) (Figure S7H).[4,72,73]

We accessed samples from the GlioVax clinical trial[38] (Table S3). GlioVax is a randomized phase II trial enrolling newly diagnosed GBM patients treated with tumor lysate-loaded DC vaccines combined with radiochemotherapy (Figure 7F).[38] DC vaccines indeed increased CD4$^+$/CD8$^+$ T cells (Figure 7G) and effector IFNγ^+CD4$^+$/CD8$^+$ T cells (Figure 7H) within GBM tissues from vaccinated patients. Interestingly, the DC vaccine also caused a significant increase in M2-like CD163$^+$CD14$^+$CD45$^+$ TAMs (Figure 7I). Moreover, the CD163$^+$ TAMs and CD8$^+$ T cells also showed spatially disconnected localizations (Figure 7J). Accordingly, a correlation analysis across 37 tumor regions from eight unvaccinated/vaccinated GBM patients highlighted an antagonistic relationship between

Figure 6. DCvax-IT-mobilized PD-L1$^+$ macrophages in tumors are blunted by DCvax-IT and anti-PD-L1 ICB

(A–C) Tumor infiltrating leukocyte (TIL) analysis of CD45$^+$ fraction from TC1 tumors (isolated on day 23 post injection) treated with DCvax-IT (day 9/16) and/or anti-PD-L1 (day 10/17). (A) Percentage of TAMs (CD11b$^+$F4/80$^+$), (B) percentage of PD-L1$^+$ TAMs, (C) CD8$^+$-to-TAM ratio. (A–C) p values depict comparison vs. PBS-treated mice unless otherwise specified (n = 3–9; Mann-Whitney test).

(D–K) TIL analysis of CD45$^+$ fraction from TC1 tumor (day 23 post injection) treated with DCvax-IT (day 9/16) with/without anti-PD-L1 (day 10/17). Normalized by tumor-weight. (D) CD8$^+$ T cells-to-TAM ratio. (E) Th1-to-Th2 ratio. (F) KI67$^+$CD8$^+$-to-dead CD8$^+$ ratio. (G) IFNγ^+CD8$^+$ T cells. (H) IL2$^+$CD8$^+$ T cells. (I) CD127$^+$CD62$^-$CD8$^+$ T cells. (J) CD107a$^+$CD8$^+$ T cells. (K) TCF$^+$CD8$^+$ cells. (D, E, F, and I–K) p values depict comparison vs. PBS-treated mice unless otherwise specified (n = 3–5; Mann-Whitney test). (G and H) p values depict comparison vs. PBS-treated mice unless otherwise specified (n = 3–4; one-way ANOVA, Kruskal-Wallis test).

(L–N) TC1-tumor-bearing mice treated with DCvax-IT (day 9/11), with anti-PD-L1 (day 10/11) and with anti-CD8 1 day pre-injection and every other day until 500 mm^3. p values depict comparison vs. PBS-treated mice unless otherwise specified. (M) %MHCII^{low}CD206^{high} of CD11b$^+$F4/80$^+$ in CD45$^+$ fraction from TC1 tumor (day 23 post injection) (n = 3; two-tailed Student's test). (N) Tumor volume curve (n = 7; area under curve; one-way ANOVA, Kruskal-Wallis test).

(O) TC1-tumor-bearing mice treated with DCvax-IT (day 9/16) and/or anti-PD-L1 ICB (day 10/17) in combination with anti-IFNγ antibody (day 8, 12, 15, 19, 22). p values depict comparison vs. PBS-treated mice (n = 4, area under curve, one-way ANOVA). Here, "n" represents biological replicates and error bars represent SEM. See also Figure S6.

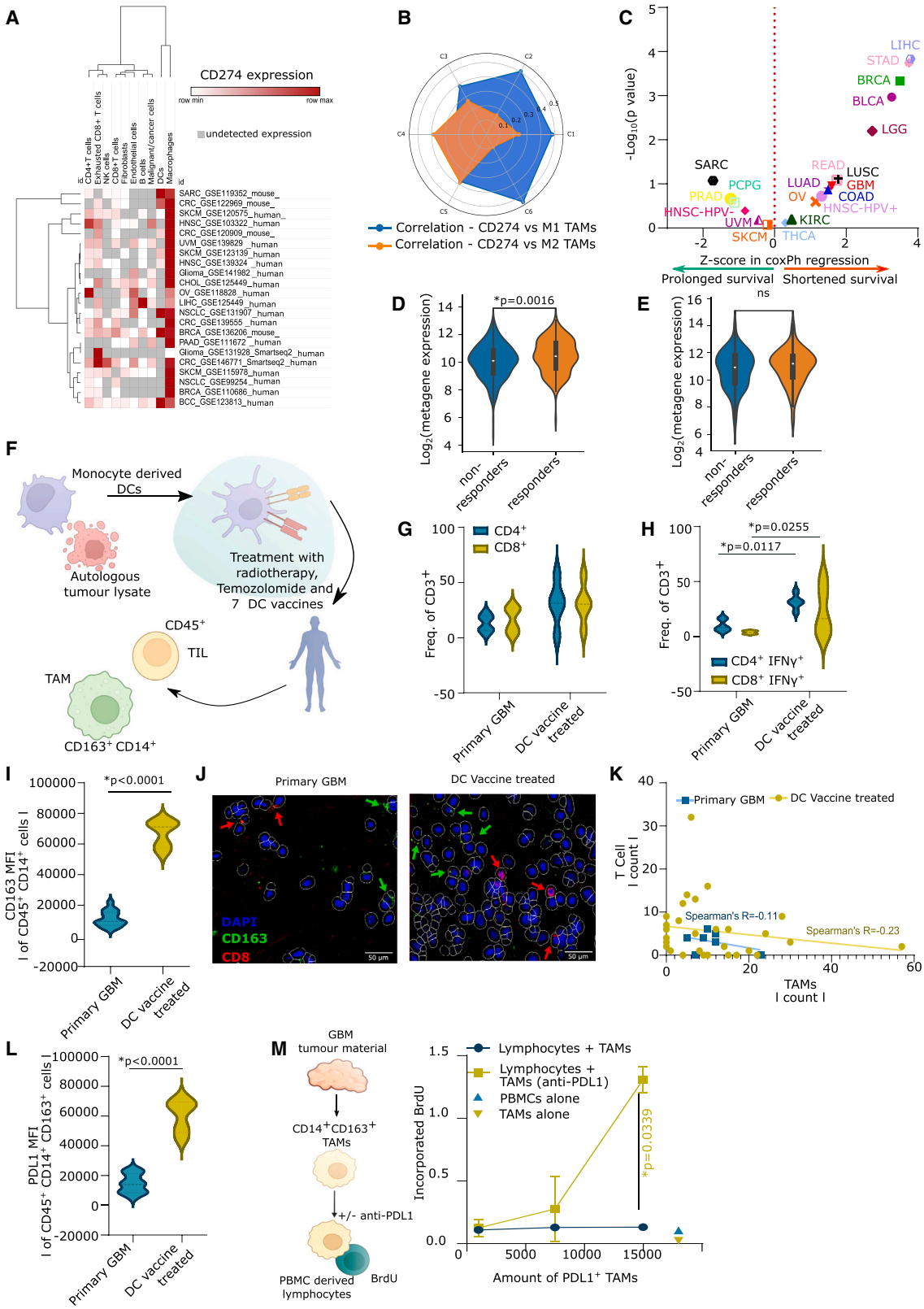

(legend on next page)

TAMs and CD8$^+$ T cells, which increased upon vaccination (Figure 7K).

In accord with our preclinical data, DC vaccination increased the frequency of PD-L1$^+$CD163$^+$ TAMs (Figure 7L) in GBM tissues. In the next step, we isolated GBM-infiltrating human PD-L1$^+$ TAMs and cocultured them at different densities with human allogeneic PBMC-derived lymphocytes in the presence or absence of PD-L1 blockade (Figure 7M). Remarkably, PD-L1 blockade stimulated lymphocyte proliferation, but only in the presence of PD-L1$^+$ TAMs, and this effect increased with higher densities of PD-L1$^+$ TAMs (Figure 7M). Of note, human GBM-infiltrating M2-like TAMs expressed significantly higher PD-L1 than CSF1R (Figure S7I). Altogether, these findings suggest that DC vaccination can elicit lymphocyte-suppressive PD-L1$^+$ TAMs in human GBM.

DISCUSSION

In this study, we found that the biggest limitation of human DC vaccines was not their maturation per se but their divergent functional states. In fact, we pinpointed the most immunogenic DC vaccine state (i.e., type I IFN/ISG response^{HIGH}), which is also associated with efficient antigen-directed immunity and favorable tumor responses in patients. Using this information, we designed a preclinical DCvax-IT. Although some studies have investigated the single-DC vaccine transcriptome,[23,74] to the best of our knowledge, none has used these data to drive the creation of an optimized preclinical DC vaccine.

Contrary to our expectations, DCvax-IT was suboptimal, because it facilitated the surge of PD-L1$^+$ LAMs via type I IFN/ISG response, rather than facilitating effector T cells. In parallel, DCvax-IT fueled preexisting T cell-suppressive PD-L1$^+$ TAMs. This created a strong immunosuppressive PD-L1$^+$ macrophage niche across both these anatomically distinct sites, which played a key role in DCvax-IT immunoresistance. Intriguingly PD-L1$^+$ macrophages suppressed CD8$^+$ T cells via TRAIL signaling. Fortunately, this immunosuppressive niche could be neutralized by PD-L1 blockade. In fact, it required a DCvax-IT plus PD-L1 blockade combination to neutralize PD-L1$^+$ LAMs in LNs and PD-L1$^+$ TAMs in the tumors, to unleash "systemic" anticancer T cell activity. The combination of DCvax-IT and PD-L1 blockade helped control the immuno-depleted TC1/LLC tumors. PD-L1 blockade reduced the accumulation of PD-L1$^+$ macrophages (possibly by modulating NF-κB signaling[75]).

These results have major implications for changing the fundamental outlook of how anticancer DC vaccines work. Currently, the literature consensus agrees that LNs serve solely as the sites of efficacious T cell priming for cancer antigens by the DCs. Our observations add some additional notions to this vision. Indeed, our findings suggest that DC vaccine-driven T cell-suppressive pathways are fueled by PD-L1$^+$ LAMs, and, together with simultaneous fueling of PD-L1$^+$ TAMs, this PD-L1 signaling counters the efficacy of DC vaccines. Moreover, it appears that this pathway is actionable, opening room for combinatorial immunotherapy opportunities.[76,77] Although anti-PD-L1 ICB is part of the clinically approved immunotherapy toolkit,[57,78] the proposal to combine DC vaccines with ICBs targeting PD-L1 (instead of PD-1) is important because almost all current clinical trials integrating ICBs with DC vaccines are prioritizing PD-1 blockage.[76]

Of note, we could confirm that DC vaccines potentiated lymphocyte-suppressive PD-L1$^+$ TAMs in patients with GBM, a prototypical T cell-depleted tumor. This, along with the data that the association of TAMs and PD-L1 has negative prognostic value and that a PD-L1$^+$ TAMs signature predicts positive patient responses to PD-L1 blockade, suggests that DC vaccine-driven

Figure 7. PD-L1$^+$ macrophages are mobilized by DC vaccines in GBM patients

(A) Expression of *CD274/cd274* (PD-L1) across indicated datasets (n = 287 patients).

(B) Correlation between *CD274* vs. M1/M2 macrophage fraction in TCGA cancer types (C1, n = 1,313; C2, n = 1,210, C3, n = 688; C4, n = 222, C5, n = 2; C6, n = 111).

(C) *Z* scores of CoxPH regression of *CD274*^{HIGH} macrophages^{HIGH} subgroups, correcting for age, gender, tumor-stage (bladder cancer/BLCA, n = 408; breast cancer/BRCA, n = 1,100; colon adenocarcinoma/COAD, n = 458; GBM, n = 153; head and neck cancer human papillomavirus$^-$/HNSC-HPV$^-$, n = 422; head and neck cancer human papillomavirus$^+$/HNSC-HPV$^+$, n = 98; kidney chromophobe/KICH, n = 66; kidney renal clear cell carcinoma/KIRC, n = 533; kidney renal papillary cell carcinoma/KIRP, n = 290; low-grade glioma/LGG, n = 516; liver cancer/LIHC, n = 371; lung adenocarcinoma/LUAD, n = 515; lung squamous cell carcinoma/LUSC, n = 501; ovarian cancer/OV, n = 303; pancreatic adenocarcinoma/PAAD, n = 179; pheochromocytoma/PCPG, n = 181; prostate adenocarcinoma/PRAD, n = 498; rectum adenocarcinoma/READ, n = 166; sarcoma/SARC, n = 260; melanoma/SKCM, n = 471; stomach adenocarcinoma/STAD, n = 415; thyroid carcinoma/THCA, n = 509; uveal melanoma/UVM, n = 80, Mantel-Cox test).

(D and E) log2(metagene expression) of CD274, CD163, CD14, and CD68. (D) Responders vs. non-responders to anti-PD-L1 (atezolizumab/durvalumab) (responders, n = 185 and non-responders, n = 269, where ureter/renal pelvis cancer n = 4, urothelial cancer n = 345, bladder cancer n = 31, esophageal cancer n = 72, renal cell carcinoma n = 2; Mann-Whitney U test). (E) Responders vs. non-responders to anti-PD-1 (nivolumab/pembrolizumab) (responders, n = 183 and non-responders, n = 323, where lung cancer n = 19, GBM n = 19, ureter/renal pelvis cancer n = 7, gastric cancer n = 45, colorectal cancer n = 5, melanoma n = 415, bladder cancer n = 59, hepatocellular carcinoma n = 22, breast cancer n = 14, renal cell carcinoma n = 31, head and neck cancer n = 110; Mann-Whitney U test).

(F–J) Analysis of CD45$^+$ fraction of primary and DC vaccinated GBM patients (NCT03395587). Tumor material from day of resection at first diagnosis (primary) or at recurrence after vaccination. (F) Overview of NCT03395587. (G) Frequency of CD4$^+$/CD8$^+$ of CD3$^+$ cells. (H) Frequency of IFNγ$^+$ of CD4$^+$/CD8$^+$CD3$^+$ T cells. (G and H) Primary, n = 6; progress vaccine, n = 5, two-way ANOVA, Bonferroni's multiple comparison.

(I) Mean fluorescent intensity of CD163 on CD14$^+$ cells. Primary, n = 15; recurrent DC vaccine, n = 5; two-tailed Student's t test.

(J and K) Immunohistochemistry of tumor slide from unvaccinated and DC vaccinated GBM patients (NCT03395587). (J) Representative images. (K) Correlation between TAM and T cell counts (n = 37 tumor regions from eight unvaccinated/vaccinated, Spearman's correlation).

(L) Mean fluorescent intensity of PD-L1 on CD14$^+$ cells. Primary, n = 15; recurrent DC vaccine, n = 5; two-tailed Student's *t* test.

(M) Bromodeoxyuridine incorporation in cocultures of PBMC-derived lymphocytes (CD14 depleted PBMC) and TAMs obtained from primary GBM samples with/without anti-PD-L1 blocking (n = 3; area-under-curve-driven two-tailed paired t test). Here, "n" represents different patients (biological replicates) and error bars represent SEM. See also Figure S7.

PD-L1^{+} TAMs could be used to predict poor clinical responses. This claim is substantiated by a recent clinical study documenting that DC vaccines showed higher efficacy in breast cancer patients with PD-L1^{-} tumors.[79]

In conclusion, our study shows that a type I IFN^{HIGH}DC vaccine state is necessary but not sufficient for inducing therapy-relevant anticancer immune responses. This is because DC vaccines paradoxically induce a self-inhibitory niche of T cell-suppressive PD-L1^{+} macrophages in LNs and tumors that form a barrier to efficacious activation of T cell immunity. This creates a DC vaccine-driven immuno-resistant niche that opens avenues for combinatorial immunotherapy.

Limitations of the study

More research is needed to fully decipher the molecular pathways behind PD-L1^{+} TAM-driven CD8^{+} T cell death and PD-L1 blockade driven suppression of TAM survival. Also, it would be relevant to test whether our proposed mechanisms work in GBM tumor models in mouse. Finally, a prospective trial combining DC vaccines with PD-L1 blockade in cancer patients will be necessary to fully confirm the clinical relevance of our proposed PD-L1^{+} LAM/TAM pathway and DC vaccine's maturation trajectories.

STAR★METHODS

Detailed methods are provided in the online version of this paper and include the following:

- KEY RESOURCES TABLE
- RESOURCE AVAILABILITY
  - Lead contact
  - Materials availability
  - Data and code availability
- EXPERIMENTAL MODEL AND STUDY PARTICIPANT DETAILS
  - Human subjects and ethics
  - Mice models
  - Cell lines
  - Cell line creation
- METHOD DETAILS
  - Cell death analysis
  - *In vitro* assays
  - Antibody array
  - Efferocytosis assay
  - 5-Bromo-2′-deoxyuridine assay (BrdU-assay)
  - Cell isolation
  - Human CD14^{+} CD163^{+} macrophages
  - Immunohistochemistry
  - In vivo experiments
  - In silico analyses
- QUANTIFICATION AND STATISTICAL ANALYSIS

SUPPLEMENTAL INFORMATION

Supplemental information can be found online at https://doi.org/10.1016/j.xcrm.2023.101377.

ACKNOWLEDGMENTS

We thank R. Vandenbroucke (UGent) for *Ifnar1*$^{-/-}$C57BL/6 mice and B. Lambrechts (UGent) for *Ccr7*$^{-/-}$C57BL/6 mice. We acknowledge AdLight Microscopy Core Facility (UKD) and KU Leuven Flow/Mass cytometry core facility. This study is supported by Research Foundation Flanders (G0B4620N, A.D.G.; EOS grant, 30837538/DECODE, A.D.G./J.B.), KU Leuven (C14/19/098; C3/21/037, A.D.G.), Kom op tegen Kanker (KOTK/2018/11509/1, S.D.V./A.D.G.) and VLIR-UOS (iBOF/21/048/'MIMICRY', A.D.G./S.T.). I.V. and J.S. are supported by FWO-SB PhD Fellowship (1S06821N) and KOTK EvDS PhD fellowship (projectID: 12699). S.T. is supported by FWO Senior Clinical Investigator award. M.C.S., M.R., and R.V.S. were supported by Federal Ministry of Education and Research (BMBF; grant #01KG1424). V.M. is supported by FWO PhD fellowship (11I7523N). G.K. is supported by Ligue Contre le Cancer, Agence National de la Recherche (ANR); AMMICa US23/CNRS UMS3655; Association pour la Recherche sur le Cancer; Cancéropôle Île-de-France; Fondation pour la Recherche Médicale; Elior donation; Equipex Onco-Pheno-Screen; European Joint Programme on Rare Diseases (EJPRD); ERC Advanced Investigator Award (ERC-2021-A.D.G., ICD-Cancer, 101052444), EU Horizon 2020 Projects Oncobiome, Prevalung (101095604) and Crimson; Institut National Du Cancer; Institut Universitaire de France; Labex Immuno-Oncology (ANR-18-IDEX-0001); Cancer Research ASPIRE Award (Mark Foundation); RHU Immunolife; Seerave Foundation; SIRIC Stratified Oncology Cell DNA Repair and Tumor Immune Elimination (SOCRATE); SIRIC Cancer Research and Personalized Medicine (CARPEM); and IdEx Université de Paris ANR-18-IDEX-0001.

AUTHOR CONTRIBUTIONS

J.S. was lead experimental researcher. S.N. and D.M.B. did bioinformatics/biostatistics. I.V., J.G., R.S.L., A.C., V.M., P.L., L.Z., O.K., G.K., L.B., A.Z.Z., M.R., A.C., and S.S. performed crucial experiments. A.D., M.K., J.F., M.S., M.R., C.K.T., and R.V.S. analyzed GBM-patient samples. G.K. rewrote sizable manuscript portions. S.D.V., J.B., and S.T. helped with data interpretation and manuscript writing. A.D.G. and R.V.S. supplied senior supervision and critical manuscript revision. A.D.G. was principal investigator, coordinated and supervised the entire project, and wrote the manuscript.

DECLARATION OF INTERESTS

A.D.G. received honoraria/funding from Boehringer Ingelheim, Miltenyi Biotec, Novigenix, SOTIO, and IsoPlexis.

Received: August 22, 2022
Revised: August 23, 2023
Accepted: December 18, 2023
Published: January 16, 2024

REFERENCES

1. Sharma, P., and Allison, J.P. (2020). Dissecting the mechanisms of immune checkpoint therapy. Nat. Rev. Immunol. *20*, 75–76.
2. Blank, C.U., Haining, W.N., Held, W., Hogan, P.G., Kallies, A., Lugli, E., Lynn, R.C., Philip, M., Rao, A., Restifo, N.P., et al. (2019). Defining "T cell exhaustion". Nat. Rev. Immunol. *19*, 665–674.
3. Thommen, D.S., and Schumacher, T.N. (2018). T cell dysfunction in cancer. Cancer Cell *33*, 547–562.
4. Naulaerts, S., Datsi, A., Borras, D.M., Antoranz Martinez, A., Messiaen, J., Vanmeerbeek, I., Sprooten, J., Laureano, R.S., Govaerts, J., Panovska, D., et al. (2023). Multiomics and spatial mapping characterizes human CD8+ T cell states in cancer. Sci. Transl. Med. *15*, eadd1016.
5. Borras, D.M., Verbandt, S., Ausserhofer, M., Sturm, G., Lim, J., Laureano, R.S., Vanmeerbeek, I., Sprooten, J., Hong, Y., Wall, R., et al. (2023). Single cell dynamics of tumour specificity vs. bystander activity

in CD8+T cells define the diverse immune landscapes in colorectal cancer. Cell Discov. *9*, 114.

6. Nakamura, K., and Smyth, M.J. (2020). Myeloid immunosuppression and immune checkpoints in the tumor microenvironment. Cell. Mol. Immunol. *17*, 1–12.
7. Beyranvand Nejad, E., Labrie, C., Abdulrahman, Z., van Elsas, M.J., Rademaker, E., Kleinovink, J.W., van der Sluis, T.C., van Duikeren, S., Teunisse, A.F.A.S., Jochemsen, A.G., et al. (2020). Lack of myeloid cell infiltration as an acquired resistance strategy to immunotherapy. J. Immunother. Cancer *8*, e001326.
8. Goswami, S., Anandhan, S., Raychaudhuri, D., and Sharma, P. (2023). Myeloid cell-targeted therapies for solid tumours. Nat. Rev. Immunol. *23*, 106–120.
9. Vanmeerbeek, I., Borras, D.M., Sprooten, J., Bechter, O., Tejpar, S., and Garg, A.D. (2021). Early memory differentiation and cell death resistance in T cells predicts melanoma response to sequential anti-CTLA4 and anti-PD1 immunotherapy. Gene Immun. *22*, 108–119.
10. Perez, C.R., and De Palma, M. (2019). Engineering dendritic cell vaccines to improve cancer immunotherapy. Nat. Commun. *10*, 5408.
11. Anguille, S., Smits, E.L., Lion, E., van Tendeloo, V.F., and Berneman, Z.N. (2014). Clinical use of dendritic cells for cancer therapy. Lancet Oncol. *15*, e257–e267.
12. van Beek, J.J.P., Flórez-Grau, G., Gorris, M.A.J., Mathan, T.S.M., Schreibelt, G., Bol, K.F., Textor, J., and de Vries, I.J.M. (2020). Human pDCs Are Superior to cDC2s in Attracting Cytolytic Lymphocytes in Melanoma Patients Receiving DC Vaccination. Cell Rep. *30*, 1027–1038.e4.
13. Wculek, S.K., Cueto, F.J., Mujal, A.M., Melero, I., Krummel, M.F., and Sancho, D. (2020). Dendritic cells in cancer immunology and immunotherapy. Nat. Rev. Immunol. *20*, 7–24.
14. Kvedaraite, E., and Ginhoux, F. (2022). Human dendritic cells in cancer. Sci. Immunol. *7*, eabm9409.
15. Garg, A.D., Coulie, P.G., Van den Eynde, B.J., and Agostinis, P. (2017). Integrating Next-Generation Dendritic Cell Vaccines into the Current Cancer Immunotherapy Landscape. Trends Immunol. *38*, 577–593.
16. Fucikova, J., Hensler, M., Kasikova, L., Lanickova, T., Pasulka, J., Rakova, J., Drozenova, J., Fredriksen, T., Hraska, M., Hrnciarova, T., et al. (2022). An autologous dendritic cell vaccine promotes anticancer immunity in ovarian cancer patients with low mutational burden and cold tumors. Clin. Cancer Res. *28*, 3053–3065.
17. Thorsson, V., Gibbs, D.L., Brown, S.D., Wolf, D., Bortone, D.S., Ou Yang, T.-H., Porta-Pardo, E., Gao, G.F., Plaisier, C.L., Eddy, J.A., et al. (2018). The immune landscape of cancer. Immunity *48*, 812–830.e14.
18. Eddy, J.A., Thorsson, V., Lamb, A.E., Gibbs, D.L., Heimann, C., Yu, J.X., Chung, V., Chae, Y., Dang, K., Vincent, B.G., et al. (2020). CRI iAtlas: an interactive portal for immuno-oncology research. F1000Res. *9*, 1028.
19. Ramilowski, J.A., Goldberg, T., Harshbarger, J., Kloppmann, E., Lizio, M., Satagopam, V.P., Itoh, M., Kawaji, H., Carninci, P., Rost, B., and Forrest, A.R.R. (2015). A draft network of ligand-receptor-mediated multicellular signalling in human. Nat. Commun. *6*, 7866.
20. Garg, A.D., and Agostinis, P. (2017). Cell death and immunity in cancer: From danger signals to mimicry of pathogen defense responses. Immunol. Rev. *280*, 126–148.
21. Mermel, C.H., Schumacher, S.E., Hill, B., Meyerson, M.L., Beroukhim, R., and Getz, G. (2011). GISTIC2.0 facilitates sensitive and confident localization of the targets of focal somatic copy-number alteration in human cancers. Genome Biol. *12*, R41.
22. Sprooten, J., Agostinis, P., and Garg, A.D. (2019). Type I interferons and dendritic cells in cancer immunotherapy. Int. Rev. Cell Mol. Biol. *348*, 217–262.
23. Castiello, L., Sabatino, M., Ren, J., Terabe, M., Khuu, H., Wood, L.V., Berzofsky, J.A., and Stroncek, D.F. (2017). Expression of CD14, IL10, and Tolerogenic Signature in Dendritic Cells Inversely Correlate with Clinical and Immunologic Response to TARP Vaccination in Prostate Cancer Patients. Clin. Cancer Res. *23*, 3352–3364.
24. Chen, H., Albergante, L., Hsu, J.Y., Lareau, C.A., Lo Bosco, G., Guan, J., Zhou, S., Gorban, A.N., Bauer, D.E., Aryee, M.J., et al. (2019). Single-cell trajectories reconstruction, exploration and mapping of omics data with STREAM. Nat. Commun. *10*, 1903.
25. Maier, B., Leader, A.M., Chen, S.T., Tung, N., Chang, C., LeBerichel, J., Chudnovskiy, A., Maskey, S., Walker, L., Finnigan, J.P., et al. (2020). A conserved dendritic-cell regulatory program limits antitumour immunity. Nature *580*, 257–262.
26. Echebli, N., Tchitchek, N., Dupuy, S., Bruel, T., Peireira Bittencourt Passaes, C., Bosquet, N., Le Grand, R., Bourgeois, C., Favier, B., Cheynier, R., et al. (2018). Stage-specific IFN-induced and IFN gene expression reveal convergence of type I and type II IFN and highlight their role in both acute and chronic stage of pathogenic SIV infection. PLoS One *13*, e0190334.
27. Mosely, S.I.S., Prime, J.E., Sainson, R.C.A., Koopmann, J.-O., Wang, D.Y.Q., Greenawalt, D.M., Ahdesmaki, M.J., Leyland, R., Mullins, S., Pacelli, L., et al. (2017). Rational selection of syngeneic preclinical tumor models for immunotherapeutic drug discovery. Cancer Immunol. Res. *5*, 29–41.
28. Sprooten, J., Vankerckhoven, A., Vanmeerbeek, I., Borras, D.M., Berckmans, Y., Wouters, R., Laureano, R.S., Baert, T., Boon, L., Landolfo, C., et al. (2021). Peripherally-driven myeloid NFkB and IFN/ISG responses predict malignancy risk, survival, and immunotherapy regime in ovarian cancer. J. Immunother. Cancer *9*, e003609.
29. Smahel, M., Sobotková, E., Bubeník, J., Símová, J., Zák, R., Ludviková, V., Hájková, R., Kovarík, J., Jelínek, F., Povýsil, C., et al. (2001). Metastatic MHC class I-negative mouse cells derived by transformation with human papillomavirus type 16. Br. J. Cancer *84*, 374–380.
30. Efremova, M., Rieder, D., Klepsch, V., Charoentong, P., Finotello, F., Hackl, H., Hermann-Kleiter, N., Löwer, M., Baier, G., Krogsdam, A., and Trajanoski, Z. (2018). Targeting immune checkpoints potentiates immunoediting and changes the dynamics of tumor evolution. Nat. Commun. *9*, 32.
31. Garg, A.D., Vandenberk, L., Koks, C., Verschuere, T., Boon, L., Van Gool, S.W., and Agostinis, P. (2016). Dendritic cell vaccines based on immunogenic cell death elicit danger signals and T cell-driven rejection of high-grade glioma. Sci. Transl. Med. *8*, 328ra27.
32. Galluzzi, L., Vitale, I., Warren, S., Adjemian, S., Agostinis, P., Martinez, A.B., Chan, T.A., Coukos, G., Demaria, S., Deutsch, E., et al. (2020). Consensus guidelines for the definition, detection and interpretation of immunogenic cell death. J. Immunother. Cancer *8*, e000337.
33. Galluzzi, L., Vitale, I., Aaronson, S.A., Abrams, J.M., Adam, D., Agostinis, P., Alnemri, E.S., Altucci, L., Amelio, I., Andrews, D.W., et al. (2018). Molecular mechanisms of cell death: recommendations of the Nomenclature Committee on Cell Death 2018. Cell Death Differ. *25*, 486–541.
34. Yang, H., Ma, Y., Chen, G., Zhou, H., Yamazaki, T., Klein, C., Pietrocola, F., Vacchelli, E., Souquere, S., Sauvat, A., et al. (2016). Contribution of RIP3 and MLKL to immunogenic cell death signaling in cancer chemotherapy. OncoImmunology *5*, e1149673.
35. Yi, F., Frazzette, N., Cruz, A.C., Klebanoff, C.A., and Siegel, R.M. (2018). Beyond cell death: new functions for TNF family cytokines in autoimmunity and tumor immunotherapy. Trends Mol. Med. *24*, 642–653.
36. Takahashi, N., Duprez, L., Grootjans, S., Cauwels, A., Nerinckx, W., DuHadaway, J.B., Goossens, V., Roelandt, R., Van Hauwermeiren, F., Libert, C., et al. (2012). Necrostatin-1 analogues: critical issues on the specificity, activity and in vivo use in experimental disease models. Cell Death Dis. *3*, e437.
37. Sprooten, J., Ceusters, J., Coosemans, A., Agostinis, P., De Vleeschouwer, S., Zitvogel, L., Kroemer, G., Galluzzi, L., and Garg, A.D. (2019). Trial watch: dendritic cell vaccination for cancer immunotherapy. OncoImmunology *8*, e1638212.

38. Rapp, M., Grauer, O.M., Kamp, M., Sevens, N., Zotz, N., Sabel, M., and Sorg, R.V. (2018). A randomized controlled phase II trial of vaccination with lysate-loaded, mature dendritic cells integrated into standard radiochemotherapy of newly diagnosed glioblastoma (GlioVax): study protocol for a randomized controlled trial. Trials *19*, 293.

39. Wu, X., Xu, F., Liu, J., and Wang, G. (2017). Comparative study of dendritic cells matured by using IL-1β, IL-6, TNF-α and prostaglandins E2 for different time span. Exp. Ther. Med. *14*, 1389–1394.

40. Brabants, E., Heyns, K., De Smet, S., Devreker, P., Ingels, J., De Cabooter, N., Debacker, V., Dullaers, M., VAN Meerbeeck, J.P., Vandekerckhove, B., and Vermaelen, K.Y. (2018). An accelerated, clinical-grade protocol to generate high yields of type 1-polarizing messenger RNA-loaded dendritic cells for cancer vaccination. Cytotherapy *20*, 1164–1181.

41. Nava, S., Dossena, M., Pogliani, S., Pellegatta, S., Antozzi, C., Baggi, F., Gellera, C., Pollo, B., Parati, E.A., Finocchiaro, G., and Frigerio, S. (2012). An optimized method for manufacturing a clinical scale dendritic cell-based vaccine for the treatment of glioblastoma. PLoS One *7*, e52301.

42. Biscari, L., Kaufman, C.D., Farré, C., Huhn, V., Pacini, M.F., Balbi, C.B., Gómez, K.A., Pérez, A.R., and Alloatti, A. (2022). Immunization With Lipopolysaccharide-Activated Dendritic Cells Generates a Specific CD8+ T Cell Response That Confers Partial Protection Against Infection With Trypanosoma cruzi. Front. Cell. Infect. Microbiol. *12*, 897133.

43. Frasca, L., Nasso, M., Spensieri, F., Fedele, G., Palazzo, R., Malavasi, F., and Ausiello, C.M. (2008). IFN-gamma arms human dendritic cells to perform multiple effector functions. J. Immunol. *180*, 1471–1481.

44. Chiang, C.L.-L., Kandalaft, L.E., Tanyi, J., Hagemann, A.R., Motz, G.T., Svoronos, N., Montone, K., Mantia-Smaldone, G.M., Smith, L., Nisenbaum, H.L., et al. (2013). A dendritic cell vaccine pulsed with autologous hypochlorous acid-oxidized ovarian cancer lysate primes effective broad antitumor immunity: from bench to bedside. Clin. Cancer Res. *19*, 4801–4815.

45. Jin, Y., Mu, Y., Zhang, S., Li, P., and Wang, F. (2020). Preparation and evaluation of the adjuvant effect of curdlan sulfate in improving the efficacy of dendritic cell-based vaccine for antitumor immunotherapy. Int. J. Biol. Macromol. *146*, 273–284.

46. Chieochansin, T., Thepmalee, C., Grainok, J., Junking, M., and Yenchitsomanus, P.-T. (2019). Cytolytic Activity of Effector T-lymphocytes Against Hepatocellular Carcinoma is Improved by Dendritic Cells Pulsed with Pooled Tumor Antigens. Sci. Rep. *9*, 17668.

47. Imai, K., Minamiya, Y., Koyota, S., Ito, M., Saito, H., Sato, Y., Motoyama, S., Sugiyama, T., and Ogawa, J.-I. (2012). Inhibition of dendritic cell migration by transforming growth factor-β1 increases tumor-draining lymph node metastasis. J. Exp. Clin. Cancer Res. *31*, 3.

48. Ito, M., Minamiya, Y., Kawai, H., Saito, S., Saito, H., Nakagawa, T., Imai, K., Hirokawa, M., and Ogawa, J.i. (2006). Tumor-derived TGFbeta-1 induces dendritic cell apoptosis in the sentinel lymph node. J. Immunol. *176*, 5637–5643.

49. Ivashkiv, L.B., and Donlin, L.T. (2014). Regulation of type I interferon responses. Nat. Rev. Immunol. *14*, 36–49.

50. Bruchard, M., Geindreau, M., Perrichet, A., Truntzer, C., Ballot, E., Boidot, R., Racoeur, C., Barsac, E., Chalmin, F., Hibos, C., et al. (2022). Recruitment and activation of type 3 innate lymphoid cells promote antitumor immune responses. Nat. Immunol. *23*, 262–274.

51. Yu, Y.-Q., Thonn, V., Patankar, J.V., Thoma, O.-M., Waldner, M., Zielinska, M., Bao, L.-L., Gonzalez-Acera, M., Wallmüller, S., Engel, F.B., et al. (2022). SMYD2 targets RIPK1 and restricts TNF-induced apoptosis and necroptosis to support colon tumor growth. Cell Death Dis. *13*, 52.

52. Vanmeerbeek, I., Govaerts, J., Laureano, R.S., Sprooten, J., Naulaerts, S., Borras, D.M., Laoui, D., Mazzone, M., Van Ginderachter, J.A., and Garg, A.D. (2022). The Interface of Tumour-Associated Macrophages with Dying Cancer Cells in Immuno-Oncology. Cells *11*.

53. Zhu, J., Naulaerts, S., Boudhan, L., Martin, M., Gatto, L., and Van den Eynde, B.J. (2023). Tumour immune rejection triggered by activation of α2-adrenergic receptors. Nature *618*, 607–615.

54. Jin, S., Guerrero-Juarez, C.F., Zhang, L., Chang, I., Ramos, R., Kuan, C.-H., Myung, P., Plikus, M.V., and Nie, Q. (2021). Inference and analysis of cell-cell communication using CellChat. Nat. Commun. *12*, 1088.

55. Vandenbon, A., Dinh, V.H., Mikami, N., Kitagawa, Y., Teraguchi, S., Ohkura, N., and Sakaguchi, S. (2016). Immuno-Navigator, a batch-corrected coexpression database, reveals cell type-specific gene networks in the immune system. Proc. Natl. Acad. Sci. USA *113*, E2393–E2402.

56. Shan, T., Chen, S., Chen, X., Wu, T., Yang, Y., Li, S., Ma, J., Zhao, J., Lin, W., Li, W., et al. (2020). M2-TAM subsets altered by lactic acid promote T-cell apoptosis through the PD-L1/PD-1 pathway. Oncol. Rep. *44*, 1885–1894.

57. Wei, S.C., Duffy, C.R., and Allison, J.P. (2018). Fundamental mechanisms of immune checkpoint blockade therapy. Cancer Discov. *8*, 1069–1086.

58. Zhu, J., Powis de Tenbossche, C.G., Cané, S., Colau, D., van Baren, N., Lurquin, C., Schmitt-Verhulst, A.-M., Liljeström, P., Uyttenhove, C., and Van den Eynde, B.J. (2017). Resistance to cancer immunotherapy mediated by apoptosis of tumor-infiltrating lymphocytes. Nat. Commun. *8*, 1404.

59. Janssen, E.M., Droin, N.M., Lemmens, E.E., Pinkoski, M.J., Bensinger, S.J., Ehst, B.D., Griffith, T.S., Green, D.R., and Schoenberger, S.P. (2005). CD4+ T-cell help controls CD8+ T-cell memory via TRAIL-mediated activation-induced cell death. Nature *434*, 88–93.

60. Hartley, G.P., Chow, L., Ammons, D.T., Wheat, W.H., and Dow, S.W. (2018). Programmed Cell Death Ligand 1 (PD-L1) Signaling Regulates Macrophage Proliferation and Activation. Cancer Immunol. Res. *6*, 1260–1273.

61. Cha, J.-H., Chan, L.-C., Li, C.-W., Hsu, J.L., and Hung, M.-C. (2019). Mechanisms Controlling PD-L1 Expression in Cancer. Mol. Cell *76*, 359–370.

62. Escors, D., Gato-Cañas, M., Zuazo, M., Arasanz, H., García-Granda, M.J., Vera, R., and Kochan, G. (2018). The intracellular signalosome of PD-L1 in cancer cells. Signal Transduct. Targeted Ther. *3*, 26.

63. Gato-Cañas, M., Zuazo, M., Arasanz, H., Ibañez-Vea, M., Lorenzo, L., Fernandez-Hinojal, G., Vera, R., Smerdou, C., Martisova, E., Arozarena, I., et al. (2017). PDL1 Signals through Conserved Sequence Motifs to Overcome Interferon-Mediated Cytotoxicity. Cell Rep. *20*, 1818–1829.

64. Cao, H., Xiang, Y., Zhang, S., Chao, Y., Guo, J., Ho, J.W.K., Huang, Y., Liu, P., and Sugimura, R. (2022). PD-L1 regulates inflammatory macrophage development from human pluripotent stem cells by maintaining interferon-gamma signal. Preprint at bioRxiv.

65. Nguyen, T., Du, J., and Li, Y.C. (2021). A protocol for macrophage depletion and reconstitution in a mouse model of sepsis. STAR Protoc. *2*, 101004.

66. de Taeye, S.W., Bentlage, A.E.H., Mebius, M.M., Meesters, J.I., Lissenberg-Thunnissen, S., Falck, D., Sénard, T., Salehi, N., Wuhrer, M., Schuurman, J., et al. (2020). FcγR binding and ADCC activity of human igg allotypes. Front. Immunol. *11*, 740.

67. Hua, Y., Vella, G., Rambow, F., Allen, E., Antoranz Martinez, A., Duhamel, M., Takeda, A., Jalkanen, S., Junius, S., Smeets, A., et al. (2022). Cancer immunotherapies transition endothelial cells into HEVs that generate TCF1+ T lymphocyte niches through a feed-forward loop. Cancer Cell *40*, 1600–1618.e10.

68. Schofield, D.J., Percival-Alwyn, J., Rytelewski, M., Hood, J., Rothstein, R., Wetzel, L., McGlinchey, K., Adjei, G., Watkins, A., Machiesky, L., et al. (2021). Activity of murine surrogate antibodies for durvalumab and tremelimumab lacking effector function and the ability to deplete regulatory T cells in mouse models of cancer. mAbs *13*, 1857100.

69. Sabado, R.L., Balan, S., and Bhardwaj, N. (2017). Dendritic cell-based immunotherapy. Cell Res. *27*, 74–95.

70. Zerdes, I., Matikas, A., Bergh, J., Rassidakis, G.Z., and Foukakis, T. (2018). Genetic, transcriptional and post-translational regulation of the programmed death protein ligand 1 in cancer: biology and clinical correlations. Oncogene *37*, 4639–4661.

71. McLane, L.M., Abdel-Hakeem, M.S., and Wherry, E.J. (2019). CD8 T cell exhaustion during chronic viral infection and cancer. Annu. Rev. Immunol. *37*, 457–495.

72. Pombo Antunes, A.R., Scheyltjens, I., Lodi, F., Messiaen, J., Antoranz, A., Duerinck, J., Kancheva, D., Martens, L., De Vlaminck, K., Van Hove, H., et al. (2021). Single-cell profiling of myeloid cells in glioblastoma across species and disease stage reveals macrophage competition and specialization. Nat. Neurosci. *24*, 595–610.

73. Woroniecka, K., Chongsathidkiet, P., Rhodin, K., Kemeny, H., Dechant, C., Farber, S.H., Elsamadicy, A.A., Cui, X., Koyama, S., Jackson, C., et al. (2018). T-Cell Exhaustion Signatures Vary with Tumor Type and Are Severe in Glioblastoma. Clin. Cancer Res. *24*, 4175–4186.

74. Maurer, D.M., Adamik, J., Santos, P.M., Shi, J., Shurin, M.R., Kirkwood, J.M., Storkus, W.J., and Butterfield, L.H. (2020). Dysregulated NF-κB-Dependent ICOSL Expression in Human Dendritic Cell Vaccines Impairs T-cell Responses in Patients with Melanoma. Cancer Immunol. Res. *8*, 1554–1567.

75. Liu, X., Hogg, G.D., and DeNardo, D.G. (2021). Rethinking immune checkpoint blockade: "Beyond the T cell". J. Immunother. Cancer *9*, e001460.

76. Laureano, R.S., Sprooten, J., Vanmeerbeerk, I., Borras, D.M., Govaerts, J., Naulaerts, S., Berneman, Z.N., Beuselinck, B., Bol, K.F., Borst, J., et al. (2022). Trial watch: Dendritic cell (DC)-based immunotherapy for cancer. OncoImmunology *11*, 2096363.

77. Garg, A.D. (2023). The dynamic interface of genetics and immunity: toward future horizons in health & disease. Gene Immun. *24*, 155–158.

78. Chae, Y.K., Arya, A., Iams, W., Cruz, M.R., Chandra, S., Choi, J., and Giles, F. (2018). Current landscape and future of dual anti-CTLA4 and PD-1/PD-L1 blockade immunotherapy in cancer; lessons learned from clinical trials with melanoma and non-small cell lung cancer (NSCLC). J. Immunother. Cancer *6*, 39.

79. Santisteban, M., Solans, B.P., Hato, L., Urrizola, A., Mejías, L.D., Salgado, E., Sánchez-Bayona, R., Toledo, E., Rodríguez-Spiteri, N., Olartecoechea, B., et al. (2021). Final results regarding the addition of dendritic cell vaccines to neoadjuvant chemotherapy in early HER2-negative breast cancer patients: clinical and translational analysis. Ther. Adv. Med. Oncol. *13*, 17588359211064653.

80. Gubin, M.M., Esaulova, E., Ward, J.P., Malkova, O.N., Runci, D., Wong, P., Noguchi, T., Arthur, C.D., Meng, W., Alspach, E., et al. (2018). High-Dimensional Analysis Delineates Myeloid and Lymphoid Compartment Remodeling during Successful Immune-Checkpoint Cancer Therapy. Cell *175*, 1014–1030.e19.

81. Kurtulus, S., Madi, A., Escobar, G., Klapholz, M., Nyman, J., Christian, E., Pawlak, M., Dionne, D., Xia, J., Rozenblatt-Rosen, O., et al. (2019). Checkpoint Blockade Immunotherapy Induces Dynamic Changes in PD-1^{-}CD8^{+} Tumor-Infiltrating T Cells. Immunity *50*, 181–194.e6.

82. Sade-Feldman, M., Yizhak, K., Bjorgaard, S.L., Ray, J.P., de Boer, C.G., Jenkins, R.W., Lieb, D.J., Chen, J.H., Frederick, D.T., Barzily-Rokni, M., et al. (2018). Defining T Cell States Associated with Response to Checkpoint Immunotherapy in Melanoma. Cell *175*, 998–1013.e20.

83. Puram, S.V., Tirosh, I., Parikh, A.S., Patel, A.P., Yizhak, K., Gillespie, S., Rodman, C., Luo, C.L., Mroz, E.A., Emerick, K.S., et al. (2017). Single-Cell Transcriptomic Analysis of Primary and Metastatic Tumor Ecosystems in Head and Neck Cancer. Cell *171*, 1611–1624.e24.

84. Wang, B., Zhang, W., Jankovic, V., Golubov, J., Poon, P., Oswald, E.M., Gurer, C., Wei, J., Ramos, I., Wu, Q., et al. (2018). Combination cancer immunotherapy targeting PD-1 and GITR can rescue CD8^{+} T cell dysfunction and maintain memory phenotype. Sci. Immunol. *3*.

85. Durante, M.A., Rodriguez, D.A., Kurtenbach, S., Kuznetsov, J.N., Sanchez, M.I., Decatur, C.L., Snyder, H., Feun, L.G., Livingstone, A.S., and Harbour, J.W. (2020). Single-cell analysis reveals new evolutionary complexity in uveal melanoma. Nat Commun *11*, 496.

86. Li, H., van der Leun, A.M., Yofe, I., Lubling, Y., Gelbard-Solodkin, D., van Akkooi, C.J., van den Braber, M., Rozeman, E.A., Haanen, J.B.A.G., Blank, C.U., et al. (2019). Dysfunctional CD8 T Cells Form a Proliferative, Dynamically Regulated Compartment within Human Melanoma. Cell *176*, 775–789.e18.

87. Cillo, A.R., Kürten, C.H.L., Tabib, T., Qi, Z., Sayali, O., Wang, T., Liu, A., Duvvuri, U., Kim, S., Soose, R.J., et al. (2020). Immune Landscape of Viral- and Carcinogen-Driven Head and Neck Cancer. Immunity *52*, 183–199.e9.

88. Wang, L., Catalan, F., Shamardani, K., Babikir, H., and Diaz, A. (2020). Ensemble learning for classifying single-cell data and projection across reference atlases. Bioinformatics *36*, 3585–3587.

89. Ma, L., Hernandez, M.O., Zhao, Y., Mehta, M., Tran, B., Kelly, M., Rae, Z., Hernadez, J.M., Davis, J.L., Martin, S.P., et al. (2019). Tumor Cell Biodiversity Drives Microenvironmental Reprogramming in Liver Cancer. Cancer Cell *36*, 418–430.e6.

90. Shih, A.J., Menzin, A., Whyte, J., Lovecchio, J., Liew, A., Khalili, H., Bhuiya, T., Gregersen, P.K., and Lee, A.T. (2018). Identification of grade and origin specific cell populations in serous epithelial ovarian cancer by single cell RNA-seq. PLoS One *13*, e0206785.

91. Kim, N., Kim, H.K., Lee, K., Hong, Y., Cho, J.H., Choi, J.W., Lee, J., Suh, Y., Ku, B.M., Eum, H.H., et al. (2020). Single-cell RNA sequencing demonstrates the molecular and cellular reprogramming of metastatic lung adenocarcinoma. Nat Commun *11*, 2285.

92. Wu, T.D., Madireddi, S., de Almeida, P.E., Banchereau, R., Chen, Y.J., Chitre, A.S., Chiang, E.Y., Iftikhar, H., O'Gorman, W., Au-Yeung, A., et al. (2020). Peripheral T cell expansion predicts tumour infiltration and clinical response. Nature *579*, 274–278.

93. Hollern, D.P., Xu, N., Thennavan, A., Glodowski, C., Garcia-Recio, S., Mott, K.R., He, X., Garay, J.P., Carey-Ewend, K., Marron, D., et al. (2019). Cells and T Follicular Helper Cells Mediate Response to Checkpoint Inhibitors in High Mutation Burden Mouse Models of Breast Cancer. Cell *179*, 1191–1206.e21.

94. Moncada, R., Barkley, D., Wagner, F., Chiodin, M., Devlin, J.C., Baron, M., Hajdu, C.H., Simeone, D.M., and Yanai, I. (2020). Integrating microarray-based spatial transcriptomics and single-cell RNA-seq reveals tissue architecture in pancreatic ductal adenocarcinomas. Nat. Biotechnol. *38*, 333–342.

95. Neftel, C., Laffy, J., Filbin, M.G., Hara, T., Shore, M.E., Rahme, G.J., Richman, A.R., Silverbush, D., Shaw, M.L., Hebert, C.M., et al. (2019). An Integrative Model of Cellular States, Plasticity, and Genetics for Glioblastoma. Cell *178*, 835–849.e21.

96. Zhang, L., Li, Z., Skrzypczynska, K.M., Fang, Q., Zhang, W., O'Brien, S.A., He, Y., Wang, L., Zhang, Q., Kim, A., et al. (2020). Single-Cell Analyses Inform Mechanisms of Myeloid-Targeted Therapies in Colon Cancer. Cell *181*, 442–459.e29.

97. Jerby-Arnon, L., Shah, P., Cuoco, M.S., Rodman, C., Su, M., Melms, J.C., Leeson, R., Kanodia, A., Mei, S., Lin, J., et al. (2018). A Cancer Cell Program Promotes T Cell Exclusion and Resistance to Checkpoint Blockade. Cell *175*, 984–997.e24.

98. Guo, X., Zhang, Y., Zheng, L., Zheng, C., Song, J., Zhang, Q., Kang, B., Liu, Z., Jin, L., Xing, R., et al. (2018). Global characterization of T cells in non-small-cell lung cancer by single-cell sequencing. Nat. Med. *24*, 978–985.

99. Savas, P., Virassamy, B., Ye, C., Salim, A., Mintoff, C.P., Caramia, F., Salgado, R., Byrne, D.J., Teo, Z.L., Dushyanthen, S., et al. (2018). Single-cell profiling of breast cancer T cells reveals a tissue-resident memory subset associated with improved prognosis. Nat. Med. *24*, 986–993.

100. Yost, K.E., Satpathy, A.T., Wells, D.K., Qi, Y., Wang, C., Kageyama, R., McNamara, K.L., Granja, J.M., Sarin, K.Y., Brown, R.A., et al. (2019). Clonal replacement of tumor-specific T cells following PD-1 blockade. Nat. Med. *25*, 1251–1259.

101. Celus, W., Oliveira, A.I., Rivis, S., Van Acker, H.H., Landeloos, E., Serneels, J., Trusso Cafarello, S., Van Herck, Y., Mastrantonio, R., Köhler, A., et al. (2022). Plexin-A4 Mediates Cytotoxic T-cell Trafficking and Exclusion in Cancer. Cancer Immunol. Res. *10*, 126–141.

102. Degterev, A., Zhou, W., Maki, J.L., and Yuan, J. (2014). Assays for necroptosis and activity of RIP kinases. Methods Enzymol. *545*, 1–33.

103. Liao, Y., Wang, J., Jaehnig, E.J., Shi, Z., and Zhang, B. (2019). WebGestalt 2019: gene set analysis toolkit with revamped UIs and APIs. Nucleic Acids Res. *47*, W199–W205.

104. Baudino, L., Shinohara, Y., Nimmerjahn, F., Furukawa, J.i., Nakata, M., Martínez-Soria, E., Petry, F., Ravetch, J.V., Nishimura, S.i., and Izui, S. (2008). Crucial role of aspartic acid at position 265 in the CH2 domain for murine IgG2a and IgG2b Fc-associated effector functions. J. Immunol. *181*, 6664–6669.

105. Vivian, J., Rao, A.A., Nothaft, F.A., Ketchum, C., Armstrong, J., Novak, A., Pfeil, J., Narkizian, J., Deran, A.D., Musselman-Brown, A., et al. (2017). Toil enables reproducible, open source, big biomedical data analyses. Nat. Biotechnol. *35*, 314–316.

106. Goldman, M.J., Craft, B., Hastie, M., Repečka, K., McDade, F., Kamath, A., Banerjee, A., Luo, Y., Rogers, D., Brooks, A.N., et al. (2020). Visualizing and interpreting cancer genomics data via the Xena platform. Nat. Biotechnol. *38*, 675–678.

107. Finotello, F., Mayer, C., Plattner, C., Laschober, G., Rieder, D., Hackl, H., Krogsdam, A., Loncova, Z., Posch, W., Wilflingseder, D., et al. (2019). Correction to: Molecular and pharmacological modulators of the tumor immune contexture revealed by deconvolution of RNA-seq data. Genome Med. *11*, 50.

108. Li, T., Fu, J., Zeng, Z., Cohen, D., Li, J., Chen, Q., Li, B., and Liu, X.S. (2020). TIMER2.0 for analysis of tumor-infiltrating immune cells. Nucleic Acids Res. *48*, W509–W514.

109. Li, T., Fan, J., Wang, B., Traugh, N., Chen, Q., Liu, J.S., Li, B., and Liu, X.S. (2017). TIMER: A Web Server for Comprehensive Analysis of Tumor-Infiltrating Immune Cells. Cancer Res. *77*, e108–e110.

110. Zhao, J., Chen, A.X., Gartrell, R.D., Silverman, A.M., Aparicio, L., Chu, T., Bordbar, D., Shan, D., Samanamud, J., Mahajan, A., et al. (2019). Immune and genomic correlates of response to anti-PD-1 immunotherapy in glioblastoma. Nat. Med. *25*, 462–469.

111. Liu, D., Schilling, B., Liu, D., Sucker, A., Livingstone, E., Jerby-Arnon, L., Zimmer, L., Gutzmer, R., Satzger, I., Loquai, C., et al. (2019). Integrative molecular and clinical modeling of clinical outcomes to PD1 blockade in patients with metastatic melanoma. Nat. Med. *25*, 1916–1927.

112. Gide, T.N., Quek, C., Menzies, A.M., Tasker, A.T., Shang, P., Holst, J., Madore, J., Lim, S.Y., Velickovic, R., Wongchenko, M., et al. (2019). Distinct Immune Cell Populations Define Response to Anti-PD-1 Monotherapy and Anti-PD-1/Anti-CTLA-4 Combined Therapy. Cancer Cell *35*, 238–255.e6.

113. Kim, S.T., Cristescu, R., Bass, A.J., Kim, K.-M., Odegaard, J.I., Kim, K., Liu, X.Q., Sher, X., Jung, H., Lee, M., et al. (2018). Comprehensive molecular characterization of clinical responses to PD-1 inhibition in metastatic gastric cancer. Nat. Med. *24*, 1449–1458.

114. Miao, D., Margolis, C.A., Gao, W., Voss, M.H., Li, W., Martini, D.J., Norton, C., Bossé, D., Wankowicz, S.M., Cullen, D., et al. (2018). Genomic correlates of response to immune checkpoint therapies in clear cell renal cell carcinoma. Science *359*, 801–806.

115. Riaz, N., Havel, J.J., Makarov, V., Desrichard, A., Urba, W.J., Sims, J.S., Hodi, F.S., Martín-Algarra, S., Mandal, R., Sharfman, W.H., et al. (2017). Tumor and Microenvironment Evolution during Immunotherapy with Nivolumab. Cell *171*, 934–949.e16.

116. Hugo, W., Zaretsky, J.M., Sun, L., Song, C., Moreno, B.H., Hu-Lieskovan, S., Berent-Maoz, B., Pang, J., Chmielowski, B., Cherry, G., et al. (2016). Genomic and Transcriptomic Features of Response to Anti-PD-1 Therapy in Metastatic Melanoma. Cell *165*, 35–44.

117. Van Allen, E.M., Miao, D., Schilling, B., Shukla, S.A., Blank, C., Zimmer, L., Sucker, A., Hillen, U., Foppen, M.H.G., Goldinger, S.M., et al. (2015). Genomic correlates of response to CTLA-4 blockade in metastatic melanoma. Science *350*, 207–211.

118. Cloughesy, T.F., Mochizuki, A.Y., Orpilla, J.R., Hugo, W., Lee, A.H., Davidson, T.B., Wang, A.C., Ellingson, B.M., Rytlewski, J.A., Sanders, C.M., et al. (2019). Neoadjuvant anti-PD-1 immunotherapy promotes a survival benefit with intratumoral and systemic immune responses in recurrent glioblastoma. Nat. Med. *25*, 477–486.

119. Choueiri, T.K., Figueroa, D.J., Fay, A.P., Signoretti, S., Liu, Y., Gagnon, R., Deen, K., Carpenter, C., Benson, P., Ho, T.H., et al. (2015). Correlation of PD-L1 tumor expression and treatment outcomes in patients with renal cell carcinoma receiving sunitinib or pazopanib: results from COMPARZ, a randomized controlled trial. Clin. Cancer Res. *21*, 1071–1077.

120. Hoffman-Censits, J.H., Grivas, P., Van Der Heijden, M.S., Dreicer, R., Loriot, Y., Retz, M., Vogelzang, N.J., Perez-Gracia, J.L., Rezazadeh, A., Bracarda, S., et al. (2016). IMvigor 210, a phase II trial of atezolizumab (MPDL3280A) in platinum-treated locally advanced or metastatic urothelial carcinoma (mUC). J. Clin. Oncol. *34*, 355.

121. Atkins, M.B., McDermott, D.F., Powles, T., Motzer, R.J., Rini, B.I., Fong, L., Joseph, R.W., Pal, S.K., Sznol, M., Hainsworth, J.D., et al. (2017). IMmotion150: A phase II trial in untreated metastatic renal cell carcinoma (mRCC) patients (pts) of atezolizumab (atezo) and bevacizumab (bev) vs and following atezo or sunitinib (sun). J. Clin. Oncol. *35*, 4505.

122. Carvalho, B.S., and Irizarry, R.A. (2010). A framework for oligonucleotide microarray preprocessing. Bioinformatics *26*, 2363–2367.

123. Ritchie, M.E., Phipson, B., Wu, D., Hu, Y., Law, C.W., Shi, W., and Smyth, G.K. (2015). limma powers differential expression analyses for RNA-sequencing and microarray studies. Nucleic Acids Res. *43*, e47.

124. Duan, Z., and Luo, Y. (2021). Targeting macrophages in cancer immunotherapy. Signal Transduct. Targeted Ther. *6*, 127.

125. Liu, Y., and Wang, R. (2020). Immunotherapy Targeting Tumor-Associated Macrophages. Front. Med. *7*, 583708.

126. Sun, D., Wang, J., Han, Y., Dong, X., Ge, J., Zheng, R., Shi, X., Wang, B., Li, Z., Ren, P., et al. (2021). TISCH: a comprehensive web resource enabling interactive single-cell transcriptome visualization of tumor microenvironment. Nucleic Acids Res. *49*, D1420–D1430.

127. Fekete, J.T., and Győrffy, B. (2019). ROCplot.org: Validating predictive biomarkers of chemotherapy/hormonal therapy/anti-HER2 therapy using transcriptomic data of 3,104 breast cancer patients. Int. J. Cancer *145*, 3140–3151.

128. Kovács, S.A., and Győrffy, B. (2022). Transcriptomic datasets of cancer patients treated with immune-checkpoint inhibitors: a systematic review. J. Transl. Med. *20*, 249.

STAR★METHODS

KEY RESOURCES TABLE

REAGENT or RESOURCE	SOURCE	IDENTIFIER
Antibodies		
Alexa Fluor 488 anti-mouse CCR7 (clone:4B12)	Biolegend	Cat#120110 RRID:AB_492841
APC/Cyanine7 anti-mouse CD3 (clone:17A2)	Biolegend	Cat#100222 RRID:AB_2242784
BV750 anti-mouse CD3 (clone:17A2)	Biolegend	Cat#100249 RRID:AB_2734148
PE/Cyanine7 anti-mouse CD4 (clone: GK1.5)	Biolegend	Cat#100422 RRID:AB_312707
PE anti-mouse CD4 (clone: GK1.5)	Biolegend	Cat#100408 RRID:AB_312693
BUV563 anti-mouse CD4 (clone:GK1.5)	BD Biosciences	Cat#612923 RRID:AB_2870208
BV711 anti-mouse CD8a (clone: 53–6.7)	Biolegend	Cat#100759 RRID:AB_2563510
Pacific Blue anti-mouse CD8a (clone: 53–6.7)	Biolegend	Cat#100725 RRID:AB_493425
PE anti-mouse/human CD11b (clone:M1/70)	Biolegend	Cat#101208 RRID:AB_312791
APC anti-mouse/human CD11b (clone:M1/70)	Biolegend	Cat#101212 RRID:AB_312795
BUV661 anti-mouse CD11b (clone:ICRF44)	BD Biosciences	Cat#612977 RRID:AB_2870249
APC anti-mouse CD11c (clone: N418)	Biolegend	Cat#117310 RRID:AB_313779
Pacific Blue anti-mouse CD11c (clone: N418)	Biolegend	Cat#117322 RRID:AB_755988
FITC anti-mouse CD11c (clone: N418)	Biolegend	Cat#117305 RRID:AB_313774
Pacific blue anti-mouse CD31 (clone 390)	Biolegend	Cat#102421 RRID:AB_10613457
BV570 anti-mouse CD45 (clone:30-F11)	Biolegend	Cat#103136 RRID:AB_2562612
PE/Cyanine7 anti-mouse CD47 (clone: miap301)	Biolegend	Cat#127523 RRID:AB_2629544
BUV395 anti-mouse CD86 (clone:GL-1)	BD Biosciences	Cat#564199 RRID:AB_2738664
APC/Cyanine7 anti-mouse CD86 (clone:GL-1)	Biolegend	Cat#105030 RRID:AB_2244452
PerCP anti-mouse CD86 (clone: GL-1)	Biolegend	Cat#105026 RRID:AB_893417
PE/Cyanine7 anti-mouse CD90.2 (clone 30-H12)	Biolegend	Cat#105325 RRID:AB_2303142
PE/Cyanine7 anti-mouse CD172a (clone: P84)	Biolegend	Cat#144008 RRID:AB_2563546
PE anti-mouse CD200 (clone: OX-90)	Biolegend	Cat#123808 RRID:AB_2073942
APC anti-mouse CD206 (clone:C068C2)	Biolegend	Cat#141708 RRID:AB_10900231
BV785 anti-mouse CD206 (clone:C068C2)	Biolegend	Cat#141729 RRID:AB_2565823
PerCP/Cyanine5.5 anti-mouse CSF1R (clone: AFS98)	Biolegend	Cat#135525 RRID:AB_2566461
BV605 anti-mouse CSF1R (clone: AFS98)	Biolegend	Cat#135517 RRID:AB_2562760
PE anti-FASL (clone KAY-10)	Biolegend	Cat#106805 RRID:AB_2246643
FITC anti-mouse F4/80 (clone:QA17A29)	Biolegend	Cat#157310 RRID:AB_2876535
Pacific blue anti-mouse F4/80 (clone:BM8)	Biolegend	Cat#123124 RRID:AB_893475
BUV737 anti-mouse F4/80 (clone: T45-2342)	BD Biosciences	Cat#749283 RRID:AB_2873658
APC IFNy anti-mouse (clone: XMG1.2)	Biolegend	Cat#505810 RRID:AB_315404
PE anti-mouse IL2 (clone: JES6-5H4)	Biolegend	Cat#503808 RRID:AB_315302
FITC anti-mouse MHCII (clone: M5/114.15.2)	Biolegend	Cat#107606 RRID:AB_313321
BV650 anti-mouse MHCII (clone:M5/114.15.2)	Biolegend	Cat#107641 RRID:AB_2565975
BUV615 anti-mouse PD1 (clone: RPM1-30)	BD Biosciences	Cat#752354 RRID:AB_2875871
FITC anti-mouse PD1 (clone 29F.1A12)	Biolegend	Cat#135214 RRID:AB_10680238
PE anti-mouse PD1 (clone RMP1-30)	Biolegend	Cat#109103 RRID:AB_313420
APC anti-mouse PDL1 (clone 10F.9G2)	Biolegend	Cat#124312 RRID:AB_10612741
Percp/Cyanine5.5 anti-mouse PDL2 (clone: TY25)	Biolegend	Cat#107218 RRID:AB_2728126
Percp/Cyanine5.5 anti-mouse Siglec-H (clone:551)	Biolegend	Cat#129614 RRID:AB_10643995
FITC anti-mouse TNF (clone: MP6-XT22)	Biolegend	Cat#506304 RRID:AB_315425
PE anti-mouse pSTAT1 (clone: pY701)	BD Biosciences	Cat#562069 RRID:AB_11151907

(*Continued on next page*)

Continued

REAGENT or RESOURCE	SOURCE	IDENTIFIER
Pe/cyanine7 anti-mouse TRAIL (clone N2B2)	Biolegend	Cat#109311 RRID:AB_2721675
BV510 anti-mouse XCR1 (clone: ZET)	Biolegend	Cat#148218 RRID:AB_2565231
Alexa Fluor 488 anti-mouse FOXP3 (clone:MF-14)	Biolegend	Cat#126406 RRID:AB_1089113
PE/Cyanine7 anti-mouse GATA3 (clone: TWAJ)	Thermo Fischer Scientific	Cat#25-9966-42 RRID:AB_2573568
PE/Cyanine5 anti-mouse CD62L (clone: MEL-14)	Biolegend	Cat#104410 RRID:AB_313097
PE anti-mouse TCF1/7 (clone: S33-966)	BD Biosciences	Cat#564217 RRID:AB_2687845
Alexa Fluor 700 anti-mouse CD107a (clone:1D4B)	Biolegend	Cat#121628 RRID:AB_2783063
BV786 anti-mouse Tbet (clone: O4-46)	BD Biosciences	Cat#564141 RRID:AB_2738615
BV650 anti-mouse KI-67 (clone:11F6)	Biolegend	Cat#151215 RRID:AB_2876504
BV450 anti-mouse EOMES (clone: Dan11mag)	Thermo Fischer Scientific	Cat#48-4875-82 RRID:AB_2574062
BUV737 anti-mouse CD127 (clone: SB/199)	BD Biosciences	Cat#612841 RRID:AB_2870163
BUV395 anti-mouse TIM3 (clone:5D12/TIM-3)	BD Biosciences	Cat#747620 RRID:AB_2744186
anti-mouse calreticulin (clone: B44)	abcam	Cat#ab2907 RRID:AB_303402
Alexa Fluor 488 anti-rabbit IgG	abcam	Cat#ab150077 RRID:AB_2630356
APC/Cyanine7 anti-human CD3 (clone: OKT3)	Biolegend	Cat#317342 RRID:AB_2563410
Alexa Fluor 594 anti-human CD3 (clone: UCHT1)	Biolegend	Cat#300446 RRID:AB_2563236
PE/Cyanine7 anti-human CD4 (clone: okt/04)	Biolegend	Cat#317414 RRID:AB_571959
Alexa Fluor 597 anti-human CD8 (clone: RPA-T8)	Biolegend	Cat#301056 RRID:AB_2563232
PE/Dazzle anti-human CD8 (clone: Sk1)	Biolegend	Cat#344744 RRID:AB_2566515
VioGreen anti-human CD8 (clone:BW135/80)	Miltenyi Biotec	Cat#130-113-726 RRID:AB_2726267
BV570 anti-human CD45RO (clone: UCHL1)	Biolegend	Cat#304226 RRID:AB_2563818
Pacific blue anti-human IFNy (clone:4S. B3)	Biolegend	Cat#502532 RRID:AB_2561398
FITC anti-human CD45 (clone: REA747)	Miltenyi Biotec	Cat#130-110-769 RRID:AB_2658236
FITC anti-human CD163 (clone: REA812	Miltenyi Biotec	Cat#130-112-290 RRID:AB_2655475
Percp anti-human CD45 (clone:2D1)	Biolegend	Cat#368506 RRID:AB_2566358
APC anti-human CD14 (clone:63D3)	Biolegend	Cat#367118 RRID:AB_2566792
PE/Dazzle anti-human CSF1R (clone: AFS98)	Biolegend	Cat#135528 RRID:AB_2566523
PE anti-human PDL1 (clone:M1H1)	BD Biosciences	Cat#557924 RRID:AB_647198
Alexa Fluor 488 isotype control (clone: MOPC-21)	BD Biosciences	Cat#557702 RRID:AB_396811
Alexa Fluor 647 isotype control (clone: MOPC-21)	BD Biosciences	Cat#557783 RRID:AB_396871
PE isotype control (clone:27–35)	BD Biosciences	Cat#555058 RRID:AB_395678
PE/Cyanine5 isotype control (clone: P3.6.2.8.1)	Thermo Fischer Scientific	Cat#46-4714-82 AB_1834453
FcX (truStain/CD16/32) anti-mouse (clone: 93)	Biolegend	Cat#101320 RRID:AB_1574975
anti-mouse MLKL (clone:3H1)	Sigma Aldrich	Cat#MABC604 RRID:AB_2820284
anti-mouse pMLKL (clone: EPR9515(2))	Abcam	Cat#ab196436 RRID:AB_2687465
anti-mouse RIPK1 (clone: D94C12)	Cell signaling	Cat#3493T RRID:AB_2305314
anti-mouse RIPK3	Biorad	Cat#AHP1797 RRID:AB_2178676
anti-mouse HMGB1 (clone: EPR3507	Abcam	Cat#ab79823 RRID:AB_1603373
anti-mouse PD-L1 (clone 10F.2H11)	BioxCell	Cat#BE0361 RRID:AB_2927503
anti-mouse PD-L1 (clone D4H1Z)	Cell signaling	Cat#60475 RRID:AB_2924680
anti-mouse PD-L2 (clone 168633)	R&D systems	Cat#MAB1022 RRID:AB_2268067
anti-HPV-E7 (clone: 8C9)	Thermo Fischer Scientific	Cat# 28-0006 RRID:AB_2533057
anti-human/mouse/rat caspase8	Thermo Fischer Scientific	Cat#PA5-77888 RRID:AB_2735575
anti-human CD163 (clone OTI2G12)	Abcam	Cat#ab156769
AF647 anti-human CD8 (clone EP1150y)	Abcam	Cat#ab196193 RRID:AB_869025
anti-mouse IgG	abcam	Cat#ab150113 RRID:AB_2576208
anti-Bovine/human/mouse/sheep/rat caspase9	Thermo Fischer Scientific	Cat#PA5-16358 RRID:AB_10985523
anti-mouse PARP (clone:46D11)	Cell signaling	Cat# 9532S RRID:AB_659884

(*Continued on next page*)

Continued

REAGENT or RESOURCE	SOURCE	IDENTIFIER
anti-mouse Actin (clone: AC-74)	Sigma Aldrich	Cat#A5316 RRID:AB_476743
anti-mouse Actin	Abcam	Cat#ab49900 RRID:AB_867494
anti-mouse Actin (clone: AC-15)	Sigma Aldrich	Cat#A5441 RRID:AB_476744
anti-rabbit IgG	Cell signaling	Cat#7074S RRID:AB_2099233
anti-mouse IgG	Cell signaling	Cat#7076S RRID:AB_330924
anti-rat IgG2a	Biolegend	Cat#400502 RRID:AB_326523
anti-mouse TNF	Invitrogen	Cat#16-7423-81 RRID:AB_469261
anti-mouse TRAIL	R&D systems	Cat#AF721 RRID:AB_2205069
anti-mouse PDL1 D265A mutated	invivogen	Cat#pdl1-mab15
anti-mouse CSF1R (clone: AFS98)	BioXCell	Cat#BP0213 RRID:AB_2687699
Chemicals, peptides, and recombinant proteins		
Recombinant Murine TNF	Miltenyi Biotec	Cat#130-101-687
Recombinant Murine IFNβ	R&D systems	Cat#8234-MB-010
Recombinant Murine IL4	Peprotech	Cat#214-14
Recombinant Murine M-CSF	Peprotech	Cat#315-02
Recombinant Murine GM-CSF	Peprotech	Cat#315-03
Recombinant Murine IL2	Peprotech	Cat#210-12
Recombinant Murine IFNγ	Peprotech	Cat#315-05
Recombinant Murine PGE2	Merk life science	Cat#P5640
Recombinant Murine IL6	Peprotech	Cat#216-16
Recombinant Murine ILIβ	Peprotech	Cat#211-11B
lipopolysaccharide Escherichia coli	Invivogen	Cat#tlrl-eblps
imiquimod	Invivogen	Cat#tlrl-imqs
5′ppp-dsRNA/lyovec	Invivogen	Cat#tlrl-3prnaclv
2′3′ cGAMP	Invivogen	Cat#tlrl-nacga23
Cisplatin	Sigma	Cat#P4394
Doxorubicin	Merck	Cat#D1515
NP-40 cell lysis buffer	Thermo Fischer Scientific	Cat#FNN0021
Phenylmethylsulfonyl fluoride (PMSF)	Thermo Fischer Scientific	Cat#1083709
Pierce ™ Protease Inhibitor Mini Tablets	Thermo Fischer Scientific	Cat#A32953
Pierce ™ Phosphatase Inhibitor Mini Tablets	Thermo Fischer Scientific	Cat#A32957
Pierce ™ ECL Western Blotting Substrate	Thermo Fischer Scientific	Cat#32106
Bovine serum albumin (BSA)	Sigma	Cat#A2153-50G
Criterion™ XT Bis-Tris Precast Gels	Biorad	Cat#3450124
Cell Staining Buffer	Biolegend	Cat#420201
Western Blot Stripping Buffer	abcam	Cat#ab270550
BV-6	Selleckchem	Cat#S7597
Z-Val-Ala-Asp (OMe)-FMK	Bachem	Cat#4027403
Necrostatin-1s	Bioke	Cat#17802S
pHrodo™ iFL Red STP Ester	Thermo Fischer Scientific	Cat#P36011
recombinant HPV-E6 antigen (VYDFAFRDL)	LifeTein	N/A
recombinant HPV-E6 antigen (DKKQRFHNI)	LifeTein	N/A
recombinant HPV-E7 antigen (RAHYNIVTF)	LifeTein	N/A
recombinant HPV-E7 antigen (LCVQSTHVD)	LifeTein	N/A
Cytofix/cytoperm™ fixation/permeabilization solution kit	BD Biosciences	Cat#554714
True-nuclear™ transcription factor buffer set	Biolegend	Cat#424401
Dynabeads® Mouse T-activator CD3/CD28	Thermo Fischer Scientific	Cat#11456D
Brefeldin A Solution (1000x)	Thermo Fischer Scientific	Cat#00-4506-51

(*Continued on next page*)

Continued

REAGENT or RESOURCE	SOURCE	IDENTIFIER
Cytofix	BD Biosciences	Cat#554655
SYBRgreen	Highqu	Cat#QPD0150
Bromodeoxyuridine	BD Biosciences	Cat#550891
MACS tissue storage solution	Miltenyi Biotec	Cat#130-100-008
phorbol myristate acetate	Sigma-Aldrich	Cat#P8139
Ionomycin	Sigma-Aldrich	Cat#I9657
Brefeldin A	Biolegend	Cat#420601
Clodronate liposomes	Liposoma	N/A
CellTracker CM-DiI dye	Thermo Fischer Scientific	Cat#C7000
anti-mouse PDL1 (clone: MIH5)	JJP Biologics, Warsaw, Poland. Louis Boon	N/A
anti-mouse CTLA4 (clone:4F10)	JJP Biologics, Warsaw, Poland. Louis Boon	N/A
anti-mouse PD1 (clone: RMP1-14	JJP Biologics, Warsaw, Poland. Louis Boon	N/A
anti-mouse IFNy (clone: XMG 1.2)	JJP Biologics, Warsaw, Poland. Louis Boon	N/A
anti-mouse NK1.1 (clone:PK136)	JJP Biologics, Warsaw, Poland. Louis Boon	N/A
anti-mouse CD8 (clone: YTS169)	JJP Biologics, Warsaw, Poland. Louis Boon	N/A
Fixable Viability Dye eFluor™ 780	Thermo Fischer Scientific	Cat#65-0865-14
Zombie Aqua™ Fixable Viability Kit A	Biolegend	Cat#423102
ZOMBI NIR™ fixable viability kit	Biolegend	Cat#423106
Edit-R Lentiviral CAG-Blast-Cas9 Nuclease Particles	Dharmacon Horizon discovery	Cat#VCAS10129
Edit-R CRISPR-Cas9 Synthetic tracrRNA	Dharmacon Horizon discovery	Cat#U-002005-50
LY294002	Tebu-bio	Cat#1543664
PD98059	Tebu-bio	Cat#T2623
SC75741	Tebu-bio	Cat#T6661
S-ruxolitinib	Tebu-bio	Cat#T6156
Critical commercial assays		
Caspase-Glo kit	Promega	Cat#G8091
RealTime-Glo Annexin V Apoptosis and Necrosis assay	Promega	Cat#JA1011
MTS assay kit	abcam	Cat#ab197010
ELITEN ATP assay system kit	Promega	Cat#FF2000
Bicinchoninic Acid (BCA) Pierce Protein Assay Kit	Thermo Fischer Scientific	Cat#23227
Purelink RNA Mini Kit	Thermo Fischer Scientific	Cat#12183025
QuantiTect Reverse Transcription kit	Qiagen	Cat#205313
Proteome Profiler Mouse Cytokines Array Kit Panel A	R&D systems	Cat#ARY006
pan-T cell isolation kit II	Miltenyi Biotec	Cat#130-095-130
Murine tumor dissociation kit	Miltenyi Biotec	Cat#130-096-730
anti-F4/80 microbeads	Miltenyi Biotec	Cat#130-110-443
Human tumor dissociation kit	Miltenyi Biotec	Cat#130-095-929
anti-human CD45 microbeads	Miltenyi Biotec	Cat#130-045-801
anti-mouse CD45 microbeads	Miltenyi Biotec	Cat#130-110-618
CXCL10 ELISA	R&D systems	Cat#DY466
IFN alfa ELISA	Invivogen	Cat#luex-mifna
PDL1 ELISA	R&D systems	Cat#DY1019

(*Continued on next page*)

Continued

REAGENT or RESOURCE	SOURCE	IDENTIFIER
IFN beta ELISA	Invivogen	Cat#mifnbv2
APC conjugation kit	abcam	Cat#ab201807
Other		
Rational selection of syngeneic preclinical tumor models for immunotherapeutic drug discovery	Mosely et al.[27]	GEO: GSE85509
Analysis of DC vaccines used for phase II clinical trial in prostate carcinoma patients	Castiello et al.[23]	GEO: GSE85698
High Dimensional Analysis Delineates Myeloid and Lymphoid Compartment Remodeling during Successful Immune Checkpoint Cancer Therapy	Gubin et al.[80]	GEO: GSE119352
Checkpoint blockade immunotherapy induces dynamic changes in PD-1-CD8$^+$ tumor-infiltrating T cells	Kurtulus et al.[81]	GEO: GSE122969
Defining T cell states associated with response to checkpoint immunotherapy in melanoma	Sade-Feldman et al.[82]	GEO: GSE120575
Single cell RNA-seq analysis of head and neck cancer	Puram et al.[83]	GEO: GSE103322
Combination immunotherapy can rescue CD8$^+$ T cell dysfunction and maintain memory phenotype in cancer	Wang et al.[84]	GEO: GSE120909
Single-cell analysis reveals new evolutionary complexity in uveal melanoma	Durante et al.[85]	GEO: GSE139829
Dysfunctional CD8$^+$ T cells form a proliferative, dynamically regulated compartment within human melanoma [scRNA-seq]	Li et al.[86]	GEO: GSE123139
Immune landscape of viral- and carcinogen-derived head and neck cancer	Cillo et al.[87]	GEO: GSE139324
Ensemble learning for classifying single-cell data and projection across reference atlases	Wang et al.[88]	GEO: GSE141982
Tumor cell biodiversity drives microenvironmental reprogramming in liver cancer	Ma et al.[89]	GEO: GSE125449
Identification of grade and origin specific cell populations in serous epithelial ovarian cancer by single cell RNA-seq	Shih et al.[90]	GEO: GSE118828
Single cell RNA sequencing of lung adenocarcinoma	Kim et al.[91]	GEO: GSE131907
Peripheral clonal expansion of T lymphocytes associates with tumor infiltration and response to cancer immunotherapy	Wu et al.[92]	GEO: GSE139555
Mutagenesis sensitizes murine models of triple negative breast cancer to immunotherapy	Hollern et al.[93]	GEO: GSE136206
Integrating microarray-based spatial transcriptomics and single-cell RNA-seq reveals tissue architecture in pancreatic ductal adenocarcinomas	Moncada et al.[94]	GEO: GSE111672
single cell RNA-seq analysis of adult and pediatric IDH-wildtype Glioblastomas	Neftel et al.[95]	GEO: GSE131928
Single-Cell Analyses Inform Mechanisms of Myeloid-Targeted therapies in colon cancer	Zhang et al.[96]	GEO: GSE146771
Single-cell RNA-seq of melanoma ecosystems reveals sources of T cells exclusion linked to immunotherapy clinical outcomes	Jerby-Arnon et al.[97]	GEO: GSE115978
T cell landscape of non-small cell lung cancer revealed by deep single-cell RNA sequencing	Guo et al.[98]	GEO: GSE99254
Single-cell RNA-seq of six thousand purified CD3$^+$ T cells from human primary TNBCs	Savas et al.[99]	GEO: GSE110686

(*Continued on next page*)

Continued

REAGENT or RESOURCE	SOURCE	IDENTIFIER
Clonal replacement of tumor-specific T cells following PD-1 blockade [single cells]	Yost et al.[100]	GEO: GSE123813
Experimental models: Cell lines		
TC1	Yang et al.[34]	N/A
TC1 *Mlkl* −/−	Yang et al.[34]	N/A
TC1 Ripk3 −/−	Yang et al.[34]	N/A
TC1 *Caspase8* −/−	This paper	N/A
TC1 *Caspase9* −/−	This paper	N/A
TC1 *Caspase8/9* −/−	This paper	N/A
LLC	Celus et al.[101]	N/A
J774-Dual™	N/A	Cat#j774d-nfis
MC38	Kerafast	Cat#ENH204-FP
Experimental models: Organisms/strains		
Mouse:C57BL/6J	the Jackson Laboratory	JAX: 000664
Mouse: B6.129S2-*Ifnar1*^{tm1Agt}/Mmjax	the Jackson Laboratory	JAX:010830
Mouse: B6.129P2*(C)*-*Ccr7*^{tm1Rfor}/*J*	the Jackson Laboratory	JAX:006621
Oligonucleotides		
murine CXCL10_forward	IDT	CGATGACGGGCCAGTGAGAA
murine CXCL10_reverse	IDT	CAGCCACTTGAGCGAGGACT
murine CXCL9_forward	IDT	AAACAGTTTGCCCCAAGCCC
murine CXCL9_reverse	IDT	CGAGTCCGGATCTAGGCAGG
murine RSAD2_forward	IDT	CGACAGCTTCGATGAGCAGG
murine RSAD2_reverse	IDT	ACACCTCTTTGTGACGCTCCA
murine MX1_forward	IDT	GGGGTCTTGACCAAGCCTGA
murine MX1_reverse	IDT	ACCGGCTGTCTCCCTCTGATA
murine IRF_forward	IDT	TGCTGAGCGAAGAGAGCGAA
murine IRF_reverse	IDT	CCTGCCATGCTGCATAGGGT
murine ACTIN_forward	IDT	CATTGCTGACAGGATGCAGAAGG
murine ACTIN_reverse	IDT	TGCTGGAAGGTGGACAGTGAGG
Recombinant DNA		
crRNA Caspase 8	Dharmacon™, Horizon Discovery	CCAGATTTCTCCCTACAGGT
crRNA Caspase 9	Dharmacon™, Horizon Discovery	CTGTCCCATAGACAGCACCC
Software and algorithms		
GraphPad Prism 8	GraphPad Software	https://www.graphpad.com/
FlowJo	BD Biosciences	https://flowjo.com
Image Lab 6.1	Biorad, Image Lab	https://www.bio-rad.com/en-be/product/image-lab-software?ID=KRE6P5E8Z#fragment-6
Biorender	Biorender	https://biorender.com/
Phyton (version 3.9.7)	Phyton	https://www.python.org/
Gistic	Broad institute	https://portals.broadinstitute.org/tcga/gistic/browseGisticByGene
Morpheus	Broad institute	https://software.broadinstitute.org/morpheus/
Stream	Human Cell atlas data portal	https://data.humancellatlas.org/analyze/methods/stream
qupath	qupath	https://qupath.github.io/
msigdb_v7.2_GMTs	Broad institute	https://www.gsea-msigdb.org/

(*Continued on next page*)

Continued

REAGENT or RESOURCE	SOURCE	IDENTIFIER
Scanpy 1.9.3.	Scanpy	https://genomebiology.biomedcentral.com/articles/10.1186/s13059-017-1382-0
UMAP-learn 0.5.3	PyPI	https://arxiv.org/abs/1802.03426
Matplotlib 3.7.1	matplotlib	https://matplotlib.org/

RESOURCE AVAILABILITY

Lead contact

Further information and requests for resources and reagents should be directed to and will be fulfilled by the lead contact, Abhishek Garg (abhishek.garg@kuleuven.be)

Materials availability

This study did not generate new unique reagents. Beyond that, all major resources or materials used are described in the "Key Resources" table above.

Data and code availability

- No original code was generated for this study.
- This paper has analyzed existing, publicly available data. These accession numbers or relevant publications/database sources for the datasets are listed in the key resources table.
- Any additional information required to reanalyze the data reported in this paper is available from the lead contact upon request.

EXPERIMENTAL MODEL AND STUDY PARTICIPANT DETAILS

Human subjects and ethics

Human samples were derived from glioblastoma patients included in the GlioVax trial (NCT03395587) with the informed consent of the patients and approval by the ethical committee of University Hospital Düsseldorf (MC-LKP-921 and 3005). Further trial details have been described elsewhere.[38]

Mice models

Wild type C57BL/6j were obtained from the KU Leuven breeding facility. The *Ifnar1*$^{-/-}$ mice (B6.129S2-*Ifnar1*^{tm1Agt}/Mmjax)(The Jackson Laboratory #010830) were a kind gift from the lab of Roos Vandenbroucke (VIB-UGent) and the *Ccr7*$^{-/-}$ mice (*B6.129P2(C)-Ccr7*^{tm1Rfor}*/J)* (The Jackson Laboratory #006621) were a kind gift from the lab of Bart Lambrecht (VIB-UGent). All subcutaneous tumor experiments were done using 7- to 12-week-old female/male mice, maintained in the conventional mouse facility. Experiments were approved by the animal ethics committee at KU Leuven (project P114/2019 and p195/2020) following the European directive 2010/63/EU as amended by the Regulation (EU) 2019/1010 and the Flemish government decree of 17 February 2017.

Cell lines

TC1 wild type, Ripk3$^{-/-}$, Mlkl$^{-/-}$ were a kind gift from the lab of Oliver Kepp (Université Paris).[34] LLC and MC38 cancer cells were a kind gift from the laboratory of Massimiliano Mazzone (VIB-KULeuven). J774-Dual cells were purchased from Invivogen. Cells were cultured at 37°C under 5% CO_2 in DMEM media containing 2 mM L-glutamine, 3.7 g/L sodium bicarbonate, 4.5 g/L glucose and 1.0 mM sodium pyruvate) with 10% heat-inactivated fetal bovine serum (30 min at 56°C; FBS), penicillin 100 U/ml streptomycin 100 μg/mL DMEM and split when 90% confluency was reached through enzymatic dissociation (Trypsin).

Cell line creation

3 mL of the LentiGuide Cas9 lentiviral particles were added into the well, to reach an MOI of 0.3 TU/cell, and the plate was gently shaken before being placed back into the incubator. Thereafter, 48 h later, the supernatant was replaced with 2 mL fresh medium and lentiviral transduced cells were now ready for transfection of synthetic guide RNA. The synthetic guide RNA complex was prepared by adding equal quantity of crRNA targeting *Casp8* + crRNA targeting *Casp9* + tracrRNA, all at final concentrations of 25 nM, in 100 μL serum-free DMEM and these were incubated for 5 min at room temperature. Transfection reagents were prepared in a separate tube by diluting 10 μL of DharmaFECT 1 in 100 μL of serum-free DMEM and incubated for 5 min. The crRNA:tracrRNA complex and DharmaFECT 1 working solution were mixed and incubated for another 20 min adding to lentiviral-transduced cells, which were incubated for another 48 h to reach efficient gene knockout. The transfected cells were then sorted to single cell clones into 96-well plates by a FACSAria cell sorter (BD Bioscience). Two weeks later, visible clones were picked and duplicated for seed reservation as well as western blotting detection of Casp8 (Thermofischer #PA5-77888) and Casp9(Thermofischer #PA5-16358) expression to confirm the knock-out phenotype.

METHOD DETAILS

Cell death analysis

Cell death induction

For cell death induction cells were seeded in the appropriate dish as such that they reached an 80% confluency the next day. Necroptosis was induced in TC1 WT by 100 ng/mL tumor necrosis factor (TNF) (Miltenyi #130-101-687), 1μM BV6 (Selleckchem #S7597 and 20μM Z-Val-Ala-Asp (OMe)-FMK (zVaD) (Bachem #4027403). For apoptosis, TC1 Mlkl$^{-/-}$, MC38 or LLC cells were pre-treated with 10μM BV6 for 3h and subsequently 100 ng/mL TNF was added. When applicable, a pre-treatment of 30μM of Necrostatin-1s (Bioke #17802S) for 3h was used to inhibit necroptosis.

MTT assay

TC1 WT and Mlkl$^{-/-}$ cells were seeded in a 96 well plate at a density of 5 000 cells per well 24h before cell death induction. Cell survival was obtained using the thiazolyl blue tetrazolium bromide (MTT) reagent (Abcam #ab197010). Absorbance was read on a microplate reader (Flexstation) at 490 nm at 24h and 48h after cell death induction.

RealTime-Glo Annexin V Apoptosis and Necrosis Assay

A total of 5 000 cells TC1 WT and Mlkl$^{-/-}$ cells were plated in 96-well plates in 100 μL DMEM and incubated for 24h. Necroptotic and apoptotic stimuli cocktails were added to the plates. Apoptosis and necroptosis were detected using the RealTime-Glo Annexin V Apoptosis and Necrosis Assay (Promega #JA1011) including CellTox green (Promega #G8741). Bioluminescence and fluorescence at excitation 485nm and emission 530nm were measured at different time points; 1, 3, 6, 9, 20, 24, 27, 30 and 48 h on a microplate reader (Flexstation). Fold changes to untreated (control) were taken. Percentage of cell death at 48h was estimated using following formula: Dead (%) = ((RFU TNF well/total RFU TNF well) − (RFU control well/total RFU control well)) × 100% as previously described.[102]

Caspase 3/7 activity

Cells were seeded in a 96-well plate at a density of 3000 cells/well. Cell death was induced, and the Caspase 3/7 activity was measured at 24h and 48h using the caspase-glo kit (Promega #G8091). A fold change to untreated cells was taken to obtain caspase 3/7 activity.

Western Blot

For intracellular proteins, 800 000 cells were seeded in 10cm dishes 24h before cell death induction. Cells were scraped and collected at 1, 3, 6, 24 or 48 h after cell death induction. Cells were centrifuged at 1500rpm for 5 min and the pellet was resuspended in 100μL NP-40 lysis buffer (Thermo Fischer #FNN0021) with protease (Thermo Fischer #A32953) and phosphatase inhibitors (Thermo Fischer #A32957). For secreted proteins, cells were 2 500 000 cells seeded in a 15cm dishes and media was collected 24h after cell death induction. Floating cells were removed by centrifugation. The supernatant was concentrated using Amicon Ultra-15 centrifuge filter units (Merck #UFC901024). A Bicinchoninic acid assay (BCA) for colorimetric quantification of total protein was done with a BCA protein assay kit (Thermo Fischer Scientific #23227) and a protein mixture of 90 μg was loaded onto the gel. Following proteins were detected; MLKL (clone 3H1), phosphorylated MLKL (pMLKL) (clone EPR9515(2)), RIPK1 (clone D94C12), RIPK3 (polyclonal), HMGB1(clone EPR3507), HPV-E7 (clone 8C9), PARP (clone 46D11), PD-L1 (clone D4H1Z), PD-L2 (clone 168633), and β-Actin (clone AC-74 and AC-15). The primary antibodies were diluted in 5% BSA+TBST with a dilution factor of 1/1000. As secondary antibody, we used the anti-rabbit antibody labelled with HRP (Cell Signaling #7074S) or anti-mouse antibody labelled with HRP (Cell Signaling #7076S) diluted in 5% BSA+TBST with a dilution factor of 1/2000. The antibody's tethering to the proteins on the membranes were detected using the ECL substrate and the resulting precipitate was detected with the ChemiDoc MP imaging system. For detection of MLKL and HPV-E7, the membranes were stripped for 15 min at room temperature using stripping buffer (Abcam #Ab270550) with a dilution factor of 1/2000 and same procedure as described above was used to detect the protein of interest. The precision plus protein dual color standards (Biorad #161037) was used as a ladder.

ATP secretion

Media of TC1 WT and Mlkl$^{-/-}$ cells after cell death induction was harvested at 6, 24 and 48h. The presence of ATP in the media was analyzed using the ATP assay system (Promega #FF2000). A fold change to untreated cells was taken to obtain ATP release.

Flow cytometry-based detection of calreticulin and CD47

A total of 200 000 TC1 WT and Mlkl$^{-/-}$ cells were plated in 12-well plates in 1 mL of DMEM and incubated for 24h. Cell death was induced for 48h. Then the cells were collected, washed with PBS, and transferred to 5mL flow cytometry tubes. The cells were re-suspended in 50 μL of FACS buffer (0.5% BSA and PBS solution) and 1/100 anti-calreticulin primary antibody (clone B44). After 30 min incubation in the dark on ice, cells were washed with 1mL of FACS buffer, centrifuged and the supernatant was discarded. Then, cells were again re-suspended in 50 μL of FACS buffer with 1/500 of Goat Anti-Rabbit Alexa Fluor 488 (polyclonal) for CRT, anti-CD47 (clone miap301) antibody and Fixable Viability Dye eFluor 780. After 30 min incubation on ice in the dark, cells were fixed with cytofix (BD Bioscience #554655).

J774 reporter assay

J774-Dual cells (Invivogen) were treated with 1000 pg/mL LPS-EB (Invivogen# tlrl-eblps) and/or 10 ng/ml anti-PDL1(Polpharma Biologics; clone M1H5) for 48 h. NF-κB activity was checked in media by adding 100 μL of Quanti-Blue (Invivogen) to 100 μL of (separately recovered) J774 media. Absorbance was examined at an optical density of 655 nm, 4 to 8 h after Quanti-Blue addition by microplate reader (Biotek).

In vitro assays

DC vaccine formation

For DC vaccine creation, bone marrow derived DCs were stimulated with dying cancer cells in a 1:1 ratio or with TC1 antigens (i.e., Human Papillomavirus (HPV) e6/e7 epitopes: VYDFAFRDL/DKKQRFHNI, RAHYNIVTF/LCVQSTHVD)), with or without 2.5 ng/mL interferon beta (IFNβ) (R&D systems #8234-MB-010) for 48h. Where indicated, DCs were stimulated with 1000 pg/ml lipopolysaccharide Escherichia coli (LPS-EB) (Invivogen #tlrl-eblps) as a positive control. In the relevant conditions, DCs were treated with 1000 pg/mL LPS-EB and 5 ng/mL IFNγ, 1000 pg/mL LPS-EB alone or with 4 ng/mL IL1β, 1 μg/mL PGE_2, 2 ng/mL IL6 and 25 ng/ml TNF instead of IFNβ. After 48h, DCs were harvested by scraping and washed with PBS for injection; 1000 000 DCs per 100μL PBS or for further analysis. Media of the DC cultures was also collected for further analysis, ELISA, cytokine array.

Flow cytometry

Before staining procedure, FC receptor of all samples was blocked using TruStain FcX (Biolegend #101320) for 15min. Cells were further stained with the indicated antibodies listed in Key resource table, diluted in 0.5% BSA, for 1h and fixed with cytofix (BD Bioscience #554655). In the case of intracellular markers, cells were fixed and permeabilized with the Cytofix/Cytoperm Kit (BD Bioscience #554714). For the staining of transcription factors, the true-nuclear transcription factor buffer (Biolegend #42441) set was used. After fixation, cells were maintained in 0.5% BSA. For intracellular cytokine staining, the cells were stimulated with Dynabeads Mouse T activator CD3/CD28 (Thermo Fisher Scientific #11456D). After 1h at 37°C 5% CO_2, 2μL Brefeldin A (Thermo Fisher Scientific #00-4506-51) was added. Cells were then placed at 37°C 5% CO_2 for 4h, transferred to 4°C overnight and then stained for intracellular cytokines. Flow cytometry was performed on the Attune NxT (Thermo Fisher Scientific), FACSCanto (BD Bioscience) or the ID7000 (SONY). Cell doublets were excluded based on FSC-A/FSC-H. Flow cytometry data was analyzed using FlowJo.

DC vaccine - TAM cocultures

DC vaccines were harvested as previously described. DC vaccines were cocultures with TC1-tumor derived TAMs in a 1:1 ratio. After 48h cocultures were scraped to collect the cells, centrifuged, and washed with PBS. Single cell suspension was stained with fluorescently labelled antibodies diluted in FACS buffer (0.5% BSA and PBS solution) for 1h on ice and then washed with the same buffer. Cells were fixed with cytofix (BD Bioscience #554655). Following fluorochrome-conjugated antibody clones were used to analyze the isolated lymph nodes by flow cytometry; MHCII (clone M5/114.15.2), PDL1 (clone 10F.9G2), CD86 (clone GL1), F4/80 (clone T45-2342), CSF1R (clone AFS98), CD11b (clone ICRF44) and CD206 (clone C068C2).

T cell - TAM cocultures

TC1 derived TAMs and matched T cells (derived from the spleen) were harvested as described above. TAMs were plated in media alone or with 10 μg/ml anti-PDL1(Polpharma Biologics), 10 μg/ml anti-PD1(Polpharma Biologics), 10 μg/ml anti-TNF (Invitrogen #16-7423-81) or 10 μg/ml anti-Trail (R&D systems #AF721), for 24h. TAMs were scraped and washed and cocultured with their matched T cells in a 1:1 ratio with 100 IU/mL IL-2 for 48h. Then cocultures were scraped to collect the cells, centrifuged, and washed with PBS. Single cell suspension was stained with fluorescently labelled antibodies diluted in FACS buffer (0.5% BSA and PBS solution) for 1h on ice and then washed with the same buffer. Cells were fixed with cytofix (BD Bioscience #554655). The following fluorochrome-conjugated antibody clones were used: CD3 (clone 17A2), CD4 (clone GK1.5) and CD8a (clone 53–6.7).

TAM *viability*

TC1 derived TAMs and matched T cells (derived from the spleen) were harvested as described above. TAMs were plated at a density of 30.000 cells/well in a 96 well plate and incubated with 10 μg/ml anti-PDL1(Polpharma Biologics), 5μM LY294002 (Tebu-bio #1543664), 5μM PD98059 (Tebu-bio #T2623), 5μM SC75741 (Tebu-bio #T6661) or 5μM S-ruxolitinib (Tebu-bio #T6156). After 48h, cell viability was measured by performing an MTT.

Enzyme-linked immunoassay (ELISA)

Derived media of DC vaccines as described above was used to perform a CXCL10 ELISA (R&D systems#DY466. For IFNα and β secretion, TC1 cells were treated with 1 μg/ml LPS (Invivogen# tlrl-eblps), 100 μg/ml imiquimod (Invivogen #tlrl-imqs), 10 μg/ml 5′ppp-dsRNA/lyovec (Invivogen #tlrl-3prnaclv), 2′3′ cGAMP (Invivogen #tlrl-nacga23) 25μM doxorubicin (Merck #D1515) or 100μM cisplatin (Merck #PHR1624) for 24h. An ELISA for PDL1 (R&D systems #DY1019), IFN alfa (Invivogen #luex-mifnav2) and beta (Invivogen #luex-mifnbv2) was performed according to manufacturer's protocol.

Quantitative polymerase chain reaction (qPCR)

The RNA of DC vaccines was extracted using the Purelink RNA Mini Kit (ThermoFischer #12183025). Using the QuantiTect Reverse Transcription kit (Qiagen #205313) cDNA was synthesized from RNA. The qPCR was performed on the StepOnePlus Real-Time PCR system (Applied Biosystems) using SYBRgreen (Highqu #QPD0150) with the following primers: *Irf7, Rsad, Mx1, Cxcl9, Cxcl10* and *Actin* (all primers were ordered at Integrated DNA Technologies, sequences available in material 1). Fold change was determined using the $2^{-}\Delta\Delta CT$ method compared to the house keeping gene, *Actin,* and untreated DCs.

Antibody array

Derived media of DC vaccines as described above was used for a mouse cytokine array panel A (R&D systems #ARY006) was used. Cytokine array was performed according to the manufacturer's protocol. Arrays were read on the ChemiDoc (Biorad). Dot intensities were determined using Image Lab (Biorad). From all values, the background was subtracted. Normalization was done using DCs stimulated with live cancer cells. Fold-change values derived from above antibody array for different immunological factors, cytokines or chemokines per treatment condition were used to run a GSEA analysis using WebGestalt (WEB-based Gene SeT

AnaLysis Toolkit), which is a functional enrichment analysis web tool.[103] This GSEA analysis was run with Mus musculus as reference organism for Gene Ontology Biological Process term enrichment with the following analyses parameters: minimum number of genes for a category, 3; maximum number of genes for a category, 2000; significance level, top 10; number of permutations, 1000; p, 1; collapse method, mean; number of categories expected from set cover, 10.

Efferocytosis assay

30 000 bone marrow derived dendritic cells were plated in white clear bottom 96 well plate (Corning #3610) per well. Untreated or dying cancer cells were collected 24h after cell death induction. Cells were stained with 20 μg/mL pHRodo (ThermoFischer #P35373) for 1h and washed with FBS. Cells were added to BMDCs in a 1:1 ratio. Plates were kept at 37°C under 5% CO_2 or at 4°C as a negative control. Fluorescence at excitation 490nm and emission 520nm were measured at different time points; 8, 20, 24, 30, 40 and 48 h after co-incubation on a microplate reader (BioTek). For the efferocytosis index calculations, fluorescent intensity values at 37°C were subtracted by the appropriate 4°C negative control.

5-Bromo-2′-deoxyuridine assay (BrdU-assay)

Isolated glioblastoma TAMs were plated with graded cell numbers from 20.000 to 100 cells in a dilutional series in 200 μL/well in a 96-flat-bottom plate and incubated overnight at 37°C and 5% CO_2. The following day, $1x10^5$ cells/well allogeneic CD14-depleted PBMC were added in 100 μL resulting in a final volume of 200 μL per well. Additionally, anti-PD-L1 (500 ng/mL) was added to some of the cultures to analyze its effect on macrophage-stimulated T cellT-cell proliferation. X-Vivo 15 media as well as PBMC ($1x10^5$ cells) or macrophages ($2x10^5$ cells) alone were used as negative controls. After five days of culture, cells were "pulsed" with 20 μL BrdU/well (BD Bioscience #550891) previously diluted 1:100 in X-Vivo-15 medium and incubated for 16 to 24 h at 37°C and 5% CO_2 to allow the base analogue BrdU to be incorporated in place of thymidine during the cell division of the proliferating cells. After incubation, cells were washed and fixed with 200 μL/well FixDenat for 30 min, followed by an incubation with 100 μL/well of a 1:100 diluted anti-BrdU antibody for 90 min, during which the peroxidase-conjugated antibody binds to the BrdU incorporated into the newly synthesized DNA. After discarding the antibody, cells were washed three times with 200 μL/well washing buffer diluted 1:10 in distilled water to remove non-specifically bound antibody. Cells were then incubated for a maximum of 30 min with 100 μL/well of a substrate solution (tetramethylbenzidine - TMB), which is converted to a blue dye by the peroxidase bound to the BrdU-*anti*-BrdU complex. The optical density was analyzed using an ELISA reader (660 nm versus 490 nm).

Cell isolation

Murine bone marrow-derived dendritic cells and macrophages

Bone marrow was isolated from wild type C57BL/6j, Ifnar$^{-/-}$ or Ccr7$^{-/-}$ mice. Both the femur and tibia were flushed using PBS and the cell suspension was centrifuged for 5 min at 1500rpm. The pellet was resuspended in red blood cell lysis buffer (Merck life science), incubated for 5 min and centrifuged. Cells were resuspended in RPMI supplemented with 100 u/mL penicillin, 100 μg/L streptomycin, and 10% heat-inactivated fetal bovine serum (FBS). Bone marrow derived cells were differentiated into macrophages by adding 25 ng/mL M-CSF (Peprotech #315-02) into the media for 6 days. For differentiation into DCs, 20 ng/mL GM-CSF (Peprotech #315-03) and 10 ng/mL IL4 (Peprotech #214-14) was added to the media for 7 days, with the exception of the macrophage-like vaccine which was stimulated with 20 ng/mL GM-CSF (Peprotech #315-02) and 10 ng/mL IL4 (Peprotech #214-14). Media was replenished after 3 days. Differentiation of dendritic cells and macrophages was confirmed by flow cytometry with respectively following fluorochrome-conjugated antibody clones were used; CD11b (clone M1/70), CD11c (clone N418) and CD11b (clone M1/70), F4/80 (clone BM8).

Murine splenocytes and T cells

Splenocytes were obtained from the spleen from wild type C57BL/6j mice. Spleens were minced and filtered through a 70-micron cell strainer. Cells were incubated in red blood cell lysis buffer for 5 min and centrifugated. For T cell isolation, splenocytes were purified using the negative selection pan-T cell isolation kit II (Miltenyi #130-095-130). Cells were maintained in RPMI supplemented with 100 u/mL penicillin, 100 μg/L streptomycin,10% heat-inactivated fetal bovine serum (FBS) and 100 IU/mL IL-2 (Peprotech #210-12). Following fluorochrome-conjugated antibody clones were used to confirm isolation of T cells by flow cytometry; CD3 (clone 17A2), CD4 (clone GK1.5) and CD8a (clone 53–6.7).

Murine lymph node isolation

3 days after DCvax-IT vaccination, mice were sacrificed, and the axillary and inguinal lymph nodes of both sides were isolated. To create a single cell suspension, lymph nodes were minced and filtered through a 70-micron cell strainer and analyzed by flow cytometry immediately. Following fluorochrome-conjugated antibody clones were used to analyze the isolated lymph nodes by flow cytometry; CD11c (clone N418), XCR1 (clone ZET), CD172A (clone P84), MHCII (clone M5/114.15.2), PDL1 (clone 10F.9G2), PD1 (clone RMP1-30), CD86 (clone GL1), F4/80 (clone T45-2342), CSF1R (clone AFS98), CD11b (clone ICRF44) and CD206 (clone C068C2).

Murine tumor infiltrating leukocytes (TILs) and tumor-associated macrophages (TAMs)

Tumors were isolated on day 23 after tumor injection. A single cell suspension was made, using the tumor dissociation kit (Miltenyi #130-096-730). TILs were isolated through magnetic bead separation via CD45 (Miltenyi #130-110-618). The CD45 negative population was collected for further flow cytometry analysis. For TAM isolation, anti-F4/80 microbeads (Miltenyi #130-110-443) were used.

Isolated TILs and TAMs were either maintained in RPMI supplemented with 100 u/mL penicillin, 100 μg/L streptomycin, 10% heat-inactivated fetal bovine serum (FBS) or stained for flow cytometry immediately. Following fluorochrome-conjugated antibody clones were used; FOXP3 (clone MF-14), GATA3 (clone TWAJ), CD62L (clone MEL-14), TCF1/7 (clone S33-966), CD107a (clone 1D4B), TOX (clone REA473), Tbet (clone O4-46), CD3 (clone 17A2), CD8a (clone 53–6.7), Ki-67 (clone 11F6), CD45 (clone 30-F11), Eomes (clone Dan11mag), CD127 (clone SB/199), PD1 (clone RMP1-30), CD4 (clone GK1.5), TIM3 (clone 5D12/TIM-3), IL2 (clone JES6-5H4), TNFα (clone MP6-XT22), IFNγ (clone XMG1.2), PDL1 (clone 10F.9G2 or 10F.2H11), PD1 (clone 29F.1A12), Siglec H (clone 551), CD11c (clone N418), XCR1 (clone ZET), CD172A (clone P84), MHCII (clone M5/114.15.2), PDL1 (clone 10F.9G2), PD1 (clone RMP1-30), CD86 (clone GL1), F4/80 (clone T45-2342), CSF1R (clone AFS98), CD11b (clone ICRF44), CD206 (clone C068C2), TNF (clone MP6-XT22), TRAIL (clone N2B2), FASL (clone KAY-10), CD31 (clone 390) and CD90.2 (clone 30-H12).

Human TIL isolation

For TIL isolation, surgically resected tumor samples of GBM patients at first diagnosis (primary GBM) or at recurrence after dendritic cell vaccination were collected and stored in MACS tissue storage solution (Miltenyi #130-100-008) for a maximum of 24 h at 4°C. TILs were isolated from tumor samples by the tumor dissociation kit (Miltenyi #130-095-929) and magnetic bead isolation using $CD45^+$ beads (Miltenyi #130-045-801). For flow cytometric analysis, the $CD45^+$ cells were stained for T cell and TAM characterizing markers: CD3 (clone OKT3 or UCHT1), CD4 (clone okt/04 or REA636)), CD8 (clone RPA-T8 or Sk1 or BW135/80), CD45RO (clone UCHL1), CD45 (clone REA747), CD163 (clone REA812), CD45PcP (clone 2D1), CD14 (clone 63D3), CSF1R (clone AFS98), CD274 (clone M1H1), isotype control (clone X40 or MOPC-21 or 27–35 or P3.6.2.8.1) for 15 min at 4°C, washed with phosphate-buffered saline (PBS), fixed with 4% d1) paraformaldehyde (PFA) and analyzed on a Cytoflex flow cytometer, using CytExpert 2.3 software (Beckman-Coulter).

For detection of interferon-γ, TILs were stimulated in X-Vivo 15 media (Lonza #BE02-060F) with 5 ng/mL phorbol myristate acetate (PMA) (Sigma-Aldrich #P8139) and 500 ng/mL Ionomycin (Sigma-Aldrich #I9657) for 5 h in the presence of 5 μg/mL Brefeldin A (BioLegend#420601) at 37°C and 5% CO_2 in a humidified atmosphere. After stimulation, cells were washed with PBS, stained for CD3, CD4, CD8 and CD45RO for 15 min at 4°C, washed with PBS and fixed for 15 min with 4% PFA. Subsequently, cells were permeabilized with 0.05% saponin in PBS (Sigma-Aldrich), stained intracellularly with: IFNγ (clone 4S.B3), CD3 (clone OKT3 or UCHT1), CD4 (clone okt/04 or REA636)), CD8 (clone RPA-T8 or Sk1 or BW135/80) and isotype control (clone X40 or MOPC-21 or 27–35 or P3.6.2.8.1) for 15 min and subjected to flow cytometric analysis.

Human $CD14^+$ $CD163^+$ macrophages

To separate macrophages from tumor-infiltrating leukocytes, cells were adjusted to a cell titer of 2.5x 10^7cells/mL in 0.5% HSA/D-PBS and stained with monoclonal antibodies directed against CD14 (clone 63D3) and CD163 (clone REA812). First, myeloid cells were identified by their typical FSC vs. SSC. Doublets are excluded via an SSC (W) vs. SSC (H) gating. Finally, within this single cell population, cells were gated based on their CD14 and CD163 expression, thereby targeting the double-positive population using an unstained control. This population was then sorted with a MoFlo XDP Sorter (Beckmann Coulter) into a 5 mL round bottom tube containing 1mL 100% FCS.

Immunohistochemistry

Human glioblastoma tissues from patients enrolled in the GlioVax Trial were obtained from the Department of Neuropathology, University Hospital Duesseldorf, and prepared as follows: Human tumor samples of primary as well as vaccinated patients after tumor recurrence were taken during surgery and fixed with buffered formaldehyde solution for up to 24 h. All tissues were subsequently washed and embedded in paraffin for archival storage. Samples from paraffin blocks were cut into 4-μm-thick sections (HM315 Microtom; Microm International GmbH, Walldorf, Germany), mounted on polylysine-coated microscope slides (Menzel, Bielefeld, Germany), air-dried thoroughly and stored until use. Paraffin was removed from sections by immersing two times for 10 min in 98.5% isomeric xylene (Carl Roth, Karlsruhe, Germany). To rehydrate the tissue, slides were immersed in decreasing concentrations of graded ethanol (2 × 5 min 100%, 5 min 96% and 5 min 70%), washed in deionized water and transferred to phosphate-buffered saline (PBS; Sigma Aldrich, Darmstadt, Germany). Antigen retrieval was achieved by cooking the slides 3 × 5min in Tris/ethylenediamine tetraacetic acid (EDTA) retrieval buffer at pH 9 (Sigma Aldrich). Slides cooled down to room temperature and transferred into PBS. For permeabilization, slides were incubated with a 0.3% Triton X-100 solution (Sigma Aldrich) for 10 min at room temperature. Unspecific Binding of was blocked by using FcR-Block (Miltenyi Biotec, Bergisch Gladbach, Germany) and 5% BSA-Solution (Sigma Aldrich).

Immunofluorescence Staining was performed with rabbit-*anti*-human CD8 – AF647 (clone EP1150y; 1:100; abcam, Cambridge, UK) and a primary mouse-*anti*-human CD163 (clone OTI2G12; 1:200; abcam) over night at 4°C. Secondary goat-*anti*-mouse Alexa Fluor 488 staining (#ab150113; 1:500; abcam) was performed for 2h at RT. Nuclear staining was performed with Hoechst 33342 (1 μg/mL – Life Technologies, Carlsbad, California, US). Quenching of autofluorescence was achieved by treatment with Background BackDrop Suppressor Red, Green, and Blue (molecular probes, Life Technologies) for 5 min at RT. Slides were mounted with the water-soluble mounting medium Fluoromount G (Life Technologies). A Zeiss inverted microscope was used for documentation (LSM800; Zeiss, Oberkochen, Germany). Several areas of vital tumor tissue infiltrated with immune cell subsets were selected for the scoring. Five to ten high power fields (HPF; 200× magnification) were assessed per sample quantifying the presence of the infiltration with $CD8^+$ T cells or $CD163^+$ macrophages.

In vivo experiments

Mouse experiments

Seven to twelve-week-old female/male C57BL/6J mice were subcutaneously (s.c) injected with $1x10^6$ TC1 LLC or MC38 cells. For prophylactic vaccinations, $1x10^6$ DCs were injected s.c twice (one week apart), before TC1-tumor inoculation. Mice were rechallenged with $1x10^6$ TC1 cells after 30 days. For curative vaccinations, $1x10^6$ DCs were injected s.c on day 9 and 16 after TC1 inoculation. When applicable, mice were cotreated with 250 μg of anti-PDL1 (clone MIH5; Polpharma Biologics) or D265A mutated anti-PDL1(Invivogen; described in Baudino et al. 2008[104]), anti-CTLA4 (clone 4F10; Polpharma Biologics), anti-CSF1R (AFS98; BioXCell), or anti-PD1(RMP1-14; Polpharma Biologics), on day 10 and 17 via intraperitoneal (i.p.) injections. For CD8 depletion experiments, mice were given 200 μg of anti-CD8 (clone YTS169; Polpharma Biologics), i.p. one day before tumor inoculation and then every other day until the tumor reached 500 mm^3. When applicable, cisplatin (8 mg/kg) (Sigma #p4394) was given on day 9 and 16. As indicated, 200μL clodronate liposomes (Liposoma) was given one day before tumor injected and every 2/3 days subsequently. Anti-NK1.1 and anti-IFNγ treatment regimens were derived from Hua et al. 2022.[67] 500μg of anti-NK1.1 was administrated three consecutive days before the start of treatment followed by weekly injections. 250 μg of anti-IFNγ was given twice a week starting one day before treatment. Mice were monitored and weighed every other day and tumor volume was determined by height x width x length.

CM-DIL

DC vaccines were stained with $1μL/10^6$ DCs of CellTracker CM-DiI dye (Thermofischer #C7000) prior to DC vaccination. 72 h after vaccination mice were euthanized and both the left and right axillary and inguinal lymph nodes were isolated. Single cell suspension was stained with the following fluorochrome-conjugated antibody clones: CD11b (clone M1/70), CD11c (clone N418), F4/80 (clone QA17A29), XCR1 (clone ZET), CD172A (P84), pSTAT1(pY701) and Siglec-H (551).

In silico analyses

Transcriptomic analysis with The Cancer Genome Atlas (TCGA) datasets

Immuno-transcriptomic analyses. We used the bulk transcriptomes of TCGA as pre-processed by the Toil-recompute project[105] in Xena[106] Immune cell proportions were inferred using the Quantiseq approach for immune cell deconvolution.[107] Filtering by Overlapping the Thorsson immune subtype class labels[17] from TCGA pan-cancer analyses (C1 to C6; see results for more details), resulted in 9126 samples in total. Overall *Z* score normalized enrichment analyses was performed for each respective immune cell-fractions or as ratios per immune subtype class, specified in the figure legends and the text. Survival endpoints were obtained from the same Xena Toil-Recompute TCGA data hub. A radar plot representation visualizing the Spearman's correlations between *CD274* gene expression levels in M1 or M2 macrophage fractions, was built using all patients from same TCGA data for which C1-C6 immune subtype class labels were available.

Extracellular network analyses. The extracellular network analyses was performed following the CRI iAtlas portal tools and methodology.[18] Herein, this network analyses uses a database of well-established ligand-receptor, cell-receptor, and cell-ligand pairs previously published elsewhere[19] and retrieved via FANTOM5[19]). Therefore, the network is built based on three criteria i.e., selected TCGA immune subtype class labels, Abundance threshold (%) and Concordance or Discordance threshold. Since the aim of the analyses was to reveal features of T cell-hostile tumors, it was hence restricted to only C4/C5 TCGA class-labels. Hence, abundance threshold creates a selection threshold for the nodes in the network wherein the abundance threshold is the frequency of samples in the upper 2 tertiles of cell-abundance or gene expression-distributions. Here we used the default abundance threshold of 66%. Finally, concordance threshold values are relevant for the inclusion of the edges in the network between any two relevant nodes. Concordance threshold is computed based on a contingency table consisting of the ternary values of the two applicable nodes for an edge. However, we pre-programmed this threshold to capture discordance probability i.e., an edge with a concordance score of 0.5 that is considered discordant because the analyses with threshold of 0.5 captures information on one node being highly expressed while the other being lowly expressed (thus, discordant, or uncorrelated) rather than both being simultaneously highly or lowly expressed.

GISTIC analysis. For genes derived from above extracellular network analyses (TNF, EDN3, IL13, EDN1, CX3CL1, VEGFB, IFNA2, IFNB1, IFNG, HMGB1, IL1A, IL1B), we performed high resolution copy number variation (CNV) analyses using the TCGA's genomic data via the GISTIC toolset poral[21] (https://portals.broadinstitute.org/tcga/home). we used the Gene-Centric GISTIC Analyses wherein, amplifications and deletion tendencies were separately analyzed per gene across a standardized pan-cancer TCGA dataset (i.e., 2013-08-16 TCGA Pan-Cancer data set), consisting of data from 4934 primary tumor samples passing GISTIC's default's quality control criteria from following cancer-types: bladder cancer (136), breast cancer (880), colorectal adenocarcinomas (585), glioblastoma multiforme (580), head and neck squamous cell cancer (310), kidney clear cell carcinoma (497), acute myeloid leukemia (200), lung adenocarcinoma (357), lung squamous cell carcinoma (344), ovarian serous carcinoma (563), and uterine endometrial carcinoma (496).

Prognostic impact analysis. For prognostic analyses i.e., impact of co-association between *CD274* and macrophage immune-fractions (TIMER-derived) on overall survival in multiple TCGA cancer-datasets spanning 19 cancer-types and 8493 patients, we utilized the TIMER2.0 portal.[108,109] the "Outcome module" was used for estimating the prognostic impact along with corrections for multiple covariates (stage, age, gender) in a multivariable Cox proportional hazard model. The hazard ratio from the Cox model was then computed into z-scores herein *Z* score >0 meant negative prognostic impact (shorter survival) while *Z* score <0 meant positive prognostic impact (prolonged survival). For this analyses, the following TCGA cancer datasets were utilized (number of patients in

brackets): BLCA (n = 408), BRCA (n = 1100), COAD (n = 458), GBM (n = 153), HNSC-HPV- (n = 422), HNSC-HPV+ (n = 98), KICH (n = 66), KIRC (n = 533), KIRP (n = 290), LGG (n = 516), LIHC (n = 371), LUAD (n = 515), LUSC (n = 501), OV (n = 303), PAAD (n = 179), PCPG (n = 181), PRAD (n = 498), READ (n = 166), SARC (n = 260), SKCM (n = 471), STAD (n = 415), THCA (n = 509), UVM (n = 80).

Immuno-oncology clinical trials analyses. Gene expression data for 12 clinical trials spanning 1142 patients in 5 cancer-types,[110–121] was downloaded from the Synapse server associated with the CRI iAtlas portal (syn24200710).[18] We applied the immune subtype classifier (C1-C6) from the original paper (https://github.com/CRI-iAtlas/ImmuneSubtypeClassifier) on the normalized gene expression data to infer the immune subtypes. Cancer immune subtypes C2/3/6 and C4/5 were merged as separate categories and differences in patient survival (OS) were investigated using lifelines 0.27.0 in Python 3.9.5. Statistical significance was investigated using the log rank test.

Transcriptomics analyses for murine subcutaneous tumors' bulk-RNAseq data. Affymetrix Mouse Exon 1.0 ST Array data, profiled from subcutaneous tumors based on B16-F10, TC1, CT26, MC38, LL2/LLC, RENCA, 4T1, TRAMPC1, EL4, P815 or PAN02 murine cancer cell lines implanted in syngeneic mice backgrounds, was derived from an existing published study (i.e., GSE85509)[27] and analyzed for expression levels of following metagene-signatures: pro-lymphocytic IFNγ/effector signaling, macrophages, type I IFN/ISG-response, or DCs,[27,28] and represented as a row-normalized heatmap.

In another case, for differential gene-expression (DGE) analyses, above transcriptomics data for TC1-tumours and MC38-tumours were analyzed in R 4.2.0, using the package oligo 1.60.0.[122] All corresponding CEL files were imported and RMA-corrected, then summarized to the gene level for which identifiers were mapped based on the NetAffx CSV files provided by Affymetrix (MoEx-1_0-st-v1.na28.mm9.transcript.csv). For the pairwise comparison between TC1 and MC38, we used limma 3.52.2[123] and applied t-tests with empirical Bayesian shrinkage of variance. pP-values were adjusted in accordance with the Benjamini-Hochberg method.

Finally, for Correlation gene-set enrichment analyses (GSEA) analyses, following assorted genes specifically enriched in the TC1-tumours (compared to MC38-tumours) from above DGE analyses, that we further annotated as myeloid/macrophage-signaling relevant based on literature were utilized: *Dkk2, Figf, Akr1c18, Ptgs1, Ereg, Thbs1, Thbs2, Ptgs2, Aspa, Pla2g7, Pdpn, Pla2g4a, Areg, Cd80, Nox4, Abca1, Cd33, Il1rl1, P2ry5, Axl, Mrc1, Gas2, Ctsl.* Correlation GSEA analyses of this gene-set (gene-set 1) versus well-established translationally-relevant markers of tumor-associated macrophages (*Cx3cr1, Ccr2, Tek, Csf1r, Cd274, Pdcd1, Sirpa, Ido1, Pdcd1lg2, Cd40*[124,125]) (gene-set 2) was performed against the background of a reference murine macrophage transcriptomic-profile, using the standardized work-flow of Immuno-Navigator portal.[55]

Maturation trajectory analyses for single-DC vaccine's transcriptomes. Trajectory analyses of monocytic-derived DC vaccines micro-array transcriptomes was performed using the Gene Expression Omnibus (https://www.ncbi.nlm.nih.gov/geo/) dataset (GSE85698).[23] This study included 93 DC vaccines that were administered to 18 prostate carcinoma (PDAC) patients. Each patient received multiple lots of autologous DC. Vaccination regimen included 5 vaccinations (one every 3 weeks) with boost vaccinations in case of response. At least 2 vaccines per patient are included. Normalized microarray expression dataset was extracted from GEO portal and further processed to filter mitochondrial genes and non-protein coding genes. Microarray's duplicated annotation probes was collapsed by per-gene average ratio of probe's expression values. Initial dimensionality reduction to further calculate trajectory inference was performed using high variable genes with additional threshold parameters of loess fraction 0.1 and number of genes $\leq$ 4000. Hence UMAP dimensionality reduction was based on the top 9 principal components which covered 99.9% of genetic variance and was computed on a 2-dimensional scale of 4 neighbors. Trajectory inference was performed using STREAM (Huidong Chen et al., Nature Comm, 2019) on the precomputed dimensionality reduction using *"seed elastic principal graph"* algorithm with default parameters except for *4 neighbors* and *"ap" clustering* algorithm. Further branch pruning was performed using *"elastic principal graph"* with default parameters except for epg_alpha 0.01, epg_mu 0.2, epg_lambda 0.03, epg_n_nodes 5 and incr_n_nodes 3. Signature expression of several signatures was calculated on per DC vaccine sample of average expression genetic profiles. Leaf markers were calculated using ''detect leaf markers'' function against root S0 group using default parameters except for cutoff_zscore 1.0, cutoff_pvalue 1.0, min_num_cells 5 and percentile_expr 99. Pathway analysis for each leaf marker genes was computed using gseapy with signal to noise methodology of gene set permutation type for a maximum of 2000 permutations, including Reactome pathways between 1 and 2000 genes. Top ranked and biologically relevant Reactome pathways were plotted based on this Normalized Enrichment Score (NES) and FDR values.

Analysis of TC1-tumor's single-cell RNA-sequencing (scRNAseq) datasets. Single-cell gene expression for untreated TC-1 tumors (GSM7103827) was downloaded from the gene expression omnibus.[53] Objects were pre-processed with Scanpy 1.9.3. Cells with less than 200 counts were removed, genes expressed in less than 10 cells were also discarded. Counts were normalized to 10000 cells per cell and log transformed. Highly variable genes with at least 0.0125 expression, max mean 3 and minimal dispersion of 0.5, resulting in 2281 cells and 4015 highly variable genes. Cells that could not be reliably annotated were removed, reducing the cell count from 2281 to 1838. Cells were annotated using the BioTuring cell type prediction approach (HaiTam v3, Talk2data https://talk2data.bioturing.com/predict). UMAPs were calculated using UMAP-learn 0.5.3 through Scanpy. Differential gene expression was obtained with Scanpy's rank_genes_groups function. Corresponding fold changes and associated p values were plotted as lollipop plots using Matplotlib 3.7.1. Raw expression data was loaded through Seurat 4.3.0.1 and SeuratDisk 0.0.0.9020 in R 4.3.1 and queried for inferred interactions with CellChat 1.6.1. Macrophages were assigned to the PD-L1 positive class using expression of *Cd274* > 0.

Analysis of cancer patient's single-cell RNA-sequencing (scRNAseq) datasets. For analyses of *CD274* or *Cd274* expression at single-cell resolution on pan-tumor level, various scRNAseq pan-tumor maps from existing peer-reviewed literature were accessed from the Tumor Immune Single Cell Hub,[126] a large-scale curated database integrating single-cell transcriptomic data from >2 million single-cells (with a uniform/standardized workflow accounting for quality control and batch-effects) across >75 high-quality tumor-derived datasets. We used the Gene Exploration module of TISCH to short-list scRNASeq datasets with stable expression profiling available for at least most of the following tumor-associated cells: $CD4^+$T cells, $CD8^+$T exhausted cells, NK cells, $CD8^+$T cells in general, fibroblasts, endothelial cells, B cells, malignant/cancer cells, DCs and macrophages. This delineated 21 eligible single-cell (sc)RNAseq datasets spanning 13 diverse cancer-types (SARC, CRC, SKCM, HNSC, UVM, Glioma/GBM, CHOL, OV, LIHC, NSCLC, BRCA, PAAD, BCC), 287 patients and 2 species (humans or mice), further accessible here: GSE119352, GSE122969, GSE120575, GSE103322, GSE120909, GSE139829, GSE123139, GSE139324, GSE141982, GSE125449, GSE118828, GSE131907, GSE139555, GSE136206, GSE111672, GSE131928, GSE146771, GSE115978, GSE99254, GSE110686, GSE123813. Across these datasets, we derived average gene expression of *CD274* or *Cd274* across an entire cell-type cluster per scRNAseq dataset and integrated all the values to create row-normalized heatmaps.

Predictive analyses of $PDL1^+$TAMs signature in immuno-oncology clinical trials. Pre-treatment tumor-derived gene expression data for 454 cancer patients (185 responders vs. 269 non-responders) treated with anti-PDL1 ICB (atezolizumab or durvalumab) spanning 5 cancer-types (4 patients with ureter/renal pelvis cancer, 345 with urothelial cancer, 31 with bladder cancer, 72 with esophageal cancer and 2 with renal cell carcinoma), or 761 cancer patients (504 responders vs. 257 non-responders) treated with anti-PD1 ICB (nivolumab or pembrolizumab) spanning 11 cancer-types (39 patients with lung cancer, 14 with glioblastoma, 7 with ureter/renal pelvis cancer, 45 with gastric cancer, 5 with colorectal cancer, 415 with melanoma, 59 with bladder cancer, 22 with hepatocellular carcinoma, 14 with breast cancer, 31 with renal cell carcinoma, and 110 with head & neck cancer) were accessed from the ROC Plotter server.[127,128] We interrogated the impact of a $PDL1^+$TAM metagene (composed of *CD68, CD163, CD14, CD274*) on tumor-level objective response rate (ORR)-based responders vs. non-responders for either anti-PDL1 or anti-PD1 ICB treatments. Analyses was restricted to pre-treatment transcriptome while excluding any statistical outliers. Statistical significance was investigated using the Mann-Whitney U test.

QUANTIFICATION AND STATISTICAL ANALYSIS

The statistical details of all the analyses are reported either in the figure legends, figures and/or methods sections, including statistical analysis performed, statistical significance thresholds/values and in most cases the counts/number of data-points. All the statistical tests used herein were always two-tailed unless otherwise explicitly mentioned. Gene signatures were estimated by considering the average expression of all the genes within that signature, unless otherwise mentioned. Details about used software for analysis can be found in the key resources table.